博士論文

論文題目　Static and dynamic spin transport in lateral spin valves（面内スピンバルブにおける静的及び動的スピン輸送）

氏　　名　井土　宏（Hiroshi Idzuchi）

博士論文

Static and dynamic spin transport in lateral spin valves

(面内スピンバルブにおける静的及び動的スピン輸送)

THESIS

Hiroshi Idzuchi

井土 宏

THE UNIVERSITY OF TOKYO

MARCH, 2014

東京大学
THE UNIVERSITY OF TOKYO

RIKEN
Since 1917

物性研究所
The Institute for Solid State Physics

RIKEN
Center for Emergent Matter Science

東京大学大学院
新領域創成科学研究科
GRADUATE SCHOOL OF FRONTIER SCIENCES
THE UNIVERSITY OF TOKYO

Advisory Committee:

Prof. dr. Y. Otani, Chair/Advisor

Prof. dr. A. Fert

Prof. dr. S. Maekawa

Prof. dr. Y. Sasaki

Prof. dr. S. Nakatsuji

Abstract

Static and dynamic spin transport in lateral spin valves

Hiroshi Idzuchi, Doctor of Philosophy

The University of Tokyo, 2014

Supervisor: Prof. Y. Otani

Generation, control and detection of spin current are key ingredients in spintronics. Pure spin current, a flow of spin angular momentum without net charge flow, bridges the conventional charge based transport phenomena and the physics in magnetism such as a spin-transfer torque, *s-d* interaction etc. and thus is the key concept in spintronics. The thesis is devoted to a series of experiment aiming at the understanding of static and dynamic properties of the spin current by means of a non-local spin injection technique in lateral spin valves (LSVs).

The non-local spin injection technique in lateral spin valves is an effective method to generate the pure spin current in non-magnetic (NM) material. The non-local spin injection was first demonstrated in 1985 using micro-scale devices which consist of a 50-μm-thick Al bar with ferromagnetic junctions [M. Johnson and R. H. Silsbee, Phys. Rev. Lett. 55, 1790 (1985)]. This experiment yielded a tiny spin accumulation signal of a few tens of pico-volts. The experiment was revisited in 2001 using nano-scaled LSVs [F. Jedema, A. T. Filip, and B. J. van Wees, Nature **410**, 345 (2001)]. This brought about an

enhanced signal of about one micro-volt at room temperature, which spurred intensive research efforts in non-local LSVs for spintronic device applications. Further enhancement of the spin accumulation is beneficial for the understandings of transport properties of the pure spin current which is flowing along the slope of the spin accumulation.

In this thesis, the non-local spin injection properties were studied with metallic LSVs. The enhancement of the spin accumulation was realized in LSVs with ferromagnet/MgO/Ag junctions. With annealed $Ni_{80}Fe_{20}$ (Permalloy, Py)/MgO/Ag junctions, the hundred-fold spin accumulation signal $\Delta V = 225$ μV was realized. The results were analyzed using spin diffusion model and the underlying physics was understood as a (spin) resistance (conductance) mismatch. In addition to it, the structure of LSV was systematically optimized. The dual injection scheme was demonstrated and the effect of spin absorption was examined. Dual injector lateral spin valves (DLSVs) with Py/MgO/Ag junctions enabled 3-fold enhancement whereas a little (~1.2 times) enhancement in Py/Ag junctions due to spin absorption. LSVs with $Co_{50}Fe_{50}$/MgO/Ag junctions showed the 20% improvement of injection/detection efficiency compared with Py/MgO/Ag junctions.

Spin relaxation mechanism in NM wire was experimentally examined by characterizing spin transport properties of Ag and Mg in LSVs. For Ag, the temperature variations of the spin relaxation time τ_{sf} and the momentum relaxation time τ_e were analyzed to discuss the intrinsic spin relaxation properties in non-magnet (NM). Spin-flip probability $\varepsilon \equiv \tau_e / \tau_{sf}$, the characteristic value of the Elliott-Yafet spin relaxation mechanism, of Ag nanowire was agreed with the value of bulk Ag obtained by conduction electron spin resonance. Phonon contribution of the spin relaxation was universally expressed with the material independent curve scaled by the spin-orbit interaction for monovalent metal. The surface spin scattering, which hampered quantitative analysis in previous reports, is well suppressed in Ag nanowire by an MgO capping layer. Non-local

spin injection into Mg nanowire revealed that the spin diffusion length was comparable to the other NM such as Cu, Ag and Al despite the fact that the light metal Mg shows small spin-orbit interaction. This is because the complex electronic structure of Mg promotes spin relaxation (spin-hot-spot), which explains the relatively short spin diffusion length of approximately 200 nm at room temperature.

Collective spin precession in LSVs, so-called Hanle effect, were studied. In ballistic spin transport, spins can coherently rotate at a Larmor frequency proportional to the applied perpendicular magnetic field. This allows us to control the direction of the spins in the channel and to manipulate the output signal of LSVs by adjusting an effective external parameter such as the Rashba field tunable via a gate voltage. This scheme realizes an active spin device such as the spin-transistor [S. Datta and B. Das, Appl. Phys. Lett. **56**, 665 (1990)]. In contrast, in a diffusive pure spin current in NMs, the precession causes dephasing, and drastically decreases the spin accumulation. Therefore the understandings of dynamic transport properties of spin current is indispensable.

The dynamic transport properties of the pure spin current in metallic LSVs with various devices were systematically studied. The effect of the spin absorption on the Hanle signal was clearly observed. We have successfully formulated the Hanle effect for the LSVs with anisotropic spin absorption for the transverse and longitudinal components of the spin polarization in the spin current relative to the detector magnetization-direction, which enables to characterize intrinsic spin transport properties even with the spin absorption effect. The velocity of diffusive spin currents and the transit-time distribution was successfully characterized by applying Fourier transform to the experimental Hanle signals, resulting in excellent agreement with the empirical model in the case of Py/MgO/Ag junctions. In contrast, we found that the transit-time distribution in LSVs with Py/Ag junctions strongly deviated from that expected in the empirical model and that the

spins diffuse much faster than in LSVs with Py/MgO/Ag junctions, reflecting the spatial distribution of chemical potential affected by the type of junctions.

Moreover, we demonstrate the LSVs with dual injectors enable to detect a highly coherent spin precession over a distance of 10 μm with keeping spin accumulation vector in plane. We show the phase coherency in precession is improved with an increase of the channel length. The coherency in the spin precession shows a universal behavior as a function of the normalized separation between the injector and the detector in material-independent fashion for metals and semiconductors including graphene.

The thesis presents a systematic study on the spin dependent transport in the metallic devices. The thesis consists of three complimentary studies, the efficient non-local spin injection (the effect of the junction and the device structure), the spin relaxation mechanism (intrinsic properties: phonon contribution and the effect of the electronic structure), and the collective spin precession (the characterization of the spin transport properties and the modulation), which are deeply related each other. The in-depth understandings of lateral spin transport could be base on the future physics of spintronics and new technological applications based on pure spin current.

CONTENTS

Chapter 1

Introduction

1.1 Spintronics

Spintronics has explored spin-related phenomena such as giant magneto-resistance, tunneling magneto-resistance and spin transfer torque, which are caused by an interaction between spins of itinerant *s(p)* electrons and localized *d* electrons [1]. Recently, spin current is becoming increasingly important not only in traditional magnetic metals but also in the wide variety of materials [2, 3]. Spin Hall effect, which gives direct response of the spin dependent scatterings, was electrically detected by injecting spin currents into metals, semiconductors and even oxides [4-7]. Moreover, spin current was utilized to manipulate the static and dynamic properties of magnetization in nanostructures and microstructure via spin-transfer-torque [8-14].

1.2 Motivation

Pure spin current, a flow of spins without charge current, is different from the conventional spin-polarized current as schematically shown in Fig. 1.1 [3]. The pure spin current bridges the conventional charge based transport phenomena and the physics in magnetism such as a spin-transfer torque, *s-d* interaction etc. and thus is the key concept in spintronics. One of excellent techniques to generate the pure spin current is non-local spin injection, as shown in Fig. 1.2(b). When the spin-polarized current in ferromagnet (FM) is injected into non-magnet (NM), spins are accumulated in the vicinity of the FM/NM interface. The accumulated spins diffuse in the NM, and thus the spin accumulation is formed in the place where no charge current is present.

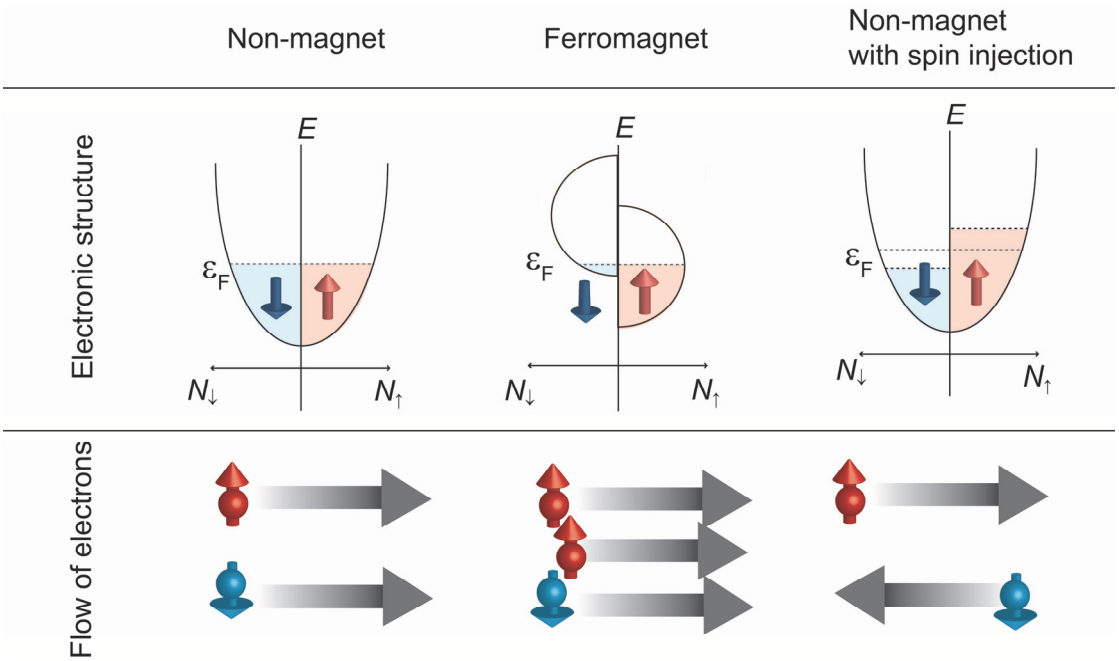

Figure 1.1: Schematics of three types of flow of electrons. **Charge current:** In the conventional NM, the electrons with up or down spin flow in one direction. The net flow of spin angular momentum is zero. **Spin-polarized current:** In the FM, since the density of states at the Fermi surface for the spins is different, the current density is different. As a result, both flows of charge and spin are observed. **Pure spin current:** when spins are injected into the NM, the non-equilibrium spin state, spin accumulation is induced. Pure spin current is flowing along the slope of the spin accumulation and defined as the currents in opposite direction with the same density for up and down spin. The net flow of spin angular momentum is nonzero. The term "**spin current**" is used as the same meaning of the pure spin current. The term "spin polarized current" has same meaning with the sum of the (pure) spin current and the charge current.

Non-local spin injection was first demonstrated in 1985 using micro-scale devices which consist of a 50-μm-thick Al bar with ferromagnetic junctions [15]. This experiment yielded a tiny spin accumulation signal of a few tens of pico-volts. The experiment was revisited in 2001 using nano-scaled lateral spin valves (LSVs) [16]. This brought about an enhanced signal of about one micro-volt at room temperature, which spurred intensive research efforts in non-local LSVs for spintronic device applications.

In order to boost spintronic research and device applications, the solid understanding of transport properties of spin current is required. In particular, the efficient

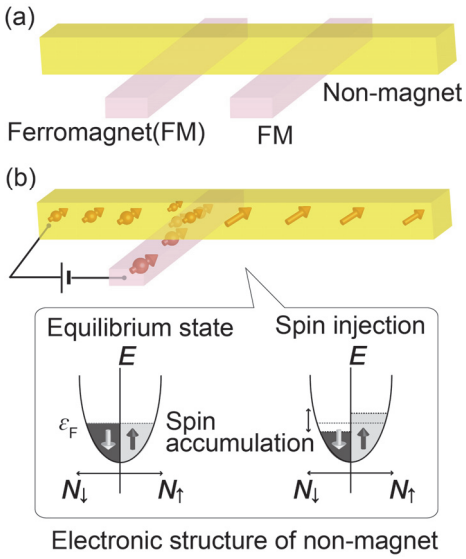

Figure 1.2: (a) Lateral spin valve structure (b) schematic of non-local spin injection technique Spin accumulation is induced by injecting spin-polarized current from FM into NM ($N\uparrow$, $N\downarrow$: spin-dependent density of states, E : energy. ε: Fermi energy). Spin accumulation and spin current, a flow along the slope of the spin accumulation, are diffusive and thus they appear even in the place where the charge current is not applied.

generation of the spin current is indispensable not only for the device application but also to characterize the static and dynamic transport properties of spin current. Previous report suggested that the spin injection was not efficiently performed in the sense that the spin polarization of the injected current in non-magnetic (NM) material is much smaller than the one in injector FM, the so-called spin-resistance mismatch issue [17-19]. The efficient spin injection was so far theoretically studied [18, 19] and the junction properties are expected to be important. In this study the spin injection is performed in various junctions and the (spin) resistance mismatch issues is detailed using the spin diffusion equation.

Transport properties of pure spin current are strongly dependent on NM materials [20]. So far, the spin relaxation mechanism in NM was studied by means of conduction electron spin resonance etc.[20] and the sample dimensions were limited to bulk. Spin relaxation in NM nanowire, of which understanding is required by the emergent

development in the spintronic devices, can be studied with LSV by characterizing transport properties of spin current. Since the spin-orbit interaction plays an important role, we studied the spin transport and relaxation mechanisms of Mg as a light metal as well as Ag as a "standard" NM metal. Since the LSV consists of nano-scaled hybrid FM/NM structure, the performance (quality) of the device strongly depends on the fabrication process and experimental conditions. The intrinsic and extrinsic properties of the spin transport and relaxation in the NM nanowire are separated by analyzing the temperature dependent spin relaxation process, which results in the characteristic values of the spin-flip probability in consistent with other techniques such as CESR.

In the last part, the thesis is devoted to the collective precession of the pure spin current in lateral spin valves, so-called Hanle effect [15, 21]. In ballistic spin transport, spins can coherently rotate at a Larmor frequency proportional to the applied perpendicular magnetic field. This allows us to control the direction of the spins in the channel and to manipulate the output signal of LSVs by adjusting an effective external parameter such as the Rashba field tunable via a gate voltage. This scheme realizes an active spin device such as the spin-transistor [22]. In contrast, in a diffusive pure spin current in NMs, the precession causes dephasing, and decreases drastically the spin accumulation. Therefore the understandings of dynamic transport properties of spin current is indispensable.

In the thesis, we demonstrate the LSVs with dual injectors enable to detect a highly coherent spin precession over a long-distance. The phase coherency in precession is detailed and the material-independent properties of diffusive spin current is extracted. Moreover, the spin absorption effect, detailed as the spin-resistance mismatch in the first part (chapter 4) is found to affect dynamic transport properties of spin current. We have successfully formulated the Hanle effect for the LSVs with anisotropic spin absorption for the transverse and longitudinal components of the spin polarization in the spin current

relative to the detector magnetization-direction, which enables to characterize intrinsic spin transport properties even with the spin absorption effect.

1.3 Outline

The thesis consist of six chapters. Chapter 1 describes the general introduction and the motivation of the thesis. Chapter 2 summarizes the theory of spin transport from the fundamental aspect to the practical formula. Chapter 3 briefly explains the principle and the procedure of the fabrication as well as the measurement techniques.

Chapter 4 describes the enhancement of the spin accumulation with MgO inserted FM/NM junctions. Hundred-fold spin accumulation was realized. Spin injection characteristic was performed and analyzed using the spin diffusion model and is discussed with (spin) resistance mismatch issue. The extended structure of LSV was also studied and shown to enable to enhance the spin accumulation by a factor of four with a proper magnetic configuration.

Chapter 5 focuses on the mechanism of spin relaxation. Temperature variation of the spin transport properties of Ag or Mg-based LSV was detailed. The phonon contribution was determined and found to be well described by the Elliott-Yafet mechanism. Scaled plot (Monod-Benue plot) was revisited. The spin relaxation in Mg was found to be affected not only by spin-orbit interaction and but also by the electronic structure.

Chapter 6 describes Hanle effect in LSV. Long 10 μm collective spin precession was realized for Ag nanowires. The detailed study revealed that characteristics of collective spin precession can be summarized in material independent fashion in the scaled plot with normalized spin transport length. The impact of spin absorption effect was examined. The

dynamic spin transport properties was described in considering anisotropic spin absorption mechanism for longitudinal and transvers spins.

References for chapter 1

[1] S. A. Wolf, D. D. Awschalom, R. A. Buhrman, J. M. Daughton, S. von Molnár, M. L. Roukes, A. Y. Chtchelkanova, and D. M. Treger, *Science* **294**, 1488 (2001).
[2] I. Žutić, J. Fabian, and S. D. Sarma, *Reviews of modern physics* **76**, 323 (2004).
[3] C. Chappert, A. Fert, and F. N. Van Dau, *Nature materials* **6**, 813 (2007).
[4] S. O. Valenzuela and M. Tinkham, *Nature* **442**, 176 (2006).
[5] X. Lou, C. Adelmann, S. A. Crooker, E. S. Garlid, J. Zhang, K. S. M. Reddy, S. D. Flexner, C. J. Palmstrøm, and P. A. Crowell, *Nature Physics* **3**, 197 (2007).
[6] M. Morota, Y. Niimi, K. Ohnishi, D. H. Wei, T. Tanaka, H. Kontani, T. Kimura, and Y. Otani, *Physical Review B* **83**, 174405 (2011).
[7] K. Fujiwara, Y. Fukuma, J. Matsuno, H. Idzuchi, Y. Niimi, Y. Otani, and H. Takagi, *Nature Communications* **4**, 2893 (2013).
[8] T. Kimura, Y. Otani, and J. Hamrle, *Physical Review Letters* **96**, 037201 (2006).
[9] T. Yang, T. Kimura, and Y. Otani, *Nature Physics* **4**, 851 (2008).
[10] J. Z. Sun *et al.*, *Applied Physics Letters* **95**, 083506 (2009).
[11] D. Ilgaz *et al.*, *Physical Review Letters* **105**, 076601 (2010).
[12] L. Liu, C. F. Pai, Y. Li, H. W. Tseng, D. C. Ralph, and R. A. Buhrman, *Science* **336**, 555 (2012).
[13] Y. Kajiwara *et al.*, *Nature* **464**, 262 (2010).
[14] L. Liu, T. Moriyama, D. C. Ralph, and R. A. Buhrman, *Physical Review Letters* **106** (2011).
[15] M. Johnson and R. H. Silsbee, *Physical Review Letters* **55**, 1790 (1985).
[16] F. Jedema, M. Nijboer, A. T. Filip, and B. J. van Wees, *Physical Review B* **67**, 085319 (2003).
[17] A. T. Filip, B. H. Hoving, F. J. Jedema, B. J. van Wees, B. Dutta, and S. Borghs, *Physical Review B* **62**, 9996 (2000).
[18] E. I. Rashba, *Physical Review B* **62**, R16267 (2000).
[19] A. Fert and H. Jaffrès, *Physical Review B* **64**, 184420 (2001).
[20] J. Bass and W. P. Pratt, *Journal of Physics: Condensed Matter* **19**, 183201 (2007).
[21] F. Jedema, H. Heersche, A. T. Filip, J. Baselmans, and B. J. van Wees, *Nature* **416**, 713 (2002).
[22] S. Datta and B. Das, *Applied Physics Letters* **56**, 665 (1990).

Chapter 2

Theory of spin transport

2.1 Spin diffusion model

2.1.1 Two current model and spin-polarized current

In order to describe the transport phenomena in ferromagnet(FM), Mott proposed two current model [1]. It assumes two conduction channels in which electrons with spin in parallel (↑) and antiparallel (↓) to the magnetization. In FM, the density of state of majority spin on Fermi surface is larger than that of minority spin. Therefore, electrical conductivities for each spin, $\sigma\uparrow$, $\sigma\downarrow$, hold the relation $\sigma\uparrow > \sigma\downarrow$. Hence the current density of each channel is different and the total current is called as spin-polarized current (Fig. 1.1). The equivalent circuit with a current application to FM is shown in Fig. 2.1 and thus

$$\begin{aligned} I_{\uparrow} &= V / R_{\uparrow}^{\mathrm{F}} \propto \sigma_{\uparrow} \\ I_{\downarrow} &= V / R_{\downarrow}^{\mathrm{F}} \propto \sigma_{\downarrow}, \end{aligned} \tag{2.1}$$

where the spin polarization of FM P_{F} is defined as $P_{\mathrm{F}} \equiv (\sigma\uparrow - \sigma\downarrow)/(\sigma\uparrow + \sigma\downarrow)$ and $I\uparrow$ ($I\downarrow$) are the current with spin ↑ (↓). The current in each channel is

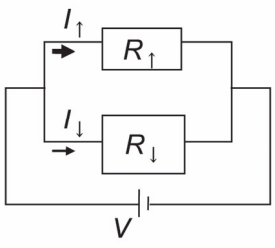

Figure 2.1: Two current model.

$$I_{\uparrow} = \frac{1+P_{\mathrm{F}}}{2} I,$$
$$I_{\downarrow} = \frac{1-P_{\mathrm{F}}}{2} I. \tag{2.2}$$

2.1.2 Current and electro chemical potential

The current density j_σ in the channel σ is written with the drift term and the diffusion term which is characterized by non-equilibrium electron density δn_σ

$$\mathbf{j}_\sigma = \sigma_\sigma \mathbf{E} - eD_\sigma \nabla \delta n_\sigma, \tag{2.3}$$

where σ_σ , D_σ and **E** are the conductivity, the diffusion constant of each spin channel σ, and the electric field, respectively. According to Einstein relation $\sigma_\sigma = e^2 N_\sigma D_\sigma$ and $\delta n_\sigma = N_\sigma \delta\varepsilon_\sigma$ one obtains

$$\begin{aligned} \mathbf{j}_\sigma &= -\frac{\sigma_\sigma}{e}\left[e\nabla\phi + \frac{\nabla \delta n_\sigma}{N_\sigma(\varepsilon_{\mathrm{F}})}\right] \\ &= -\frac{\sigma_\sigma}{e}\left[e\nabla\phi + \nabla\delta\varepsilon_\sigma\right] \end{aligned} \tag{2.4}$$

where ϕ_e and $\delta\varepsilon_\sigma$ are the electrical potential and the shift in the chemical potential of carriers from its equilibrium value. Therefore, current density is expressed by the electro chemical potential $\mu_\sigma = \mathrm{e}\phi_e + \varepsilon_\sigma$

$$\mathbf{j}_\sigma = -\frac{\sigma_\sigma}{e}\nabla\mu_\sigma. \tag{2.5}$$

2.1.3 Spin diffusion equation

The continuity equations for charge and spin in the steady states are

$$\nabla \cdot (\mathbf{j}_\uparrow + \mathbf{j}_\downarrow) = 0$$
$$\nabla \cdot (\mathbf{j}_\uparrow - \mathbf{j}_\downarrow) = -e\frac{\delta n_\uparrow}{\tau_{\uparrow\downarrow}} + e\frac{\delta n_\downarrow}{\tau_{\downarrow\uparrow}}. \quad (2.6)$$

Note that $j_s \equiv j\uparrow - j\downarrow$ is spin current density. By combining it with eqns.(2.3)-(2.5) and the detail balanced formula $N\uparrow/\tau\uparrow\downarrow = N\downarrow/\tau\downarrow\uparrow$ where $\tau_{\sigma\sigma'}$ is the scattering time of an electron from spin state σ to σ', one obtains [2-6]

$$\nabla^2(\sigma_\uparrow\mu_\uparrow + \sigma_\downarrow\mu_\downarrow) = 0$$
$$\nabla^2(\mu_\uparrow - \mu_\downarrow) = \lambda_{sf}^{-2}(\mu_\uparrow - \mu_\downarrow), \quad (2.7)$$

with

$$\lambda_{sf} = \sqrt{D\tau_{sf}}, \quad (2.8)$$

where λ_{sf} and D are the spin diffusion length and the diffusion constant. To derive eqn.(2.7), $\tau_{sf}^{-1} = (\tau_{\uparrow\downarrow}^{-1} + \tau_{\downarrow\uparrow}^{-1})/2$, $D^{-1} = (N_\uparrow D_\downarrow^{-1} + N_\downarrow D_\uparrow^{-1})(N_\uparrow + N_\downarrow)$ is used.

2.1.4 Spin accumulation and spin absorption

As described in chapter 1, the current application between FM and non-magnet (NM) induces the different electro chemical potentials near the interface depending on the spin channel. This difference of spin-dependent electro chemical potential is called as spin accumulation $\delta\mu = (\mu\uparrow - \mu\downarrow)$. According to eqn.(2.7), $\delta\mu$ obeys

$$\nabla^2\delta\mu = \lambda_{sf}^{-2}\delta\mu. \quad (2.9)$$

$\delta\mu$ decreases with distance, and its characteristic length is called as spin diffusion length. The typical spin diffusion lengths are about several nanometers to several micrometers for non-magnetic(NM) materials and several nanometers to tens of nanometers for

ferromagnetic(FM) materials [7]. From eqn.(2.5), the relation between spin accumulation and spin current is [8]

$$j_s = -\frac{\sigma_N}{2e}\nabla\delta\mu. \tag{2.10}$$

Note $\sigma\uparrow = \sigma\downarrow$ in NM.

It is convenient to use the spin-resistance $R_{N(F)} \equiv \rho\lambda_{sf}/A$ where A is the cross-sectional area of the spin current [4, 9] and ρ is the resistivity, to characterize the diffusion properties of spin accumulation (In this thesis we use this notation instead of the spin-resistance $R_F = \rho\lambda_{sf}/A/(1\text{-}P_F^2)$ where P_F is the spin polarization for FM). The subscripts of N and F represent NM and FM, respectively. We consider the one dimensional spin diffusion model where spin current is injected at $x = 0$ and decays at infinity. In this case, the solution of eqn.(2.9) is $\delta\mu \propto \exp(-|x|/\lambda_{sf})$ and according to eqn.(2.10)

$$I_s \equiv j_s / A = \frac{\delta\mu / 2e}{R_N}. \tag{2.11}$$

For FM, eqn.(2.11) holds with the corrected factor of $(1\text{-}P_F^2)$, i.e., $I_S=\delta\mu/(2eR_F/(1\text{-}P_F^2))$. It means that the spin-resistance is the measure of how much current is flowing by a spin accumulation. Spin-resistance also characterize spin absorption, effect which will be described in the next section.

2.1.5 Generation of spin accumulation

In order to clarify the feature of the generation of the spin accumulation, eqn.(2.7) is solved in the geometry of the single FN/NM junction shown in Fig. 2.2(a). Here, no contact resistance and no spin-flip at the interface are assumed. Also, one dimensional model is used (assuming that the spin diffusion length of FM is much shorter than the

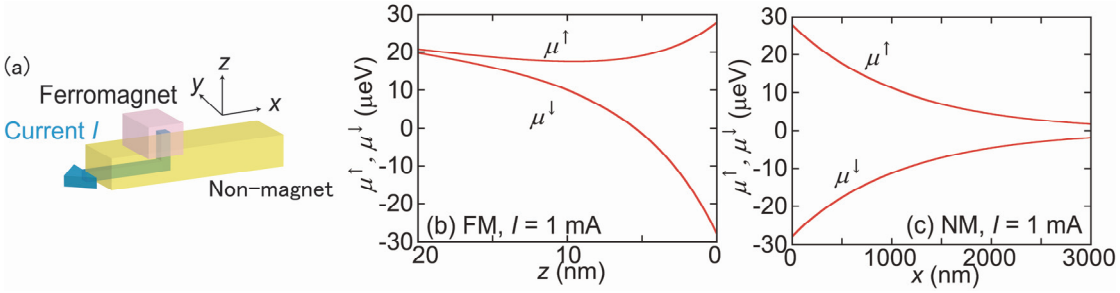

Figure 2.2: (a) Schematics of spin injection at FM/NM junction. (b) Spatial distribution of the electro chemical potential in FM (c) and in NM. The curve is derived with the material parameters shown in sec. 4.4.

widths of FM and NM and the spin diffusion length of NM is much shorter than the width and the thickness of NM). The electro chemical potentials are expressed as

$$
\begin{cases}
\mathrm{F1}\begin{cases}
\mu_{\mathrm{F1}}^{\uparrow}(z)/e = +\dfrac{\sigma_{\mathrm{F1}}}{\sigma_{\mathrm{F1}}^{\uparrow}} b_1 e^{-z/\lambda_{\mathrm{F1}}} + \dfrac{I}{\sigma_{\mathrm{F1}} A_{\mathrm{F}}} z + V_1, \\
\mu_{\mathrm{F1}}^{\downarrow}(z)/e = -\dfrac{\sigma_{\mathrm{F1}}}{\sigma_{\mathrm{F1}}^{\downarrow}} b_1 e^{-z/\lambda_{\mathrm{F1}}} + \dfrac{I}{\sigma_{\mathrm{F1}} A_{\mathrm{F}}} z + V_1,
\end{cases} \\
\mathrm{N}\begin{cases}
\mu_{\mathrm{N}}^{\uparrow}(x)/e = \dfrac{I}{\sigma_N A_{\mathrm{N}}}\Theta(-x) + \delta\mu_{\mathrm{N}}(x)/e, \\
\mu_{\mathrm{N}}^{\downarrow}(x)/e = \dfrac{I}{\sigma_N A_{\mathrm{N}}}\Theta(-x) - \delta\mu_{\mathrm{N}}(x)/e, \\
\text{where } \delta\mu_{\mathrm{N}}(x)/e = a_1 \mathrm{e}^{-|x|/\lambda_{\mathrm{N}}},
\end{cases}
\end{cases}
\tag{2.12}
$$

where $\Theta(x)$ is the step function, indices F and N are ferromagnet and non-magnet, respectively, a_1,b_1,V_1 is the constant determined by the boundary condition. a_1 and b_1 correspond the generated spin accumulation in NM and FM, respectively and V_1 is the potential difference between the FM and the NM. Spin current is $I_s \equiv Aj_s$ and according to eqn.(2.5)

$$
\begin{aligned}
&\mathrm{F}: \mathbf{I_S} = -P_{\mathrm{eff}} I \mathbf{e}_z, \\
&\mathrm{N}: \begin{cases} \mathbf{I_S} = -\dfrac{a_1}{R_\mathrm{N}} e^{-x/\lambda_\mathrm{N}} \mathbf{e}_x \quad (x<0), \\ \mathbf{I_S} = +\dfrac{a_1}{R_\mathrm{N}} e^{-x/\lambda_\mathrm{N}} \mathbf{e}_x \quad (x>0), \end{cases} \\
&\text{where} \quad P_{\mathrm{eff}} = P_\mathrm{F} - \frac{2b_1}{IR_\mathrm{F}} e^{-z/\lambda_\mathrm{N}},
\end{aligned}
\tag{2.13}
$$

where $\mathbf{e}_x$ and $\mathbf{e}_z$ is the unit vector in x and z direction. From eqn.(2.13), one finds that the effective spin polarization P_{eff} decreases from "bare" FM spin polarization P_F due to the back-flow $2(b_1/IR_\mathrm{F})\exp(-z/\lambda_\mathrm{F})$.

In order to obtain the electro chemical potentials for NM and FM, the coefficients a_1, b_1 and V_1 are derived with eqn.(2.12) with using the conditions of the continuity of the electro chemical potential and its first order differential (that is, there is no interface resistance and the loss of spin) as

$$
\begin{aligned}
a_1 &= IR_\mathrm{N} \frac{\dfrac{P_\mathrm{F}}{1-P_\mathrm{F}^2}\dfrac{R_\mathrm{F}}{R_\mathrm{N}}}{1+\dfrac{2}{1-P_\mathrm{F}^2}\dfrac{R_\mathrm{F}}{R_\mathrm{N}}}, \\
b_1 &= IR_\mathrm{F}\left(-\frac{\dfrac{P_\mathrm{F}}{1-P_\mathrm{F}^2}\dfrac{R_\mathrm{F}}{R_\mathrm{N}}}{1+\dfrac{2}{1-P_\mathrm{F}^2}\dfrac{R_\mathrm{F}}{R_\mathrm{N}}} + \frac{P_\mathrm{F}}{2} \right), \\
V_1 &= -\frac{2P_\mathrm{F}}{1-P_\mathrm{F}^2}\frac{R_\mathrm{F}}{R_\mathrm{N}} a_1 + \frac{P_\mathrm{F}^2}{1-P_\mathrm{F}^2} IR_\mathrm{F}.
\end{aligned}
\tag{2.14}
$$

Figures 2.2(b) and (c) show the spatial distribution of the electro chemical potential.

Another important consequence of the consideration of junction is *spin absorption* effect. Suppose the NM wire sustaining the spin accumulation. Subsequent spin relaxation takes place in an additional material in Ohmic contact with the NM [9]. This is so-called

spin absorption (or spin sink effect). The spin accumulation and spin current is flowed in to the material with small spin-resistance. The spin-resistance is also the measure of how much spin current is absorbed into the attached material. Spin absorption into FM material provides an attractive means to manipulate the magnetization in magnetic nanostructures [10-13].

2.1.6 Detection of spin accumulation

Spin accumulation in NM is detected by spin-dependent electro-chemical potential. In the case of Ohmic junction, the electro chemical potential of FM and NM is continuous, and thus the spin accumulation appears in FM attached to the NM sustaining spin accumulation. Spin relaxation takes place in FM in the length-scale of the spin diffusion length as shown in Fig. 2.3(a). The relaxation depends on the relative direction of the spin polarization of injected spin and the magnetization of detection FM electrode because the density of states near the Fermi surface depends on the spin. Therefore the potential after the relaxation depends on the spin as shown in Fig. 2.3(a). When the magnetization of injector FM and detector FM is antiparallel, the detection voltage is different. Spin

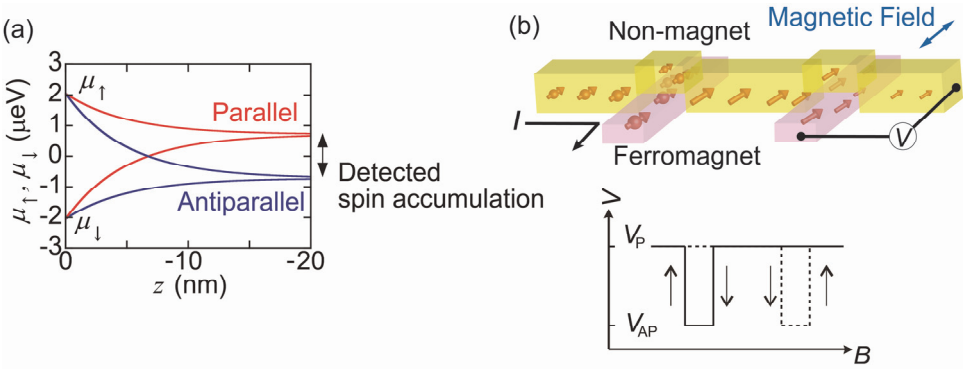

Figure 2.3: (a) Spatial distribution of electro chemical potential in FM detector (I = 1 mA). (c) Configuration of non-local spin valve measurement and spin valve signal. Magnetic field is applied in parallel to the FM wires. Two distinct output voltages V_P and V_{AP} are observed for parallel and antiparallel magnetization states between injector and detector FMs when the switching field of FM wires are different.

polarization of FM in most materials are less than 100 %, the detection voltage is smaller than the spin accumulation in NM. Another case of resistive junction for the detection of spin accumulation is described in sec. 2.1.8.

2.1.7 Lateral spin valve

The generation and detection of spin accumulation is possible by using lateral spin valve (LSV) which consists of at least two FM wires bridged by NM wires. The two FM wires have different switching fields. Therefore, by sweeping the external magnetic field, the magnetization states changes from parallel → Antiparallel → Parallel → Antiparallel → Parallel, and two distinct output voltages are observed as shown in Fig. 2.3(c). Detection voltage V is proportional to the injected current I [2], and V/I is called as non-local resistance. Especially, the difference of the voltages $\Delta V \equiv (V_{\mathrm{P}}\text{-}V_{\mathrm{AP}})$ and its normalized value $\Delta R_{\mathrm{S}} \equiv \Delta V/I$ are called as spin accumulation signal (voltage) and spin signal, respectively and used as performance index of the LSV.

2.1.8 Formula for Spin signal (Takahashi-Maekawa formula)

Spin signal ΔR_{S} can be obtained by using spin diffusion equation. In similar to sec. 2.1.5, spatial distribution of the electro chemical potential is derived by eqn.(2.7). By taking account of the contact resistance, the boundary conditions are

$$eI^{\sigma} = G_{\mathrm{I}j}^{\sigma}(\mu_{\mathrm{F}}^{\sigma} - \mu_{\mathrm{N}}^{\sigma})\,|_{\mathrm{Boundary}}, \tag{2.15}$$

where $G_{\mathrm{I}j}{}^{\sigma}$ is the conductivity of the j-th interface (junction) for spin channel σ. One obtains spin signal as [2]

$$\Delta R_{\mathrm{S}} = \frac{V^{\mathrm{P}} - V^{\mathrm{AP}}}{I}$$
$$= \frac{4R_{\mathrm{N}}\left[\frac{P_{\mathrm{I1}}^2}{1-P_{\mathrm{I1}}^2}\left(\frac{R_{\mathrm{I1}}}{R_{\mathrm{N}}}\right)+\frac{P_{\mathrm{F1}}}{1-P_{\mathrm{F1}}^2}\left(\frac{R_{\mathrm{F1}}}{R_{\mathrm{N}}}\right)\right]\left[\frac{P_{\mathrm{I2}}^2}{1-P_{\mathrm{I2}}^2}\left(\frac{R_{\mathrm{I2}}}{R_{\mathrm{N}}}\right)+\frac{P_{\mathrm{F2}}^2}{1-P_{\mathrm{F2}}^2}\left(\frac{R_{\mathrm{F2}}}{R_{\mathrm{N}}}\right)\right] e^{-L/\lambda_{\mathrm{N}}}}{\left[1+\frac{2}{1-P_{\mathrm{I1}}^2}\left(\frac{R_{\mathrm{I1}}}{R_{\mathrm{N}}}\right)+\frac{2}{1-P_{\mathrm{F1}}^2}\left(\frac{R_{\mathrm{F1}}}{R_{\mathrm{N}}}\right)\right]\left[1+\frac{2}{1-P_{\mathrm{I2}}^2}\left(\frac{R_{\mathrm{I2}}}{R_{\mathrm{N}}}\right)+\frac{2}{1-P_{\mathrm{F2}}^2}\left(\frac{R_{\mathrm{F2}}}{R_{\mathrm{N}}}\right)\right]-e^{-2L/\lambda_{\mathrm{N}}}}$$

(2.16)

where $P_{\mathrm{F}j}$ is the spin polarization of the j-th FM, $R_{\mathrm{F}j}$ is the spin-resistance of j-th FM. $R_{\mathrm{I}j} = 1/G_{\mathrm{I}j}$ $(G_{\mathrm{I}j} = G_{\mathrm{I}j}^{\uparrow} + G_{\mathrm{I}j}^{\downarrow})$ is the interface resistance (conductance) of j-th junction, $P_{\mathrm{I}j} = (G_{\mathrm{I}j}^{\uparrow} - G_{\mathrm{I}j}^{\downarrow})/(G_{\mathrm{I}j}^{\uparrow} + G_{\mathrm{I}j}^{\downarrow})$ is the interfacial spin polarization and L is the separation between the injector and the detector. This formula includes the effect of "spin-resistance mismatch" (will be detailed in the section 2.1.9). When $R_{\mathrm{I}} >> R_{\mathrm{F}}$ and R_{N},

$$\Delta R_{\mathrm{S}} = R_{\mathrm{N}} P_{\mathrm{I1}} P_{\mathrm{I2}} e^{-L/\lambda_{\mathrm{N}}}. \tag{2.16b}$$

The principle of the detection of spin accumulation for resistive junction (including magnetic tunneling junction) is as follows. The spin current is absorbed into the junction according to eqn.(2.15).[1] $G_{\mathrm{I}j}{}^{\sigma}$ is different but $|I^{\sigma}|$ is same for the spin channels. Therefore the decrease of the electro chemical potentials at the junction, $|(\mu_{\mathrm{F}}^{\sigma} - \mu_{\mathrm{N}}^{\sigma})|_{\mathrm{Boundary}}|$ are different for the channels and the spin accumulation is detected via resistive junctions with a finite junction spin-polarization.

[1] For the resistive junction, the absorbed spin current is usually much smaller than one for Ohmic junction.

2.1.9 Spin-resistance mismatch, the effect of the interface on the generation and the detection of spin accumulation

In this section, we discuss the effect of the junction on the generation and the detection of the spin accumulation. As discussed in sec. 2.1.4, spin injection accompanies back-flow of spin current, which effectively reduces spin injection efficiency I_S/I from the ideal value of P_F. The back-flow is induced because the spin-resistance of FM material (e.g. Py, Co) is much smaller than that of NM material (e.g. Ag, Cu) [7], in which condition the spin absorption from NM to FM takes place. From the spin diffusion equation, one obtains spin current near the injector

$$j_S = j \frac{\dfrac{2P_F}{1-P_F^2}\dfrac{R_F}{R_N}}{1+\dfrac{2}{1-P_F^2}\dfrac{R_F}{R_N}}. \tag{2.17}$$

Figure 2.4(a) shows the spin injection efficiency I_S/I at the injector (x = 0, z = 0) as a function of the ratio of spin-resistance for FM to that for NM. The spin diffusion length of FM is one-three orders of magnitude smaller [7]. In the typical case of $R_F/R_N \sim 0.1$, it is clear that only a little part of spin is injected into NM.

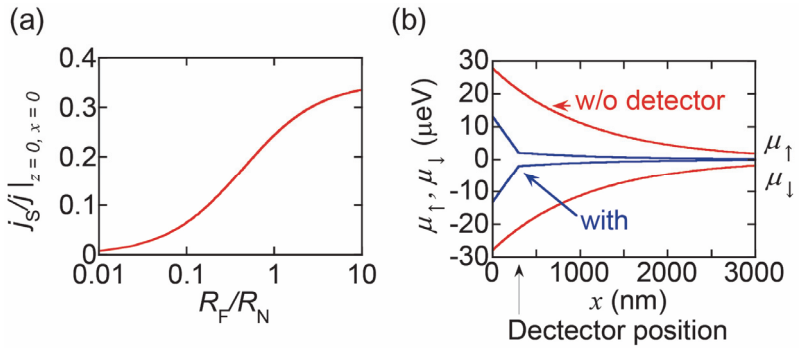

Figure 2.4: (a) Spin injection efficiency as a function of the ratio of spin-resistances for FM and NM. (b) The effect of spin absorption on the spatial distribution of the spin accumulation in NM. R_F/R_N=0.1 and I = 1 mA.

Moreover, the spin-resistance mismatch affects the detection property of spin accumulation as shown in Fig. 2.4(b): the spin accumulation of NM is decreased by the spin absorption effect at the detector.

Historically, the obstacle of the spin injection from FM into NM semiconductor is reported as the difference of conductivity mismatch $\sigma_N << \sigma_F$ [14]. As for the spin injection into NM metal, the conductivity matches $\sigma_N > \sigma_F$, and the detection itself was reported in 1985 [15] although the efficient spin injection was hampered. Therefore the issue should be called as probably "spin-resistance" mismatch. After the conductivity mismatch was reported [14], the use of the tunnel junction [16] and the spin-polarized layer with the appropriate junction resistance [17] were theoretically proposed. The injection efficiency will improve by the effect of the interface under the condition that the junction resistance is comparable or higher than the spin-resistance of NM, which is attributed to the change of the spatial distribution of the spin current. In the previous study for the effect of the junction in spin injection efficiency, people mainly focused on the spin injection into NM semiconductor. The enhancement of the spin injection/detection efficiency was expected even for the lateral spin valve consisting of NM metal and the efficient spin injection is reported by using high resistance tunnel burrier [18]. However, the injection efficiency at the finite bias (hot electron states) [19] was strongly reduced and the bias current was limited due to the joule heating. Therefore the spin accumulation in the previous studies was up to ~ 1 μV [19-21]. On the other hand, according to the theoretical considerations mentioned above, the required interface resistance is 2-3 orders of magnitude smaller than the conventional high resistance magnetic tunnel junctions. Hence the enhancement of the spin accumulation is expected in the appropriate FM/NM junctions.

2.1.10 Spin valve signal in lateral spin valve with dual injector

LSV has various extended structure such as multi-terminal terminal geometry [22], which, enables to enhance spin accumulation compared with the single injector lateral spin valve (SLSV) which consists of two FM wires bridged by a NM wire.

In order to enhance spin accumulation, there are three factors we need to consider. One is the spin relaxation volume. Since the spin accumulation is diffusive, the smaller relaxation volume is better to enhance spin accumulation. Second is the number of the injectors. The larger number of the injector increases the source of spin currents if we control the directions of the magnetizations and current to obtain the constructive effect. Last is the spin absorption effect which could decrease the spin accumulation just by adding the FM electrode, which competes the enhancement of spin accumulation by an increase of the source of spin current.

Dual injector LSV (DLSV) with spin-polarized interface layer enables to enhance spin accumulation. As shown in Fig. 2.5, a DLSV consists of three FM wires bridged by a NM wire. By cutting the edge of a NM wire at the injector, the unnecessary spin relaxation volume is removed. The measurement geometry is shown in Fig. 2.5. Spin absorption effect will examine as follows.

The procedure to obtain the expression for spin accumulation in DLSV is same with SLSV. The electro chemical potential of the N wire in DLSV is $\mu_{\mathrm{N}}^{\sigma}(x)=\bar{\mu}_{\mathrm{N}}+\sigma\delta\mu_{\mathrm{N}}$, where $\bar{\mu}_{\mathrm{N}}=\left(eI/\sigma_{\mathrm{N}}A_{\mathrm{N}}\right)x$ for $x<0$, $\bar{\mu}_{\mathrm{N}}=0$ for $x>0$, $\sigma=+(-)$ for up (down) spin,

Figure 2.5: Schematic of dual injector LSV.

$\delta\mu_{\rm N} = a_1 e^{-|x+d_{12}|/\lambda_{\rm N}} + a_2 e^{-|x|/\lambda_{\rm N}} + a_3 e^{-|x-L|/\lambda_{\rm N}}$, a_1, a_2 and a_3 are the coefficient determining the electro chemical potential shifts due to the spin injection/absorption from FM1, FM2 and FM3, respectively, d_{12} and L are the center-center separation between FM1-FM2 and FM2-FM3, respectively. The spin diffusion eqn.(2.7) with the boundary conditions for DLSV yields [23]

$$\begin{pmatrix} (r_{\rm I1}+r_{\rm F1}+2) & -(r_{\rm I1}+r_{\rm F1}-2)e^{-d_{12}/\lambda_{\rm N}} & -(r_{\rm I1}+r_{\rm F1}-2)e^{(-d_{12}-L)/\lambda_{\rm N}} \\ e^{-d_{12}/\lambda_{\rm N}} & (1+r_{12}+r_{\rm F2}) & e^{-L/\lambda_{\rm N}} \\ e^{(-L-d_{12})/\lambda_{\rm N}} & e^{-L/\lambda_{\rm N}} & (1+r_{\rm I3}+r_{\rm F3}) \end{pmatrix} \begin{pmatrix} a_1 \\ a_2 \\ a_3 \end{pmatrix} = \begin{pmatrix} -\cos\theta_{13}\left(P_{\rm I1}r_{\rm I1}+P_{\rm F1}r_{\rm F1}\right) \\ \frac{1}{2}\cos\theta_{23}\left(P_{\rm I2}r_{12}+P_{\rm F2}r_{\rm F2}\right) \\ 0 \end{pmatrix} eIR_{\rm N}, \tag{2.18}$$

$$eV_3 = -(P_{\rm I3}r_{\rm I3} + P_{\rm F3}r_{\rm F3})a_3, \tag{2.19}$$

where V_3 is the detection voltage at the detector FM3, $\cos\theta_{13} = \mathbf{e}^{\rm FM1}\bullet\mathbf{e}^{\rm FM3}$ and $\cos\theta_{23} = \mathbf{e}^{\rm FM2}\bullet\mathbf{e}^{\rm FM3}$ with the unit vector $\mathbf{e}^{{\rm FM}j}$ in the direction of the magnetization, $r_{{\rm F}j} = [2/(1-P_{{\rm F}j}{}^2)]R_{{\rm F}j}/R_{\rm N}$ and $r_{{\rm I}j} = [2/(1-P_{{\rm I}j}{}^2)]R_{{\rm I}j}/R_{\rm N}$ are the normalized spin-resistance of FM and the normalized interface resistance, respectively. The detected spin signal V_3/I is calculated as

$$\frac{V_3}{I} = \frac{R_{\rm N}}{2}\left(P_{\rm I3}r_{\rm I3}+P_{\rm F3}r_{\rm F3}\right)e^{-L/\lambda_{\rm N}} \times \frac{(2+r_{\rm I1}+r_{\rm F1})(P_{\rm I2}r_{\rm I2}+P_{\rm F2}r_{\rm F2})\cos\theta_{23} - 2e^{-d_{12}/\lambda_{\rm N}}\left(r_2+r_{\rm F2}\right)(P_{\rm I1}r_{\rm I1}+P_{\rm F1}r_{\rm F1})\cos\theta_{13} + e^{-2d_{12}/\lambda_{\rm N}}\left(-2+r_{\rm I1}+r_{\rm F1}\right)(P_{\rm I2}r_{\rm I2}+P_{\rm F2}r_{\rm F2})\cos\theta_{23}}{(2+r_{\rm I1}+r_{\rm F1})\left[(1+r_{\rm I2}+r_{\rm F2})(1+r_{\rm I3}+r_{\rm F3})-e^{-2L/\lambda_{\rm N}}\right]+e^{-2d_{12}/\lambda_{\rm N}}\left(-2+r_{\rm I1}+r_{\rm F1}\right)\left[e^{-2L/\lambda_{\rm N}}\left(-1+r_{\rm I2}+r_{\rm F2}\right)+\left(1+r_{\rm I3}+r_{\rm F3}\right)\right]}. \tag{2.20}$$

It turns out that the spin accumulation is maximized when the magnetization configuration of the injectors F_1-F_2 is antiparallel. The overall change of the spin valve signal ΔR_S in the in-plane magnetic field dependence of V_3/I is expressed as

$$\begin{aligned}\Delta R_S &= \left(V_3|_{\cos\theta_{13}=-1,\cos\theta_{23}=+1} - V_3|_{\cos\theta_{13}=+1,\cos\theta_{23}=-1}\right)/I \\ &= R_N(P_{F3}r_{F3}+P_{I3}r_{I3})e^{-L/\lambda_N}\times \\ &\frac{(2+r_{I1}+r_{F1})(P_{I2}r_{I2}+P_{F2}r_{F2})+2e^{-d_{12}/\lambda_N}(r_{I2}+r_{F2})(P_{I1}r_{I1}+P_{F1}r_{F1})+e^{-2d_{12}/\lambda_N}(-2+r_{I1}+r_{F1})(P_{I2}r_{I2}+P_{F2}r_{F2})}{(2+r_{I1}+r_{F1})\left[(1+r_{I2}+r_{F2})(1+r_{I3}+r_{F3})-e^{-2L/\lambda_N}\right]+e^{-2d_{12}/\lambda_N}(-2+r_{I1}+r_{F1})\left[e^{-2L/\lambda_N}(-1+r_{I2}+r_{F2})+(1+r_{I3}+r_{F3})\right]}.\end{aligned}$$

(2.21)

Assuming that all the electrodes and their interface are identical, eqn.(2.21) is expressed as

$$\begin{aligned}\Delta R_S &= R_N e^{-L/\lambda_N}(P_F r_F + P_I r_I)^2 \times \\ &\frac{(1+e^{-d_{12}/\lambda_N})\left[(2+r_I+r_F)+e^{-d_{12}/\lambda_N}(-2+r_I+r_F)\right]}{(2+r_I+r_F)\left[(1+r_I+r_F)^2-e^{-2L/\lambda_N}\right]+e^{-2d_{12}/\lambda_N}(-2+r_I+r_F)\left[(1+r_I+r_F)+e^{-2L/\lambda_N}(-1+r_I+r_F)\right]}.\end{aligned}$$

(2.22)

When $d_{12} >> \lambda_N$, eqn.(2.22) reduces to the previous expression of ΔR_S for the conventional SLSV (2.16),

$$\Delta R_S = R_N e^{-L/\lambda_N}\times\frac{(P_F r_F + P_I r_I)^2}{\left(1+r_I+r_F\right)^2-e^{-2L/\lambda_N}}. \qquad (2.23)$$

The enhancement factor of DLSV compared to SLSV is defined as

$$\begin{aligned}\alpha &\equiv \frac{(2.22)}{(2.23)} \\ &= \frac{\left[(1+r_I+r_F)^2-e^{-2L/\lambda_N}\right](1+e^{-d_{12}/\lambda_N})\left[(2+r_I+r_F)+e^{-d_{12}/\lambda_N}(-2+r_I+r_F)\right]}{(2+r_I+r_F)\left[(1+r_I+r_F)^2-e^{-2L/\lambda_N}\right]+e^{-2d_{12}/\lambda_N}(-2+r_I+r_F)\left[(1+r_I+r_F)+e^{-2L/\lambda_N}(-1+r_I+r_F)\right]}.\end{aligned}$$

(2.24)

α increases monotonically as $r_I + r_F$ increases and shows a maximum $\alpha_{max} \equiv 1+ \exp(-2d_{12}/\lambda_N) + 2\exp(-d_{12}/\lambda_N)$ for $r_I + r_F >> 1$.

When the interface resistance R_I is larger enough to prevent the spin absorption effect into FM from N ($R_I >> R_N$), ΔR_S is expressed as

$$\Delta R_S = \alpha_{max} P_I^2 R_N e^{-L/\lambda_N}. \tag{2.25}$$

The spin signal is enhanced by a factor of α_{max} compared to SLSV where the $1+ \exp(-2d_{12}/\lambda_N)$ and $2\exp(-d_{12}/\lambda_N)$ in α_{max} are from spin injections from FM2 and FM1, respectively. The first term of 1 represents the direct diffusive spin flow to FM3 from FM2, and the next term of $\exp(-2d_{12}/\lambda_N)$ represents the flow to FM3 from FM2 via the reflection at the edge of the N wire near FM1. The last term of $2\exp(-d_{12}/\lambda_N)$ is related to spins injected from FM1.

Fig. 2.6 shows simulated enhancement factor for various spin-resistance mismatch factor $r^* \equiv r_I+r_F$ as a function of normalized separation d_{12}/λ_N. The experimental verification of the enhancement of spin accumulation and the effect of spin absorption in DLSV is described in sec. 4.5 and refs. [23, 24].

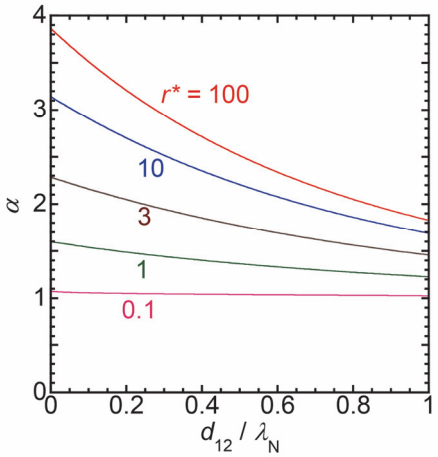

Figure 2.6: The enhancement factor of various spin-resistance mismatch factor $r^* \equiv r_I+r_F$ from with spin absorption regime (r^*=0.1) to without spin absorption regime (r^*=100) as a function of normalized separation d_{12}/λ_N.

2.2 Hanle effect

2.2.1 Introduction

When the magnetic field is applied perpendicular to the spin orientation, Larmor spin precession is induced. The collective spin precession of spin current, so-called Hanle effect is one of the most effective methods to characterize dynamic properties of the pure spin current (Fig. 2.7) [25, 26]. This section outlines Hanle effect in LSV and shows the explicit expression to deduce spin transport parameters.

2.2.2 Transit time distribution

Hanle effect is so far expressed by two styles. One is the use of transit-time distribution [26] (sec. 2.2.2) and another is the Bloch-Torrey equation (sec 2.2.3) [27]. The equivalence will be shown in sec. 2.2.3.

The collective spin precession can be characterized by the distribution of the transit-time $P(t)$ which determines the angle of precession when the Larmor frequency is given.

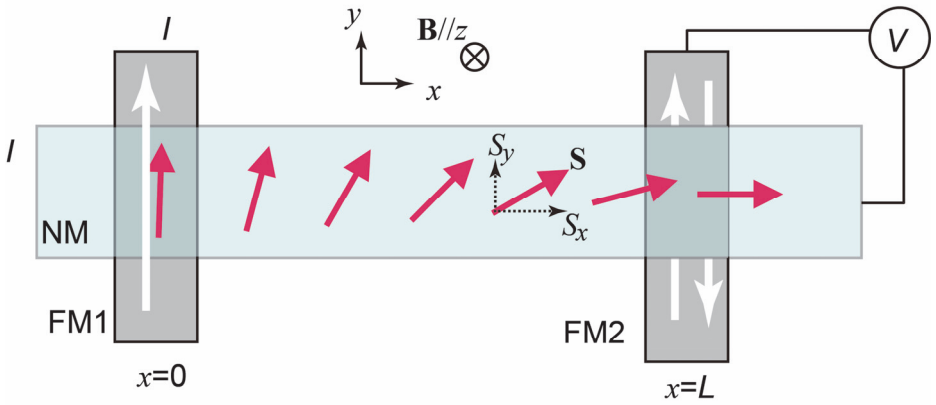

Figure 2.7: Precession of accumulated spins in NM in a lateral spin valve in the presence of perpendicular magnetic field **B** where the spin accumulation (spin density) ***S*** rotates during the travel of distance L between the injector FM1 and the detector FM2. The projection of S (S_y) along the magnetization of FM2 is detected by FM2 as output voltage V.

$P(t)$ is the probability of the spin reached at the detector position $x = L$ after the spin is injected at the time $t = 0$, and expressed as

$$P(t) = \frac{1}{\sqrt{4\pi D_N t}} \exp\left(-\frac{L^2}{4 D_N t} - \frac{t}{\tau_{sf}} \right). \tag{2.26}$$

where D_N and τ_{sf} are the diffusion constant of NM and the spin relaxation time, respectively. $P(t)$ in the typical parameters is shown in Fig. 2.8(a). With an increase of the time t, spin relaxation pronounces and hence the $P(t)$ drastically decreases.

The non-local resistance of a response of the spin precession, Hanle effect, is expressed as

$$V / I \propto \int_0^\infty dt P(t) \cos(\omega_L t), \tag{2.27}$$

where $\omega_L = \gamma_e B$ is the Larmor frequency, $\gamma_e = 2\mu_B / \hbar$ is the gyromagnetic ratio, μ_B is the Bohr magneton, and $\hbar$ is the Planck constant. Figure 2.8(b) shows the eqn.(2.26) for different ω_L and the typical signal of Hanle effect. The decoherence of spin precession characterizes the shape of Hanle signal.

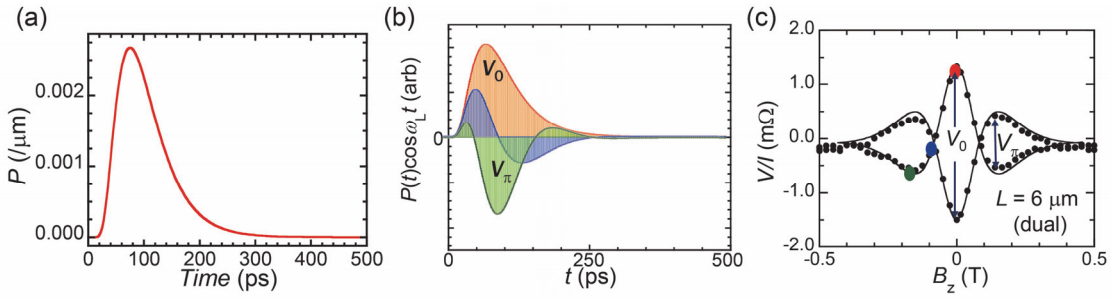

Figure 2.8: (a) The transit-time distribution of spin current for LSV with Py/MgO/Ag junctions. (b) The transit-time distribution of spin current for LSV with Py/MgO/Ag junctions. Red, blue and green lines show $P(t)\cos(\omega_L t)$ with the magnetic field in which $\int_0^\infty dt P(t)\cos(\omega_L t)$ shows maximum (B=0), zero (B=$B_{\pi/2}$) and minimum (B=B_π) and correspond to 0, π/2 and π rotation, respectively. (c) Hanle signal for LSV with dual injector Py/MgO/Ag junctions with L = 6 μm. Red, Blue and Green dots are proportional to the colored area in (b).

The proportionality factor of eqn.(2.26) is given as follows. Right hand of eqn.(2.26) is

$$\frac{\tau_{\mathrm{sf}}}{2\lambda_{\mathrm{sf}}}\mathrm{Re}\left[\frac{1}{\sqrt{1-i\omega_{\mathrm{L}}t}}\exp\left(-\sqrt{1-i\omega_{\mathrm{L}}t}\,\frac{|x|}{\lambda_{\mathrm{sf}}}\right)\right]\rightarrow\frac{\tau_{\mathrm{sf}}}{2\lambda_{\mathrm{sf}}}\exp\left(-\frac{|x|}{\lambda_{\mathrm{sf}}}\right)\qquad(\omega_{\mathrm{L}}\rightarrow 0),\quad(2.28)$$

where $\lambda=(D_{\mathrm{N}}\tau_{\mathrm{sf}})^{1/2}$ is used.[2] By comparing with eqn.(2.16b), one obtains [26]

$$V/I=\frac{1}{e^2N(\varepsilon_{\mathrm{F}})A_{\mathrm{N}}}P_{\mathrm{I}}^2\int_0^\infty dtP(t)\cos(\omega_{\mathrm{L}}t).\qquad(2.29)$$

This is thus equivalent to the complex representation of [28]

$$\frac{V}{I}=\frac{1}{2}P_{\mathrm{I1}}P_{\mathrm{I2}}R_{\mathrm{N}}\,\mathrm{Re}\left[\left(\lambda_\omega/\lambda_{\mathrm{N}}\right)\exp(-L/\lambda_\omega)\right].\qquad(2.30)$$

where $\lambda_\omega=\dfrac{\lambda_{\mathrm{N}}}{\sqrt{1+i\omega_{\mathrm{L}}\tau_{\mathrm{sf}}}}$. (2.31)

2.2.3 Bloch-Torrey equation

By using Bloch-Torrey equations, one can explicitly link the Hanle effect with the "equation of motion" for non-equilibrium magnetization $\mathbf{m}_{\mathrm{N}}$ [29, 30]. Bloch-Torrey equation is

$$\frac{\partial\mathbf{m}_{\mathrm{N}}}{\partial t}=-\gamma_e\left[\mathbf{m}_{\mathrm{N}}(\mathbf{r})\times\mathbf{B}\right]-\frac{\mathbf{m}_{\mathrm{N}}}{\tau_{\mathrm{sf}}}+D_{\mathrm{N}}\nabla^2\mathbf{m}_{\mathrm{N}}(\mathbf{r}),\qquad(2.32)$$

where each term of eqn.(2.32) on the right-hand side is spin precession, spin relaxation and spin diffusion, respectively.

---

[2] The author acknowledges the suggestion of Dr. Takahashi. See table of integrals series and product by Gradshteyn & Ryzhik 3.325 pp. 307

At first, the simplest case, the Hanle effect without spin absorption is considered. Bloch-Torrey equation under the spin injection in the stationary state is expressed as [27, 28]

$$\begin{cases} 0 = -\omega_{\mathrm{L}} m_y - \dfrac{m_x}{\tau_{\mathrm{sf}}} + D_{\mathrm{N}} \nabla^2 m_x, \\ 0 = \omega_{\mathrm{L}} m_x - \dfrac{m_y}{\tau_{\mathrm{sf}}} + D_{\mathrm{N}} \nabla^2 m_y + \dfrac{\hbar \gamma_{\mathrm{e}}}{2e} \dfrac{I_{\mathrm{m}}}{A_{\mathrm{N}}} \delta(x). \end{cases} \tag{2.33}$$

where I_{m} is the injection spin current, x is the NM wire direction and y is the spin polarization of the injection spin current. The magnetization is therefore expressed with complex representation as

$$\tilde{m}(x) = m_y(x) + i m_x(x), \tag{2.34}$$

where

$$\tilde{m} = \frac{\hbar \gamma_{\mathrm{e}}}{2e} \frac{1}{D_{\mathrm{N}}} \frac{I_{\mathrm{m}}}{A_{\mathrm{N}}} \lambda_\omega \exp(-|x|/\lambda_\omega), \tag{2.35}$$

with

$$\lambda_\omega = \frac{\lambda_{\mathrm{N}}}{\sqrt{1 + i\omega_{\mathrm{L}} \tau_{\mathrm{sf}}}}. \tag{2.31}$$

It is convenient to introduce a complex spin accumulation $\delta\tilde{\mu}_{\mathrm{N}}(x) = \tilde{m}(x) / [2\mu_{\mathrm{B}} N(\varepsilon_{\mathrm{F}})]$, the real part of which relates spin accumulation

$$\delta\tilde{\mu}_{\mathrm{N}} = \frac{I_{\mathrm{m}}}{eN(\varepsilon_{\mathrm{F}}) A_{\mathrm{N}}} \frac{\tau_{\mathrm{sf}}}{2\lambda_{\mathrm{N}}} \left[\frac{\lambda_\omega}{\lambda_{\mathrm{N}}} \exp(-|x|/\lambda_\omega) \right], \tag{2.36}$$

which gives left hand side of eqn.(2.28) with $I_{\mathrm{m}} = P_{\mathrm{I}} I$, $V = \mathrm{Re}[\delta\tilde{\mu}_{\mathrm{N}}(x)] / e$ and gives the formula for Hanle signal with resistive junctions as eqn.(2.29). Thus the styles of the transit-time distribution and the Bloch-Torrey equation are consistent.

2.2.4 Hanle effect with spin absorption

In order to describe the Hanle effect with spin absorption, we start from Bloch-Torrey equation in the form of

$$\frac{\partial \mathbf{m}_{\mathrm{N}}}{\partial t} = -\gamma_e \left[\mathbf{m}_{\mathrm{N}}(\mathbf{r}) \times \mathbf{B}\right] - \frac{\mathbf{m}_{\mathrm{N}}}{\tau_{\mathrm{sf}}} + D_{\mathrm{N}} \nabla^2 \mathbf{m}_{\mathrm{N}}(\mathbf{r}) + \frac{\hbar \gamma_{\mathrm{e}}}{2e} \frac{I_{\mathrm{s1}}^{x}}{A_{\mathrm{N}}} \mathbf{e}_x \delta(x) + \frac{\hbar \gamma_{\mathrm{e}}}{2e} \frac{I_{\mathrm{s1}}^{y}}{A_{\mathrm{N}}} \mathbf{e}_y \delta(x) + \frac{\hbar \gamma_{\mathrm{e}}}{2e} \frac{I_{\mathrm{s2}}^{x}}{A_{\mathrm{N}}} \mathbf{e}_x \delta(x-L) + \frac{\hbar \gamma_{\mathrm{e}}}{2e} \frac{I_{\mathrm{s2}}^{y}}{A_{\mathrm{N}}} \mathbf{e}_y \delta(x-L), \tag{2.37}$$

where the last four terms represent the effect of spin injection/detection. The general solution of eqn.(2.37) is given by eqns.(2.33) and (2.35). The boundary conditions for transverse and longitudinal spins are

$$\begin{cases} I_{\mathrm{J}k}^{\,x,\sigma} = G_{\mathrm{I}k}^{\,\sigma}\, \mathrm{Re}\left[\dfrac{\tilde{\mu}_{\mathrm{N}}{}^{\sigma}(x)}{e} - \dfrac{\tilde{\mu}_{\mathrm{F}k}{}^{\sigma}(z)}{e}\right]\Big|_{k\text{-th junction}}, \\ I_{\mathrm{S,J}k}^{\,y} = I_{\mathrm{J}k}^{\,y,\uparrow} - I_{\mathrm{J}k}^{\,y,\downarrow} = 2G_{\uparrow\downarrow,k}\, \mathrm{Im}\left[\dfrac{\tilde{\mu}_{\mathrm{N}}(x)}{e} - \dfrac{\tilde{\mu}_{\mathrm{F}k}(z)}{e}\right]\Big|_{k\text{-th junction}}, \end{cases} \tag{2.38}$$

where $I_{\mathrm{J}k}^{x,\sigma}$ and $I_{\mathrm{J}k}^{y,\sigma}$ are the current with the spin polarization σ (=↑,↓) in x (y) direction, $I_{\mathrm{S,J}k}^{y}$ is the transverse spin current, $\delta\tilde{\mu}_{\mathrm{F},k}(\mathrm{z})$ is the complex spin accumulation of k-th FM and $G_{\uparrow\downarrow,k}$ is the real part of the spin mixing conductance of k-th junction. Eqn.(2.38) reduces to eqn.(2.15) when the transverse spin component (all the imaginary part) is zero.

After the long algebra, one arrives at

$$\hat{X}\begin{pmatrix} I_{s1}^{y} \\ I_{s2}^{y} \\ I_{s1}^{x} \\ I_{s2}^{x} \end{pmatrix} = 2\left(\frac{P_{\mathrm{I1}}}{1-P_{\mathrm{I1}}^2}\frac{R_{\mathrm{I}}}{R_{\mathrm{N}}} + \frac{P_{\mathrm{F1}}}{1-P_{\mathrm{F1}}^2}\frac{R_{\mathrm{F1}}}{R_{\mathrm{N}}}\right)\begin{pmatrix} I \\ 0 \\ 0 \\ 0 \end{pmatrix}, \tag{2.39}$$

with the matrix

$$\hat{X} = \begin{pmatrix} r_{1\parallel} + \mathrm{Re}[\bar{\lambda}_\omega] & \mathrm{Re}[\bar{\lambda}_\omega e^{-L/\tilde{\lambda}_\omega}] & -\mathrm{Im}[\bar{\lambda}_\omega] & -\mathrm{Im}[\bar{\lambda}_\omega e^{-L/\tilde{\lambda}_\omega}] \\ \mathrm{Re}[\bar{\lambda}_\omega e^{-L/\tilde{\lambda}_\omega}] & r_{2\parallel} + \mathrm{Re}[\bar{\lambda}_\omega] & -\mathrm{Im}[\bar{\lambda}_\omega e^{-L/\tilde{\lambda}_\omega}] & -\mathrm{Im}[\bar{\lambda}_\omega] \\ \mathrm{Im}[\bar{\lambda}_\omega] & \mathrm{Im}[\bar{\lambda}_\omega e^{-L/\tilde{\lambda}_\omega}] & r_{1\perp} + \mathrm{Re}[\bar{\lambda}_\omega] & \mathrm{Re}[\bar{\lambda}_\omega e^{-L/\tilde{\lambda}_\omega}] \\ \mathrm{Im}[\bar{\lambda}_\omega e^{-L/\tilde{\lambda}_\omega}] & \mathrm{Im}[\bar{\lambda}_\omega] & \mathrm{Re}[\bar{\lambda}_\omega e^{-L/\tilde{\lambda}_\omega}] & r_{2\perp} + \mathrm{Re}[\bar{\lambda}_\omega] \end{pmatrix}, \qquad (2.40)$$

where $\bar{\lambda}_\omega = \tilde{\lambda}_\omega / \lambda_{\mathrm{N}}$ and

$$r_{k\parallel} = \left(\frac{2}{1-P_{\mathrm{I}k}^2} \frac{R_{\mathrm{I}k}}{R_{\mathrm{N}}} + \frac{2}{1-p_{\mathrm{F}k}^2} \frac{R_{\mathrm{F}k}}{R_{\mathrm{N}}} \right), \quad r_{k\perp} = \frac{1}{R_{\mathrm{N}} A_{\mathrm{I}k} G_k^{\uparrow\downarrow}}, \quad (k = 1,2) . \qquad (2.41)$$

The boundary conditions also lead to the non-local voltage V due to the spin accumulation detected by F2,

$$V = -\left(\frac{P_{\mathrm{F2}}}{1-P_{\mathrm{F2}}^2} \frac{R_{\mathrm{F2}}}{R_{\mathrm{N}}} + \frac{P_{\mathrm{I2}}}{1-P_{\mathrm{I2}}{}^2} \frac{R_{\mathrm{I2}}}{R_{\mathrm{N}}} \right) R_{\mathrm{N}} I_{s2}^{y}, \qquad (2.42)$$

where the minus sign indicates the absorption of spin current by F2. Using the solution of the matrix eqn.(2.39), one obtains the non-local resistance

$$\frac{V}{I} = -2R_{\mathrm{N}} \left(\frac{P_{\mathrm{F1}}}{1-P_{\mathrm{F1}}^2} \frac{R_{\mathrm{F1}}}{R_{\mathrm{N}}} + \frac{P_{\mathrm{I1}}}{1-P_{\mathrm{I1}}^2} \frac{R_{\mathrm{I1}}}{R_{\mathrm{N}}} \right) \left(\frac{P_{\mathrm{F2}}}{1-P_{\mathrm{F2}}^2} \frac{R_{\mathrm{F2}}}{R_{\mathrm{N}}} + \frac{P_{\mathrm{I2}}}{1-P_{\mathrm{I2}}{}^2} \frac{R_{\mathrm{I2}}}{R_{\mathrm{N}}} \right) \frac{C_{12}}{\det(\hat{X})}, \qquad (2.43)$$

where $\det(\hat{X})$ is the determinant of the matrix $\hat{X}$ in eqn.(2.39) and C_{12} is the (1, 2) component of the cofactors of $\hat{X}$,

$$C_{12} = -\det \begin{pmatrix} \mathrm{Re}[\bar{\lambda}_\omega e^{-L/\tilde{\lambda}_\omega}] & -\mathrm{Im}[\bar{\lambda}_\omega e^{-L/\tilde{\lambda}_\omega}] & -\mathrm{Im}[\bar{\lambda}_\omega] \\ \mathrm{Im}[\bar{\lambda}_\omega] & r_{1\perp} + \mathrm{Re}[\bar{\lambda}_\omega] & \mathrm{Re}[\bar{\lambda}_\omega e^{-L/\tilde{\lambda}_\omega}] \\ \mathrm{Im}[\bar{\lambda}_\omega e^{-L/\tilde{\lambda}_\omega}] & \mathrm{Re}[\bar{\lambda}_\omega e^{-L/\tilde{\lambda}_\omega}] & r_{2\perp} + \mathrm{Re}[\bar{\lambda}_\omega] \end{pmatrix}. \qquad (2.44)$$

When junctions 1 and 2 are tunnel junctions ($R_{Ik} \gg R_N, R_{Fk}$), eqn.(2.43) reduces to eqn.(2.30)

$$\frac{V}{I} = \frac{1}{2} P_{I1} P_{I2} R_N \,\mathrm{Re}\left[\left(\tilde{\lambda}_\omega / \lambda_N \right) \exp(-L / \tilde{\lambda}_\omega) \right]. \tag{2.45}$$

In the absence of perpendicular magnetic field, eqn.(2.43) reduces to the previous result of eqn.(2.16).

2.2.5 Magnetization process

In the perpendicular magnetic field, FM changes its direction of magnetization. This magnetization process affect Hanle signal because the perpendicular magnetic field in Hanle measurement affect the direction of the magnetizations of injector and detector. In this section we shortly describe the magnetization process and its effect on Hanle signal.

The magnetization process of FM is determined by the crystal anisotropy and the shape anisotropy [31]. In order to study Hanle effect, FM wire of LSV is designed to make the magnetization state of FM uniform magnetization. In such a case, the magnetization under the external magnetic field is described by the Stoner-Wohlfarth model [32, 33]. The direction of the magnetization is determined to minimize the total energy E, which consists of the demagnetizing energy E_D and the energy associated with the applied field E_H. In the case of the ellipsoid,

$$E = E_D + E_H, \tag{2.46}$$

$$E_D = \frac{1}{2} {I_0}^2 (N_1 \alpha_1'^2 + N_2 \alpha_2'^2 + N_3 \alpha_3'^2), \tag{2.47}$$

$$E_H = -H I_0 \cos\phi, \tag{2.48}$$

where I_0 is the intensity of the magnetization, $\alpha_1'^2, \alpha_2'^2, \alpha_3'^2$ are the direction of the cosines of I_0 with respect to the principal axes. N_1, N_2, N_3 are the demagnetization coefficients along these axes. We assume that the magnetization lie in the plane defined by the direction of the field and of the polar axis of the ellipsoid.[3] In this plane let θ be the angle between the polar axis and the positive direction of H , ϕ the angle between I_0 and H, and the ψ the angle between the polar axis and I_0, so that

$$\phi = \theta + \psi. \tag{2.49}$$

The eqn.(2.47) reduces to

$$E_{\mathrm{D}} = \frac{1}{2} I_0{}^2 (N_a \cos^2 \psi + N_b \sin^2 \psi), \tag{2.50}$$

where $N_b = 2\pi - N_a/2$. Then the variable part of the total energy is expressed as

$$E = -\frac{1}{4}\cos 2(\phi - \theta) - h\cos\phi + \text{constant}, \tag{2.51}$$

where $h = I_0 H/(N_b - N_a)$. Now the magnetization process in LSV is considered. The magnetic field in perpendicular to the easy axis of the FM ($\theta = \pi/2$) and thus

$$E = -\frac{1}{4}\sin 2\phi - h\cos\phi + \text{constant}. \tag{2.52}$$

$$\frac{\partial E}{\partial \phi} = -\frac{1}{2}\cos 2\phi + h\sin\phi = 0. \tag{2.53}$$

[3] This assumption is validated in sec.5 of [32]. For Hanle measurement, we do not need the proof of the general case. The applied field is fixed to the perpendicular to the cuboid nanowire. Thus the magnetization is in the plane defined by the field and the easy axis of the magnet.

As a consequence, typical magnetization process can be simulated by using the saturation field of Py of 1 T and the demagnetization coefficient of 0.7 for FM nanowire as shown in Fig. 2.9.

The effect of the magnetization process on the spin accumulation can be described by considering the vector spin polarization $P\mathbf{e}^{\mathrm{FM}i}$ to y and z-axis and its projection as shown in Fig. 2.10 [23].

$$\frac{V}{I} = R_{\mathrm{S}}^{\mathrm{Hanle}}\left(\omega_{\mathrm{L}}, \mathbf{e}^{\mathrm{FM1}}\bullet\mathbf{e}_y, \mathbf{e}^{\mathrm{FM2}}\bullet\mathbf{e}_y\right) + R_{\mathrm{S}}^{\mathrm{Hanle}}\left(0, \mathbf{e}^{\mathrm{FM1}}\bullet\mathbf{e}_z, \mathbf{e}^{\mathrm{FM2}}\bullet\mathbf{e}_z\right), \tag{2.54}$$

with

$$R_{\mathrm{S}}^{\mathrm{Hanle}}(\omega_{\mathrm{L}}, a^{\mathrm{FM1}}, a^{\mathrm{FM2}}) = \frac{1}{2}P_{\mathrm{I}}^2 R_{\mathrm{N}}\,\mathrm{Re}\left[\left(\lambda_\omega/\lambda_{\mathrm{N}}\right)\exp(-L/\lambda_\omega)\right], \tag{2.55}$$

where $a^{\mathrm{FM}i}$ is the projection of the unit vector of the magnetization of FMi $\mathbf{e}^{\mathrm{FM}i}$ on y- or z-axis. Each term shows the contribution of the injected spin with the polarization of y-axis with spin precession and the injected spin with the polarization of z-axis without spin precession.

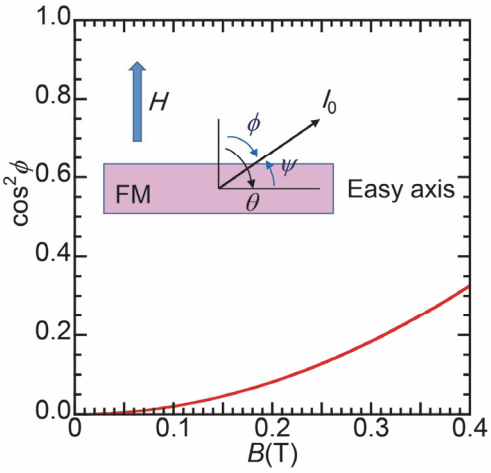

Figure. 2.9: The direction of magnetization I_0 as a function of the field applied $B=\mu_0 H$. Data are calculated for Py.

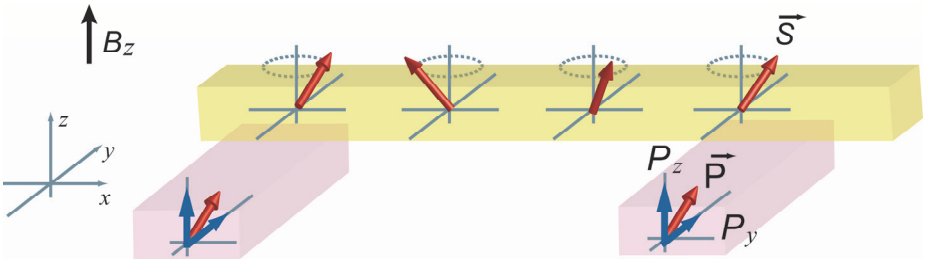

Figure 2.10: Spin precession and magnetization under perpendicular magnetic field B_z. The magnetization of FMs is tilted up toward the z axis and then the polarization **P** has nonzero z component P_z. The tilted spins injected into NM precess in the x-y plane.

2.2.6 Hanle effect in three terminal geometry

In the metallic system, the spin relaxation time is smaller and the diffusion constant is higher compared to semiconductors. It requires higher magnetic field and hence the effect of the magnetization process is not negligible [23, 26, 33, 34]. In such a case, Hanle effect in multi-terminal structure is of benefit because the background signal due to the magnetization process is suppressed and the spin-precession signal is pronounced (sec. 6.3 and Fig. 6.6 (b)). In general, the Hanle effect in the multiterminal geometry can be obtained by the scheme described by the sec. 2.2.4 with the magnetization process in sec. 2.2.5. Assuming that $R_I >> R_N$, the non-local resistance R_S^{Hanle} is calculated by using Bloch-Torrey equation [23]

$$R_S^{Hanle} = \frac{1}{2} R_N P_I^2 \times \mathrm{Re}[(\lambda_\omega/\lambda_N)\exp(-L/\lambda_\omega)\{\cos\theta_{y2}\cos\theta_{y3} - 2\cos\theta_{y1}\cos\theta_{y3}\exp(-d_{12}/\lambda_\omega) + \cos\theta_{y2}\cos\theta_{y3}\exp(-2d_{12}/\lambda_\omega)\}], \quad (2.56)$$

where $\cos\theta_{yj} = \mathbf{e}_y \cdot \mathbf{e}^{FMj}$. When the precession angle during the transport between FM1 and FM2 is negligiblly small, i.e., $d_{12} << L$, it is given by

$$R_{\mathrm{S}}^{\mathrm{Hanle}} \approx \{\cos\theta_{y2}\cos\theta_{y3} - 2\cos\theta_{y1}\cos\theta_{y3}\exp(-d_{12}/\lambda_{\mathrm{N}}) + \cos\theta_{y2}\cos\theta_{y3}\exp(-2d_{12}/\lambda_{\mathrm{N}})\} \times \frac{1}{2} R_{\mathrm{N}} P_{\mathrm{I}}^2 \,\mathrm{Re}\left[\left(\lambda_{\omega}/\lambda_{\mathrm{N}}\right)\exp(-L/\lambda_{\omega})\right]. \tag{2.57}$$

In the antiparallel configuration between FM1 and FM2 with $\cos\theta_{y1} = -\cos\theta_{y2}$, we obtain the simple expression,

$$R_{\mathrm{S}}^{\mathrm{Hanle}} \approx \frac{\alpha_{\max}}{2} R_{\mathrm{N}} P_{\mathrm{I}}^2 \cos\theta_{y2}\cos\theta_{y3}\,\mathrm{Re}\left[\left(\lambda_{\omega}/\lambda_{\mathrm{N}}\right)\exp(-L/\lambda_{\omega})\right]. \tag{2.58}$$

2.3 Spin relaxation mechanism

2.3.1 Introduction

Spin relaxation mechanism in solid has been intensively studied for a long time not only for the fundamental interest but also for the spintronics applications. So far, three types of the spin relaxation mechanism has been found to be relevant for the conduction electrons: the Elliott-Yafet [35, 36], D'yakonov-Perel' [37, 38] and Bir-Aronov-Pikus [39].

2.3.2 Elliott-Yafet mechanism

In the Elliott-Yafet mechanism, the spin-orbit interaction (SOI) plays a key role. Firstly, we consider the simple case where Bloch states of different spins |+> and |-> ("up"- and "down"-) are subjected to the momentum scatterings such as phonon scattering, NM impurity scattering and grain boundary scattering. The spin relaxation time τ_{sf} is inversely proportional to the scattering matrix as $1/\tau_{\mathrm{sf}} \propto |\langle +|\mathcal{H}|-\rangle|^2$, where $\mathcal{H}$ is the Hamiltonian. Therefore, the spin-independent scatterings alone do not induce spin relaxation. However, in real crystal, the SOI mixed the spin-"up" state and spin-"down" state. The SOI is usually much smaller than the typical band width ΔE. Therefore, with taking the perturbative

approach, original “up” state becomes the admixture of the original “up” state and the little “down” state of the order of $\lambda_{SOI}/\Delta E$ where λ_{SOI} is the spin-orbit splitting [35, 36]. That is, the “new” spin up-state $|\uparrow> \approx |+> + (\lambda_{SOI}/\Delta E)|->$ has non-zero transition probability to $|\uparrow>$ and the spin relaxation time is proportional to the momentum relaxation time τ_e and inversely proportional to the square of the SOI in the first order.

2.3.3 D’yakonov-Perel’ and Bir-Aronov-Pikus mechanism

D’yakonov-Perel’ mechanism: in crystal that lacks of the inversion symmetry (such as the zinc-blend semiconductror) the SOI lifts the spin-degeneracy, that is, spin-up and spin-down electrons have different energies even when in the same momentum state. This is equivalent to having a momentum-dependent internal magnetic field $\mathbf{B}(\mathbf{k})$ which can induce spin flips through the interaction term $\mathbf{B}(\mathbf{k}).\mathbf{S}$. The spin relaxation rate $1/\tau_{sf}$ is proportional to the momentum relaxation time τ_e.

Bir-Aronov-Pikus: spin relaxation mechanism is based on the electron-hole exchange interaction. This interaction depends on the spins of interacting electrons and act as an effective magnetic field. This is relevant only in the semiconductors with a significant overlap between electron and hole wave functions [40].

2.3.4 Effect of the electronic structure (spin hot spot)

Spin relaxation mechanism in metal is established as the Elliott-Yafet mechanism [40, 41]. As is described in sec 2.3.2, spin relaxation time is proportional to the charge relaxation time and thus the temperature dependence of the spin

relaxation time was tested. Monod and Beuneu [42] catalogued the spin relaxation time for various materials (Cu, Ag, Au, Al, Mg, Be, Cs, K, Na, Rb and Pd) and found that the normalized spin relaxation time is at least three orders of the magnitude different for *s*-state metals and the others. Fabian and Das Sarma theoretically found out that the electronic structure stongly affects the strength of spin relaxation [43]. In particular, the polyvalent metals (Al, Pd, Mg, and Be) contains the region where the spin relaxation is abnormally fast. Such a region ("spin hot spot") is near the Brillouin zone boundaries, special symmetry points, or lines of accidental degeneracy. Although such an area is small compared to the whole area, it affects the total spin relaxation time because the spin relaxation time is very short in the area.

References for chapter 2

[1] N. F. Mott, *Advances in Physics* **13**, 325 (1964).
[2] S. Takahashi and S. Maekawa, *Physical Review B* **67**, 052409 (2003).
[3] S. Takahashi and S. Maekawa, *Journal of the Physical Society of Japan* **77**, 031009 (2008).
[4] P. C. van Son, H. van Kempen, and P. Wyder, *Physical Review Letters* **58**, 2271 (1987).
[5] S. Hershfield and H. L. Zhao, *Physical Review B* **56**, 3296 (1997).
[6] E. I. Rashba, *The European Physical Journal B - Condensed Matter* **29**, 513 (2002).
[7] J. Bass and W. P. Pratt, *Journal of Physics: Condensed Matter* **19**, 183201 (2007).
[8] T. Valet and A. Fert, *Physical Review B* **48**, 7099 (1993).
[9] T. Kimura, J. Hamrle, and Y. Otani, *Physical Review B* **72**, 014461 (2005).
[10] T. Kimura, Y. Otani, and J. Hamrle, *Physical Review Letters* **96**, 037201 (2006).
[11] T. Yang, T. Kimura, and Y. Otani, *Nature Physics* **4**, 851 (2008).
[12] J. Z. Sun *et al.*, *Applied Physics Letters* **95**, 083506 (2009).
[13] D. Ilgaz *et al.*, *Physical Review Letters* **105**, 076601 (2010).
[14] A. T. Filip, B. H. Hoving, F. J. Jedema, B. J. van Wees, B. Dutta, and S. Borghs, *Physical Review B* **62**, 9996 (2000).
[15] M. Johnson and R. H. Silsbee, *Physical Review Letters* **55**, 1790 (1985).
[16] E. I. Rashba, *Physical Review B* **62**, R16267 (2000).
[17] A. Fert and H. Jaffrès, *Physical Review B* **64**, 184420 (2001).
[18] S. O. Valenzuela and M. Tinkham, *Applied Physics Letters* **85**, 5914 (2004).
[19] S. Valenzuela, D. Monsma, C. Marcus, V. Narayanamurti, and M. Tinkham, *Physical Review Letters* **94**, 196601 (2005).
[20] F. Jedema, A. T. Filip, and B. J. van Wees, *Nature* **410**, 345 (2001).
[21] A. Vogel, J. Wulfhorst, and G. Meier, *Applied Physics Letters* **94**, 122510 (2009).
[22] H. Jaffrès, J. M. George, and A. Fert, *Physical Review B* **82**, 140408(R) (2010).
[23] H. Idzuchi, Y. Fukuma, and Y. Otani, *Scientific reports* **2**, 628 (2012).
[24] H. Idzuchi, S. Karube, Y. Fukuma, T. Aoki, and Y. Otani, *Applied Physics Letters* **103**, 162403 (2013).
[25] M. Johnson and R. H. Silsbee, *Physical Review B* **37**, 5326 (1988).
[26] F. Jedema, H. Heersche, A. Filip, J. Baselmans, and B. J. van Wees, *Nature* **416**, 713 (2002).
[27] M. Johnson and R. H. Silsbee, *Physical Review B* **37**, 5312 (1988).
[28] Y. Fukuma, L. Wang, H. Idzuchi, S. Takahashi, S. Maekawa, and Y. Otani, *Nat Mater* **10**, 527 (2011).
[29] F. Bloch, *Physical Review* **70**, 460 (1946).
[30] H. C. Torrey, *Physical Review* **104**, 563 (1956).
[31] S. Chikazumi, *Physics of ferromagnetism* (Oxford : Clarendon Press, 1997), Internat. Ser. Mono. Phys. **94**.

[32] E. C. Stoner and E. Wohlfarth, *Philosophical Transactions of the Royal Society of London. Series A. Mathematical and Physical Sciences* **240**, 599 (1948).
[33] G. Mihajlović, J. E. Pearson, S. D. Bader, and A. Hoffmann, *Physical Review Letters* **104**, 237202 (2010).
[34] S. O. Valenzuela and M. Tinkham, *Nature* **442**, 176 (2006).
[35] R. J. Elliott, *Physical Review* **96**, 266 (1954).
[36] Y. Yafet, *Solid State Physics* **14**, 1 (1963).
[37] M. D'yakonov and V. Perel, *Soviet Journal of Experimental and Theoretical Physics* **33**, 1053 (1971).
[38] M. D'yakonov and V. Perel, *Sov. Phys. Solid State* **13**, 3023 (1972).
[39] G. Bir, A. Aronov, and G. Pikus, *Soviet Journal of Experimental and Theoretical Physics* **42**, 705 (1975).
[40] J. Fabian and S. Das Sarma, *Journal of Vacuum Science & Technology B: Microelectronics and Nanometer Structures* **17**, 1708 (1999).
[41] I. Žutić, J. Fabian, and S. D. Sarma, *Reviews of modern physics* **76**, 323 (2004).
[42] P. Monod and F. Beuneu, *Physical Review B* **19**, 911 (1979).
[43] J. Fabian and S. Das Sarma, *Physical Review Letters* **81**, 5624 (1998).

Chapter 3

Device fabrication and measurement technique

3.1 Device fabrication

The modern device-fabrication technique opens the way to study spin transport phenomena in the nanometer scale, which is shorter than that of the characteristic length. In this section, the principle and the procedure of fabrication of lateral spin valve (LSV) devices are shortly summarized.

3.1.1 Steps of the fabrication procedure

Samples were fabricated in the following steps, as shown in Fig. 3.1. Firstly, 3-5 inches Si-substrates with SiO_2 layer was cut into pieces. Next, Ti/Au electrodes were fabricated by using photo-lithography. Then, the metallic lateral spin valves were fabricated by *e*-beam lithography. After the evaporation and subsequent lift-off, annealing process (heat treatment) was performed.

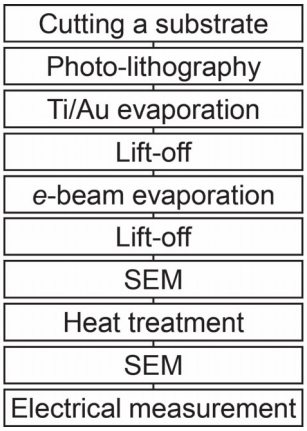

Figure 3.1: Steps of sample fabrication.

3.1.2 Photo-lithography

Photo-lithography enables to fabricate a micro-meter scale resist-mask. The electrodes and a positioning mark for *e*-beam lithography were patterned by photo-lithography. In this study, mask-less photo-lithography, D-light-DL1000RS Mask-less UV Lithography System where digital mirror devices control the position of laser, was used. The recipe is shown below

(1) A Si substrate (with SiO_2 layer) was cut into appropriate size, e.g. square 20 mm on a side.

(2) Cleaning of the substrate. After an ultrasonic cleaning with a high power in acetone for 10 minutes, it was dried with an air gun. Subsequently, the substrate was cleaned by an ultrasonic cleaning with a high power in IPA (isopropyl alcohol) and it was dried with an air gun. Ultraviolet cleaning was performed for 10 min to remove remaining organics on the surface. After all, it was inspected with eyes that dust does not remain.

(3) Primer was coated. Primer (1,1,1,3,3,3,-Hexamethyldisilazane, $C_6H_{10}NSi_2$, HDMS) was spin-coated at 500 rpm-5 sec, 5000 rpm-40 sec.

(4) Soft bake by an oven for 5 min.

(5) Resist was coated. Resist (AZ1500) was spin coated at 500 rpm-5 sec, 5000 rpm-40 sec as a second layer.

(6) Soft bake by oven at 80 °C for 5 min.

(7) Laser beam exposure (the typical energy is 90 mJ/mm^2).

(8) Development. Shaking the sample in a developer for 60 sec. Subsequently, the sample was rinsed by flowing pure water with shaken by hand for approximately 30 sec and was dried by air gun.

3.1.3 Electron beam lithography

E-beam lithography enables to fabricate a nanometer scale resist-mask. Since minimum dimensions of the patterns were restricted by the wavelength of the source of the light, it enables to fabricate fine structures compared with photo-lithography. In this study, it was used to fabricate LSV (non-magnet (NM)/ferromagnet (FM) hybrid structure).

In order to fabricate LSV without air exposure (*in-situ*), three-dimensional resists patterns were used, i.e., double or triple resist layers were formed on substrates and fabricate three-dimensional structure because the resists have different sensitivities to the *e*-beam as shown in Fig. 3.2. The thickness of the resistss were determined by a SEM observation of the structures after the evaporation. The first and second layers were 500-nm-thick methyl-methacrylate (MMA) EL9 and 50-nm-thick polymethyl methacrylate (PMMA) 950A4, respectively. The recipe is shown below

(1) A Si substrate with Ti/Au electrodes was cleaned. After an ultrasonic cleaning with a low power in acetone for 10 minutes, it was dried with an air gun. Subsequently, the substrate was cleaned by an ultrasonic cleaning with a low power in IPA for 10 minutes, and it was dried with an air gun. Ultraviolet cleaning was performed for 5 minutes to remove remaining organics on the surface. After all, it was inspected with eyes that dust does not remain.

(2) MMA-EL9 resist was spin coated at slope-5 sec, 500 rpm-10 sec, 1500 rpm-90 sec and slope-10 sec.

(3) Soft bake. The sample was baked by oven at 180 °C for 30 min or heated on a hot plate at 180 °C for 90 sec.

(4) PMMA-950A4 resist was spin coated in 500 rpm-5 sec, 5000 rpm-40 sec and slope-5 sec.

(5) Soft bake by oven at 180 °C for 30 min or on a hot plate at 180 °C for 90 sec.

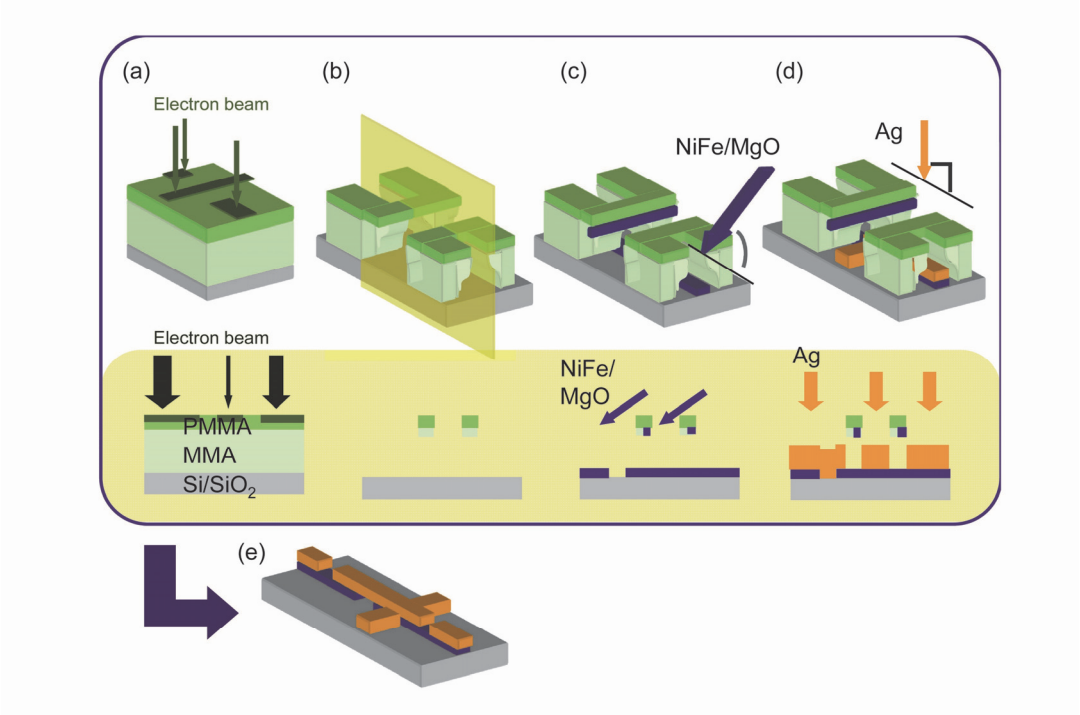

Figure 3.2: Schematics of three-dimensional resist for shadow evaporation. Upper and lower cases show cubic diagram and cross-section diagram ultrasonic the projection on the plane shown in the upper case), respectively. (a) Exposure area of *e*-beam. (b) Resist structure after development. (c) Shadow evaporation of NiFe/MgO. The substrate was tilt from normal. (d) Evaporation of Ag at the angle normal to the substrate. (e) Device structure after removing the resists (lift-off).

(6) Electron beam exposure. (typical dose time is 0.70 micro sec in 2.5 nm^2 in the beam condition of the acceleration voltage of 100 kV and the beam current of 100 pA)

(7) Development. The sample is soaked in a developer for 30 sec. Subsequently, the sample was rinsed by IPA with shaken by hand for 60 sec and was dried by air gun. The developer was made by mixing MIBK (methyl isobutyl ketone) with IPA (volume ratio is 1:3).

3.1.4 Deposition

Electrodes were *e*-beam evaporated after fabricating resist masks.

3.1.4.1 Au electrode and positioning mark for *e*-beam lithography

5-nm-thick Ti and (20-400)-nm-thick Au were evaporated. Note: if the total thickness is larger than the thickness of LSV, electrical disconnections were often observed after the heat treatment.

3.1.4.2 Deposition for LSV

(1) FM was evaporated at the angle of 45 degree from normal to the substrate. Evaporation rate was 0.4-0.5 Å/s and the thickness was 20 nm (28 nm should be displayed in thickness monitor which is placed normal).

(2) MgO was evaporated at the same angle. LSVs with different MgO thickness were fabricated by using a moving shutter in the chamber.

(3) Sample was transferred to another chamber for depositing NM. In order to prevent contaminations of the NM from FM, the chamber was separated from that for FM. Liquid nitrogen was flowed in the cooling pipe to cool the substrate. After 30 min, non-magnetic layer was evaporated at the angle normal to the substrate. Typical thickness is 50 nm.

(4) In order to protect the sample from oxidization, MgO layer was evaporated at the angle normal to the substrate. Typical thickness is 5 nm.

3.1.5 Lift-off

After the deposition, unnecessary resists and layers were removed by soaking the sample in a remover. This process is called as lift-off.

(1) Au electrodes and positioning marks were soaked in acetone over 10 minutes. Subsequently, ultrasonic (power: low) was performed until the unnecessary part is removed (approximately for 30 sec).

(2) Lateral spin valves were soaked in acetone over 10 minutes. Subsequently, some of the samples were shaken (typically for 8 hours). After that the samples were rinsed by IPA and dried with an air gun. Note: Especially for Ag and Mg nanowires, ultrasonic cleaning damaged necessary part and thus it was not used. For Mg, even a shaker was not used to prevent the damage.

3.1.6 Heat treatment

After the lift-off, heat treatment was performed in the atmosphere of N_2(97.1%)+H_2(2.9%) at 400 °C in 40 min.

3.2 Measurement techniques

3.2.1 Wire bonding

Samples were wire bonded by the bonder model 7476D (West bond Inc). Typical parameters for 200-nm-thick Au electrodes at room temperature[4] were as follows. For Al bonding wire, Power(P) and Time(T) were of 250 and 30 ms, and 30 and 30 ms for first and second bond, respectively. For Au bonding wire, P and T were of 300 and 100 ms, and 200 and 100 ms for first and second bond, respectively.

[4] If the sample was heated (at typically 80°C) bonding becomes easy but damages LSVs.

3.2.2 Hanle measurement

Hanle measurement was performed by the vector magnet system (Suzuki shokan Ltd.) Two rotation axes are assembled in the system. Firstly, by using the sample rotation system, the sample plane (substrate) was aligned to be parallel to the rotation axis of the magnet[5]. Subsequently, by using the magnet rotation system, the non-local spin valve measurement at the 0 degree of magnet and the Hanle measurement at around 90 degree of magnet were performed. Figure 3.3 shows the magnet angle dependence of the Hanle signal. If the angle was deviated from the correct perpendicular direction, the magnetization of LSVs are switched probably due to the in-plane component of the magnetic field. Therefore, before the Hanle measurement was started the calibration was performed.

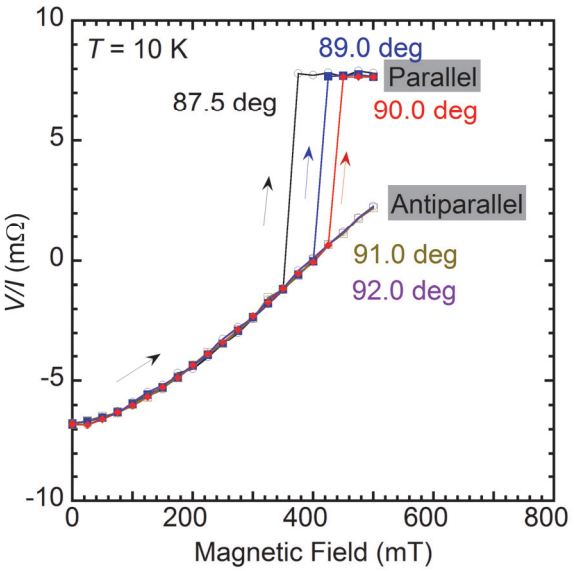

Figure 3.3: Hanle signal for different magnetic field direction. After the initialization (antiparallel state of injector-detector magnetization), the non-local resistance was measured.

[5] After the angle of LSV was calibrated by the eyes at room temperature, the sample rotation system cannot be used at low temperature.

3.2.3 Electrical measurement

Electrical measurement was performed by using conventional current-bias lock-in technique (LI5640: NF corporation) or by a dc current source and nano-voltmeter (2182A: Keithley). Lock-in technique enables to detect tiny signal at a low frequency (79 Hz in this study). Therefore, it was used to detect the small signal such as Mg based LSVs. The DC measurement is not as good S/N as lock-in technique but enables to make duration time short. Thus, it is beneficial to apply high current. The electrode configurations of non-local resistance and the interface resistance are shown in the sec. 5.2.2 and sec. 5.3.2.

Chapter 4

Enhanced spin accumulation in lateral spin valves

4.1 Introduction

Pure spin current is a flow of spin angular momentum with no accompanying charge current. Non-local spin injection in lateral spin valves (LSVs) has proven to be an effective method to generate the pure spin current I_S flowing along the slope of the spin accumulation, which decays exponentially with a factor of $\exp(-d/\lambda_{sf})$ where d is the distance from the interface and λ_{sf} is the spin diffusion length in the non-magnetic (NM) wire [1, 2]. Subsequent spin relaxation takes place in an additional ferromagnet (FM) in Ohmic contact with the NM wire sustaining the spin accumulation. This is so-called spin absorption and provides an attractive means to manipulate the magnetization in magnetic nanostructures [3-6]. Therefore, it is more beneficial to develop a more efficient way to generate a large spin accumulation for advancement of spintronic devices using lateral geometry. However the amplitude of the voltage change ΔV_S between anitiparallel and parallel alignments of the magnetization of the two ferromagnetic (FM) wires detected at the second FM wire in LSVs typically of the order of 1 μV. The non-local measurement involves no charge-current flows but spin accumulation in the vicinity of the detector. The spin accumulation is the difference in the electro chemical potential between majority and minority spins, that is, ΔV_S is the measurable physical quantity and also determines the magnitude of pure spin current absorbed into the detector FM. Therefore, efficient spin injection into the non-magnet (NM) from the FM, being proportional to the spin signal $\Delta R_S = \Delta V_S/I$, and high applied

current *I* are indispensable in realizing further enhancement of the spin accumulation [7-14].

In the first part of the Chapter 4, we report on the effect of the interface on the spin accumulation in metallic LSVs with $Ni_{80}Fe_{20}$ (Permalloy, Py)/MgO/Ag junctions. According to the spin-resistance mismatch model, the effect of the junction is expected to strongly affect the injection efficiency of spin current. The spin injection properties of various Py/MgO/Ag junctions was investigated and the low areal resistance around 0.2 $\Omega\mu m^2$ of the interface MgO layer could effectively overcome the spin-resistance mismatch between Py and Ag and leads to significant enhancement of the spin accumulation.

In the second part of the Chapter 4, we report on the optimized device structure for non-local spin injection using lateral geometry. Non-local spin injection was first demonstrated in 1985 using micro-scale devices which consist of a 50-μm-thick Al bar with FM junctions [15]. This experiment yielded a tiny spin accumulation signal of a few tens of pico-volts. The experiment was revisited in 2001 using nano-scaled LSVs [16]. This brought about an enhanced signal of about one micro-volt at room temperature (RT), which spurred intensive research efforts in non-local LSVs for spintronic device applications. When the *I* is applied across a FM/NM junction at the injector in LSVs, I_S is injected from the FM to the NM and then diffuses toward the detector [2, 17, 18]. For the *micro-scale* NM, the injected spins diffuse in any direction and a little part of them can reach to the detector. In contrast, the spin diffusion is restricted along the NM wire in *nano-scale* LSVs because the cross sectional area is much smaller dimension than the spin diffusion length λ_N. This reduces unwanted spin relaxation in the NM and thus the detected spin accumulation signal is dramatically improved [19]. In the light of this history, removing the spin relaxation volume is an effective scheme to enhance the spin accumulation generated in NM. Recently, Jaffrès *et al.* also theoretically pointed out that spin accumulation is enhanced by confined

geometries and mutiterinal structure [20]. In the section 4.5, we study the specially designed LSVs to enhance spin accumulation.

4.2 The effect of MgO insertion in Py and Ag based LSVs

4.2.1. Digest of device fabrication

In this study, we used Py as FM, Ag as NM and MgO as an insertion layer. Py has small crystal magnetic anisotropy which makes it easy to control switching field by the shape of electrodes. Also, it shows strong oxidative resistance, which makes the fabrication procedure simple. Ag is good spin conductor because spin diffusion length is long [12], and interfacial spin polarization in Ag/FM interface is high [21]. MgO is chosen because FM/MgO/FM magnetic tunnel junction shows high spin polarization [22, 23].

LSVs with clean Py/MgO/Ag junction were fabricated *in-situ* as detailed in the chapter 3. In order to keep clean interface, all Py, MgO and Ag layers were evaporated without air exposure. The SEM image after the heat treatment was shown in Fig. 4.1. The widths and thicknesses of wires were w_{Ag} = 160 nm, t_{Ag} = 50 nm, w_{Py} = 140 nm, and t_{Py} = 20 nm for Ag and Py, respectively. As shown in Fig. 4.1, the sample consists of three parts: a Ag layer, Py/MgO bilayer and Py/MgO/Ag trilayer. The center of the sample consists of two Py/MgO wires bridged by a NM Ag wire. The remaining wires and pads mainly consist of Py/MgO/Ag trilayer. The gap between Py/MgO/Ag trilayer and the Ag wire in the center was approximately 100 nm. Since the spin diffusion length of Py was 5 nm [24], 100 nm separation was enough to separate spin transport of LSV from the remaining parts.

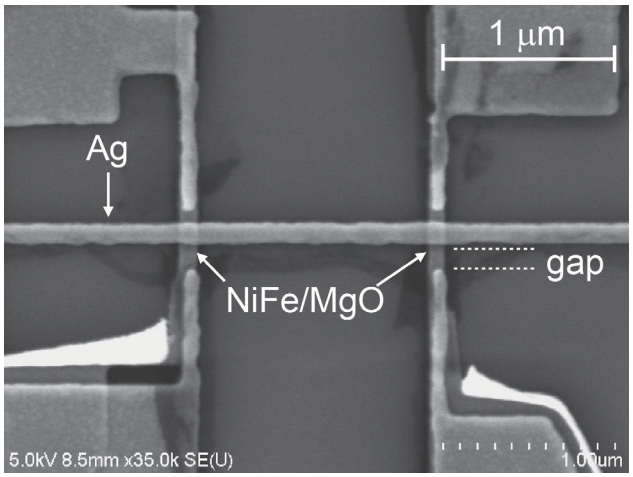

Figure 4.1: Scanning electron microscope image (SEM) of fabricated lateral spin valve.

4.3 Experimental result (before annealing)

4.3.1 Thickness dependence of interfacial resistance

Figure 4.2 shows the thickness dependence of interface resistance of Py/MgO/Ag junctions. In order to normalize the interface resistance by the dimensions, areal resistance $R_{IA} \equiv R_I w_{Ag} w_{Py}$ was used where R_I is the junction resistance of

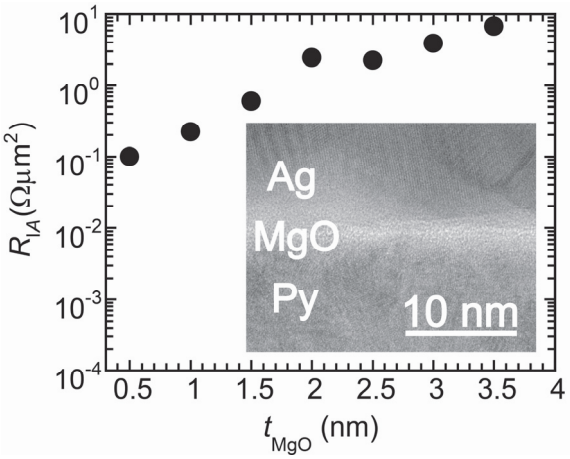

Figure 4.2: MgO thickness dependence of R_{IA}. Inset shows cross-sectional TEM image for Py/MgO(0.5 nm)/Ag junctions.

Py/MgO/Ag or the interface resistance of Py/Ag. The interface resistance exponentially increases as the MgO thickness increases. Although this is similar properties of magnetic tunnel junctions [22, 23], the value of the junction resistance is small and the *I-V* characteristics shows linear behavior for the sample in this study. The inset of Fig. 4.2 shows the cross-sectional transmission electron micrograph of the junction. It reveals that amorphous MgO is uniform and there is no pin-hole. The small junction resistance is attributed to the oxygen vacancies of the junction [25].

4.3.2. Spin valve measurement

Figure 4.3 shows the result of spin valve measurement for LSV with L = 300 nm. The spin valve signal was observed in which magnetizations shows parallel and antiparallel configuration with the reasonable switching field. One of the 140-nm-wide FM wires attached to the micro-meter pads. The magnetic domain wall nucleation in the pad and subsequent change of the domain structure reduces the switching field (see Fig. 5.1). It enables to use the FM wires with the same width for LSVs, which makes the analysis simple.

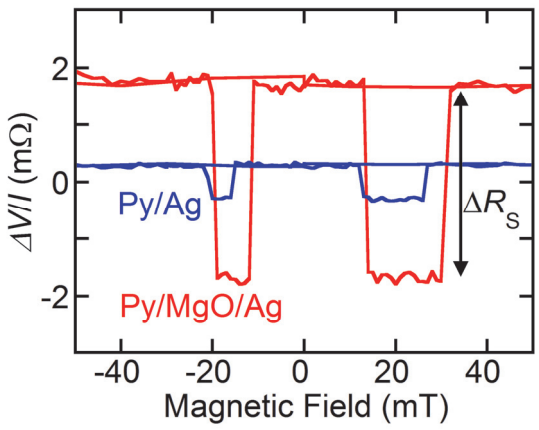

Figure 4.3: Non-local spin valve signal for lateral spin valve with Py/Ag junctions and Py/MgO(0.5 nm)/Ag junctions at T = 10 K.

4.3.3. Interface resistance dependence of spin accumulation

Figure 4.4 shows the interface resistance dependence of ΔR_S for LSVs with L = 300 nm, 500 nm, and 1000 nm for RT and 10 K. Each case shows the increase of the spin accumulation with an increase of the interface resistance and ΔR_S shows a maximum at the specific R_I. According to the model in chapter 2 (see eqn.(2.16)), ΔR_S increase with an increase of interface resistance and is expected to saturate. The observed peak structure is interpreted as the decrease of the spin polarization in the high interface resistance regime. The spin cannot transmit and relaxes in the high resistance (thick) MgO layer, which is attributed to the poor crystalline quality and electrically leaky properties of pristine Py/MgO/Ag junctions.

4.4 Experimental result (after annealing)

4.4.1. Change of interfacial resistance after annealing

Figure 4.5 shows the thickness dependence of interface resistance of Py/MgO/Ag junctions at RT both for annealed samples and pristine ones. The junction resistance exponentially increases with an increase in the thickness of MgO. This

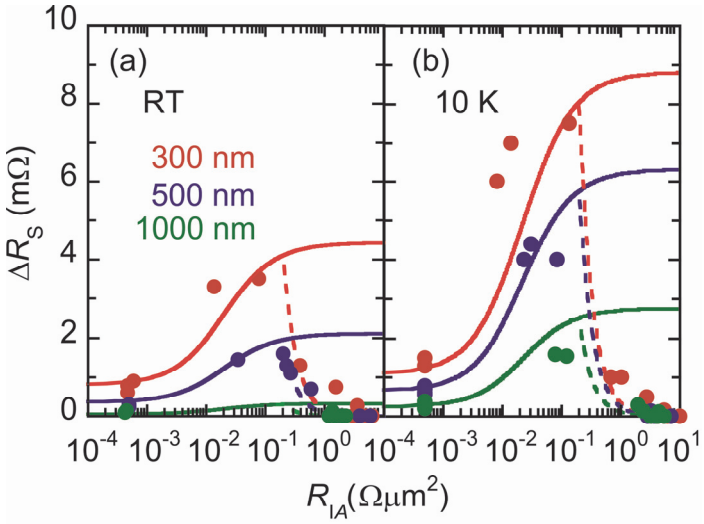

Figure 4.4: (a) R_{IA} dependence of spin signal ΔR_S with separation L = 300 nm, 500 nm, and 1000 nm at RT (b) at T = 10 K.

tendency is consistent with reported magnetic tunnel junction [22, 23] but the junction resistance in this study was much smaller. The character X-ray analysis revealed that the amount of oxygen is decreased by 6 % after annealing. Therefore, the decrease of the junction resistance is attributed to the oxygen vacancies [25].

4.4.2. Spin valve measurement

Figure 4.6(a) shows non-local resistance V/I as a function of the magnetic field for a LSV with injector-detector L of 300 nm. The two distinct non-local resistance corresponds to the parallel and antiparallel magnetization configuration of Py wires. Spin signal ΔR_S is strongly enhanced after the annealing and observed as high as 48.0 mΩ and 112 mΩ at RT and 10 K, respectively.

4.4.3. Interfacial resistance dependence of spin signal

Figure 4.6(b) shows R_I dependence of ΔR_S. ΔR_S increases with an increase in R_I and saturated near R_I = 0.1 Ωμm^2, of which behavior agrees with spin-resistance mismatch model as described in chapter 2, both at RT and 10 K. This is displayed as

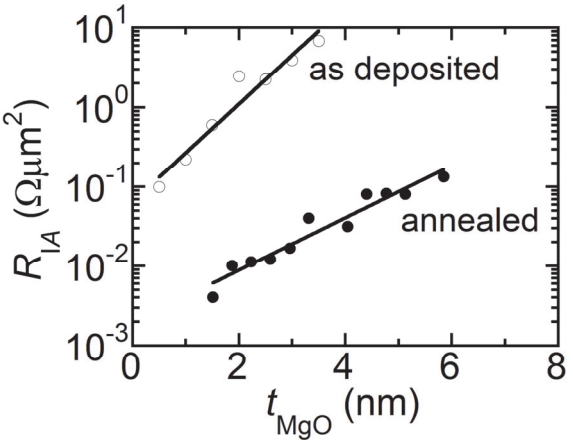

Figure 4.5: Thickness dependence of R_{IA} at RT for annealed and as-deposited samples.

the qualitatively agreed curves in Fig. 4.6(b), which is calculated with Takahashi-Maekawa formula

$$\Delta R_S = \frac{4R_N\left[\frac{P_I^2}{1-P_I^2}\left(\frac{R_I}{R_N}\right)+\frac{P_F}{1-P_F^2}\left(\frac{R_F}{R_N}\right)\right]^2 e^{-L/\lambda_N}}{\left[1+\frac{2}{1-P_I^2}\left(\frac{R_I}{R_N}\right)+\frac{2}{1-P_F^2}\left(\frac{R_F}{R_N}\right)\right]^2 - e^{-2L/\lambda_N}} \tag{4.1}$$

where $R_N = \rho_N\lambda_N/t_N w_N$ and $R_F = \rho_F\lambda_F/w_F w_N$ are the spin-resistance, with resistivity ρ, spin diffusion length λ, thickness t, and width w. The subscripts F and N represent Py and Ag, respectively. λ_{Ag}, P_{Py}, $P_{Py/MgO/Ag}$ are obtained by spin diffusion characteristics (L dependence of ΔR_S) as in sec. 4.4.4.

4.4.4. Separation dependence

Figure 4.7 shows L dependence of ΔR_S for RT and $T = 10$ K. ΔR_S decreases with an increase of L due to the spin flip in Ag. Data were analyzed by using one-dimensional spin diffusion model and fitted to eqn.(4.1), with adjusting parameters of λ_{Ag}, P_{Py}, $P_{Py/MgO/Ag}$. λ_{Py} was set to 5 nm from [24]. We obtained λ_{Ag} = 300 nm, 1100 nm, p_F = 0.30, 0.35, and P_I = 0.42, 0.44 at RT and T = 10 K, respectively. Obtained λ_{Ag} was relatively long and increased by the annealing by a factor of approximately 2 at $T = 10$

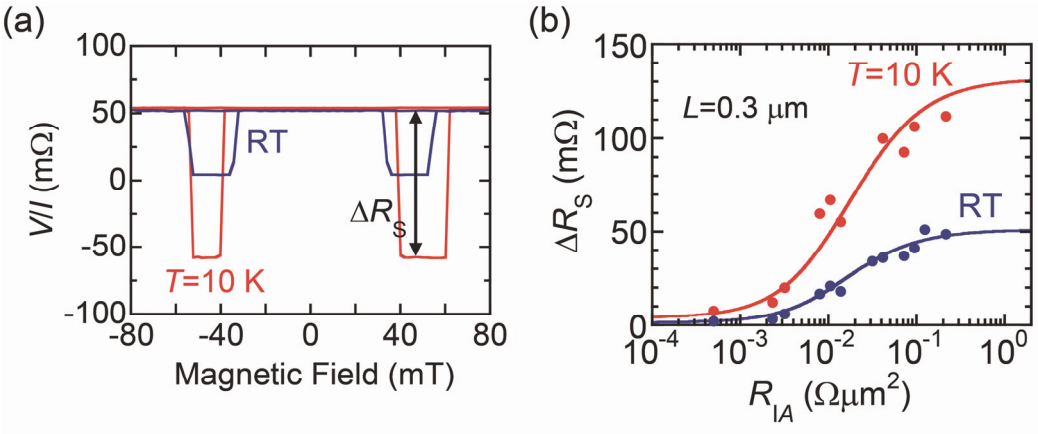

Figure 4.6:(a) Spin signal at RT and $T = 10$ K. (b) R_{IA} dependence of Spin signal ΔR_S for LSV with L = 300 nm. Blue and red dots show the signals for RT and 10 K, respectively. Lines are calculated by using eqn.(4.1).

K and did not change at RT [26, 27]. It is attributed to the decrease of scatterings at grain boundaries because the resistivity of Ag is decreased after annealing. P_{Py} also increases after annealing, which is attributed to the improvement of the crystalline properties. P_I is higher than reported values [8, 10, 26, 28], which explains the obtained high ΔR_S because ΔR_S is proportional to the square of P_I when $R_I >> R_N$.

4.4.5. The effect of interface on the spin injection/detection

The effect of spin injection/detection was analyzed by using one dimensional spin diffusion model described in chapter 2. Spin-resistance of Ag and Py are obtained as 0.9 Ω and 0.07 Ω, respectively, which means higher spin-resistance of Ag prevents efficient spin injection from Py. In the low interface regime with thin MgO layer, R_I is not enough high to overcome spin-resistance mismatch. In the high interface regime, where R_I is higher than 4.5 Ω (R_{IA} is higher than 0.1 Ω μm^2), the spin accumulation was experimentally saturated. Theoretically, the spin polarization of near the interface (spin injection efficiency) was obtained as

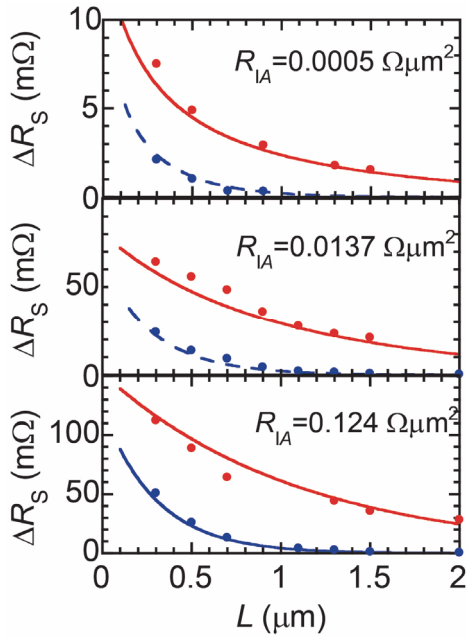

Figure 4.7: Separation dependence of ΔR_S for three different R_{IA}. Blue and red dots show the data for RT and T = 10 K, respectively. Lines are calculated from eqn.(4.1).

$$\frac{j_S}{j} = \frac{\dfrac{2P_I}{1-P_I^2}\dfrac{R_I}{R_N} + \dfrac{2P_F}{1-P_F^2}\dfrac{R_F}{R_N}}{1 + \dfrac{2}{1-P_I^2}\dfrac{R_I}{R_N} + \dfrac{2}{1-P_F^2}\dfrac{R_F}{R_N}}. \tag{4.2}$$

The spin injection efficiency as a function of the normalized interface resistance of NM material is shown in Fig. 4.8(a). It reveals that the efficient spin injection is achieved in the condition of $R_I \sim 5R_N$, and the experimental result is well described by the spin-resistance mismatch model. Figure 4.8(b) shows the spatial distribution of the electro chemical potential near the injector. In contrast to the pronounced back-flow of spin current for low junction resistance, the Py/MgO/Ag junctions for $R_I \sim 5R_N$ completely suppresses the back-flow and enable to efficiently generate spin current in NM. Figure 4.8(c) shows the spin absorption effect due to the detector electrode. Spin absorption effect was decreased by inserting interface layer in which junction resistance is comparable to the spin-resistance of NM material. Therefore, the decrease of the spin accumulation due to the spin absorption is suppressed and enables to detect spin accumulation without loss. This means the efficient detection of the spin accumulation.

4.4.6. Bias current dependence

Now, the maximum spin accumulation was examined with changing bias current. Figure 4.9 shows the bias current dependence of $\Delta V_S = I\Delta R_S$ for various

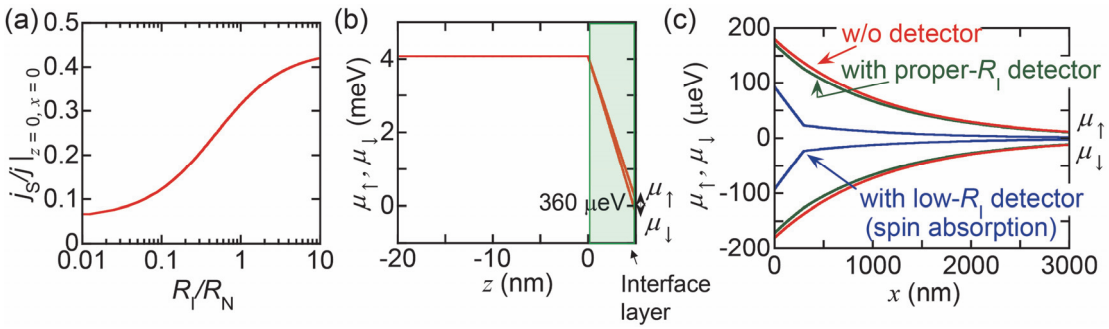

Figure 4.8: (a) R_I dependence of spin injection efficiency. (b) Spatial distribution of the electro chemical potential in FM and interface layer for $R_I = 4.5R_N$ (c) Spatial distribution of the electro chemical potential in NM for LSVs with and without detector for $L = 300$ nm, $R_I = 4.5R_N$ and $I = 1$ mA.

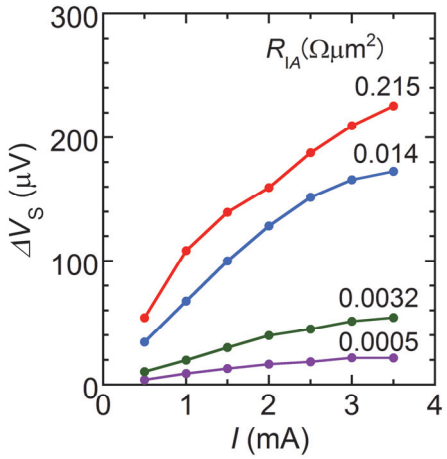

Figure 4.9: Bias current dependence of spin accumulation signal $\Delta V_S = I\Delta R_S$ at $T = 10$ K for four different interface resistance.

junctions at $T = 10$ K. ΔV_S monotonically increases with an increase of I. ΔV_S takes a maximum 225 μV when $I = 3.5$ mA before the device becomes broken at $I = 4.0$ mA.

4.5 Structural issue

4.5.1 Enhancement of spin accumulation in dual injector LSV with Py/MgO/Ag junctions

A conventional LSV consists of a pair of injector and detector FM wires which are bridged by a NM wire. The spins are injected by applying a bias voltage across the FM/NM interface and accumulate in its vicinity. Their density decays exponentially with a factor of $\exp(-d/\lambda_{sf})$ where d is the distance from the injector and λ_{sf} is the spin diffusion length. Unlike the above LSV, our structure shown in Fig. 4.10(a) consists of three Py wires bridged by a Ag wire. I is applied between FM1 and FM2 for the spin injection into the Ag wire, and the spin accumulation is detected in voltage V by using FM3. To avoid the spin absorption by FM wires, we use the Py/MgO/Ag junction in the present study [26, 29]. For comparison between conventional and our schemes, we depict the spatial variation of spin accumulation $\delta\mu_{Ag}$ in the Ag wire calculated by using the same material parameters in Figs. 4.10(b)-(d). In a conventional scheme of Fig.

4.10(b), the spin injection generates the spin current I_S towards both directions along the Ag wire, the magnitude of which is proportional to the spatial gradient of $\delta\mu_{Ag}$. On the other hand, our scheme shown in Figs. 4.10(c) and (d), confines the spin current solely to the detector since the unnecessary side edge, i.e., relaxation volume, on the left of FM1 is removed. Figure 4.10(c) shows $\delta\mu_{Ag}$ from each injector with parallel magnetization configuration and the magnitude of each spin current from FM1 and FM2 can be twice as much as the conventional I_S due to the confinement effect. As the direction of spin current across the FM1/MgO/Ag and FM2/MgO/Ag interfaces is opposite each other, the currents flowing across the interfaces thus cancel out for the parallel magnetic configuration of dual injectors, whereas for the antiparallel configuration, the spin currents induced by FM1 and FM2 are constructive as depicted in Fig. 4.10(d). As a result, this scheme can enhance the total spin current by up to a factor of four compared to the conventional one.

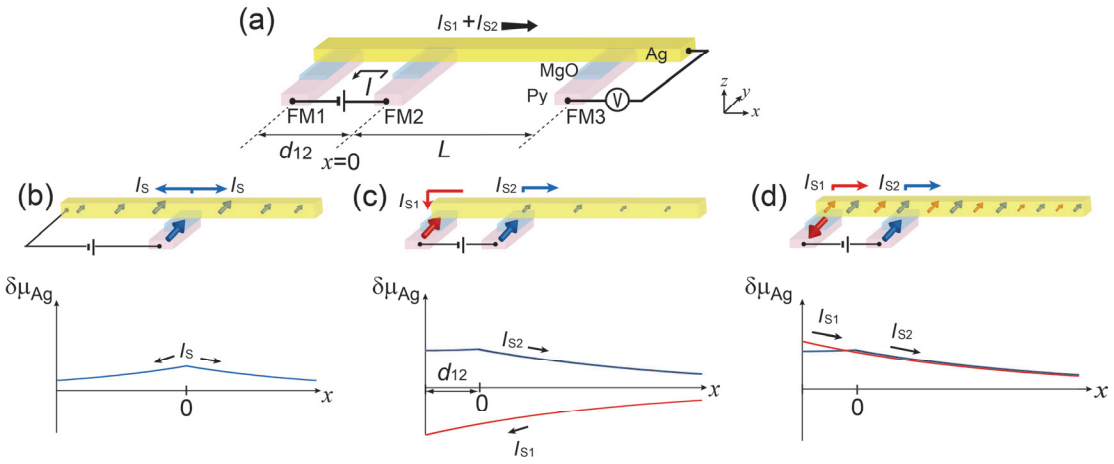

Figure 4.10: (a) Schematic diagram of lateral spin valve with dual injectors in non-local measurement configuration. (b) Schematic diagram of LSV with single injector and the spatial variation of spin accumulation $\delta\mu$ for Ag. Arrows in Ag and FM, respectively represent the non-equilibrium magnetization of Ag and the magnetization of FM. The spin current $I_S = I\uparrow - I\downarrow$ flows in both directions along the Ag wire. The magnitude of I_S is proportional to the spatial gradient of $\delta\mu$. (c),(d) Schematic diagram of LSV with dual injectors with parallel or antiparallel configuration and the spatial variation of spin accumulation $\delta\mu$ for Ag. The red and blue lines show $\delta\mu_{Ag}$ induced by spin injectors of FM1 and FM2, respectively. In parallel configuration, the flow direction of spin current from FM2 I_{S2} is opposite to that of FM1 I_{S1}. In antiparallel configuration, the flow direction of I_{S1} is the same as that of I_{S2}.

LSV with Py/MgO/Ag junctions were used in this study. The Py wires were 140 nm in width and 20 nm in thickness. The Ag wire was 120 nm in width and 100 nm in thickness. Center-to-center separation between FM1 and FM2 d_{12} was 350 nm. The non-local spin valve signal in LSVs is shown in Figs. 4.11(a)-(b). For the conventional single injector LSV (SLSV), the high and low signals correspond, respectively to the parallel and antiparallel configurations of the injector and detector FMs, of which overall change ΔR_S amounts to 31.5 mΩ at 10 K in Fig. 4.11(a). Figure 4.11(b) shows the spin signal for the dual injector LSV (DLSV). All FMs exhibit distinct switching fields at around 10 mT, 40 mT and 50 mT, corresponding to the switching fields of FM1, FM2 and FM3, respectively. The hysteresis loop shows three-level signals associated with the following magnetic configurations; in the negative sweep (green line), the magnetization of FM1 flips at -10 mT and the injectors' magnetization configuration becomes antiparallel. Accordingly FM3 detects the change in the electro chemical potential and the resulting change in $\delta\mu_{Ag}$ is shown in Fig. 4.11(c). Further decrease in field down to -40 mT flips the magnetization of FM2 and returns the injectors' magnetic configuration to parallel. Since the antiparallel configuration maximizes the spin accumulation in DLSV, it can be evaluated from the overall change ΔR_S between the minor loop shown in a red curve and the positive sweep shown in a blue line in Fig. 4.11(b). The center-to-center injector and detector L dependence of ΔR_S in Fig. 4.11(c) shows that ΔR_S of DLSV is almost 3 times larger than that of SLSV and decreases exponentially with increasing L due to spin relaxation in the Ag wire [30, 31].

The analytical expression of ΔR_S for DLSV, for the case where the interface resistance is enough higher than the spin-resistance of the NM wire R_N, is approximated by using a solution of one-dimensional spin diffusion equation (see Chapter 2 for details)

$$\Delta R_S = \alpha P_I^2 R_N e^{-L/\lambda_N}, \tag{4.3}$$

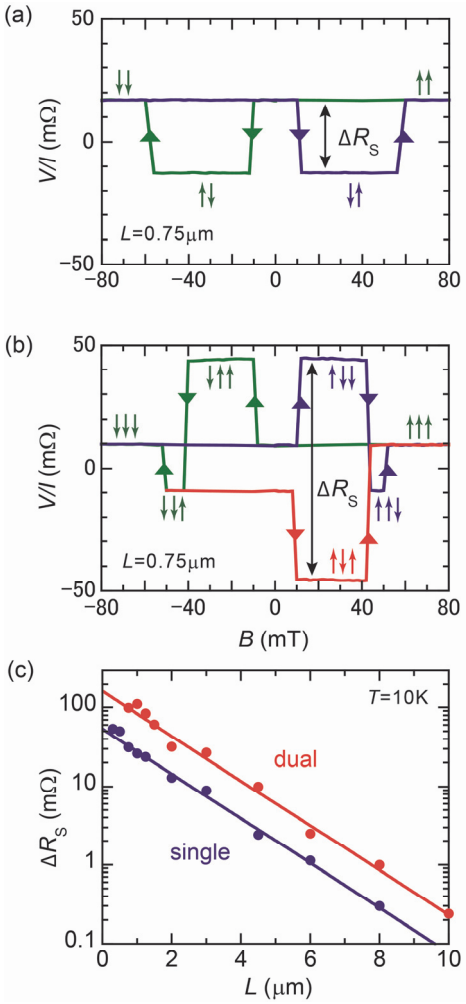

Figure 4.11: (a) Spin valve signal as a function of *y*-directional magnetic field for SLSV at 10 K. The arrows indicate the magnetization configuration of two Py wires. The triangles indicate the sweep direction of the magnetic field. (b) Spin valve signal as a function of magnetic field for DLSV at 10 K. The arrows indicate the magnetization configuration of three Py wires. The triangles indicate the sweep direction of the magnetic field. The red line shows the minor hysteresis loop. (c) Spin signal ΔR_S as a function of injector-detector separation at T = 10 K. The solid lines are the fitting curves using eqn.(4.3).

where $\alpha = 1 + \exp(-2d_{12} / \lambda_N) + 2\exp(-d_{12} / \lambda_N)$, P_I is interfacial polarization, λ_N is the spin diffusion length of the NM and d_{12} is the separation between FM1 and FM2. The ΔR_S for DLSV is remarkably enhanced by a factor of α compared to that of SLSV, corresponding to the reduced eqn.(4.3) of ΔR_S for SLSV [32] with $d_{12} >> \lambda_N$ (see sec. 2.1.10). The first and second terms in α represent the spin current injected from FM2 and the third term does the spin current injected from FM1. The obtained experimental

results in Fig. 4.11(c) were fitted to eqn.(4.3) with adjusting parameters P_I and λ_N, yielding $P_I = 0.36$, $\lambda_N = 1500$ nm and $\alpha = 3.2$, which are consistent with our previous data for Py/MgO/Ag junctions [29]. The longer λ_N is attributed to the suppression of the electron scattering in thicker Ag nanowire, which is consistent with the decrease of the resistivity. The quantitative discussion based on the spin relaxation mechanism will be provided in sec. 5.3.4 (50-nm-thick-Ag) and in sec. 6.2.3 (100-nm-thick-Ag).

4.5.2 Effect of spin absorption in dual injector LSV

In the previous section, we have studied dual injector LSV with FM/MgO/Ag junctions, which prevents spin absorption effect. For the solid understandings of the multi-terminal spin injection scheme, this section will discuss the impact of the spin absorption effect in dual injector LSV with Py/Ag junctions.

The non-local spin injection measurements were performed on the LSVs by using conventional current-bias lock-in technique with applied current of 0.15 mA and frequency of 79 Hz. The scanning electron microscopy images of fabricated LSVs were shown in Figs.4.12 (b) and (c). The field dependence of the spin valve signal for DLSV with Ohmic Py/Ag junction (Ohmic-DLSV) with $L = 500$ nm is shown in Fig. 4.12 (d). In the full hysteresis loop, the six leaps of non-local resistance are clearly observed corresponding to the magnetization reversals of three FM wires. The magnetic configurations are indicated by arrows in Fig. 4.12 (d). Since the current direction is opposite each other for the Py1/Ag junction and the Py2/Ag junction, spin accumulation in the Ag wire is maximized when the magnetization configuration of Py1 and Py2 is antiparallel. The spin valve signal ΔR_S is defined as the overall change of the non-local resistance, which is observed to be 11.5 mΩ. The contribution of each injector Py1 and Py2 to ΔR_S is estimated to be $\Delta R_{F1} = 1.8$ mΩ and $\Delta R_{F2} = 9.7$ mΩ, respectively, as depicted in Fig. 4.12 (d). The low value of $\Delta R_{F1}/\Delta R_{F2} = 0.19$ suggests that Py1 is not efficiently working to enhance the spin accumulation at the detector. On the other hand,

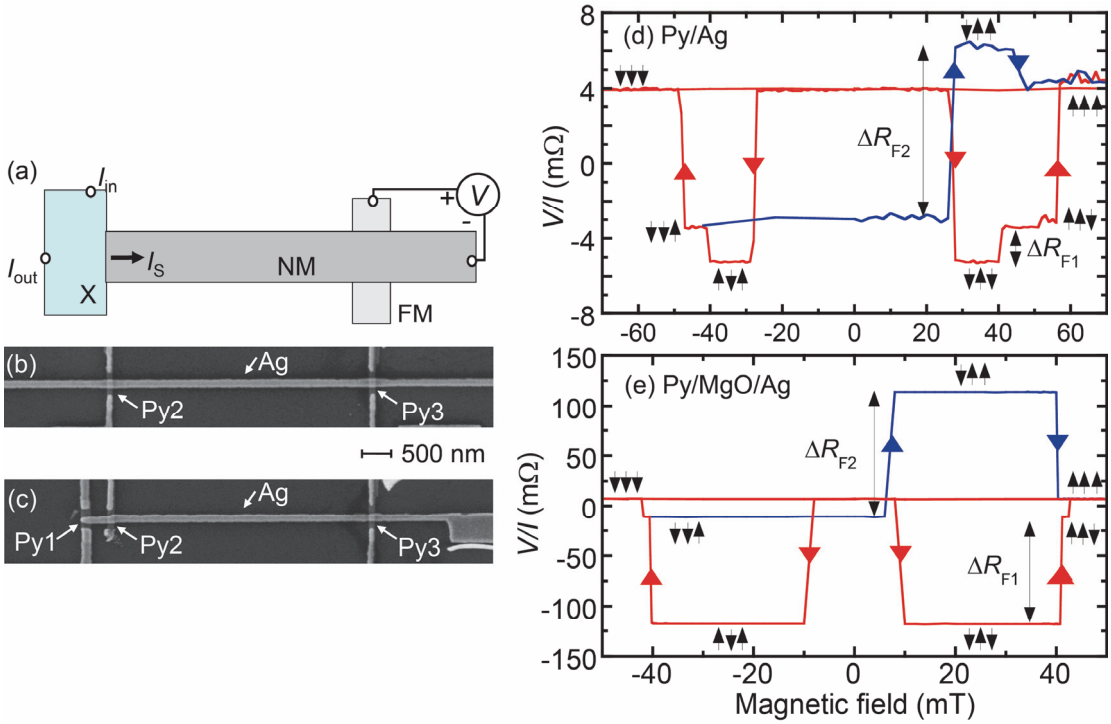

Figure 4.12: (a) Schematic diagram of the measurement configuration of non-local spin injection. (b) Scanning microscope image of conventional single injector lateral spin valve (SLSV). (c) That of dual injector lateral spin valve (DLSV). (d) Non-local spin signal as a function of magnetic field for LSV with Py(20nm)/Ag(50nm) Ohmic junctions at 10 K. Arrows display corresponding magnetic states of Py1, Py2 and Py3, from left to right. ΔR_{F1} and ΔR_{F2} show the change of non-local resistance due to the magnetization reversals of Py1 and Py2, respectively. (e) Non-local spin signal as a function of magnetic field for LSV with Py(20nm)/MgO(6.4nm)/Ag(50nm) junctions.

ΔR_S of DLSV with Py/MgO/Ag junctions (Py/MgO-DLSV) with L = 500 nm is as large as 233 mΩ, as shown in Fig. 4.12 (e). The contribution of the each injector to the signal is estimated to be ΔR_{F1} = 104 mΩ, ΔR_{F2} = 129 mΩ and $\Delta R_{F1}/\Delta R_{F2}$ = 0.806, implying that the both Py1 and Py2 injectors work equivalently in Py/MgO-DLSVs.

Figure 4.13 shows ΔR_S as a function of L for the DLSVs. ΔR_S decreases reasonably with increasing L due to the spin relaxation in the Ag nanowire. Clear enhancement of ΔR_S is observed for Py/MgO-DLSVs, while ΔR_S of Ohmic-DLSVs is slightly enhanced compared to that of Ohmic-SLSVs. To gain the insight of the difference of ΔR_S for the junctions, we perform the fitting of ΔR_S, based on the one

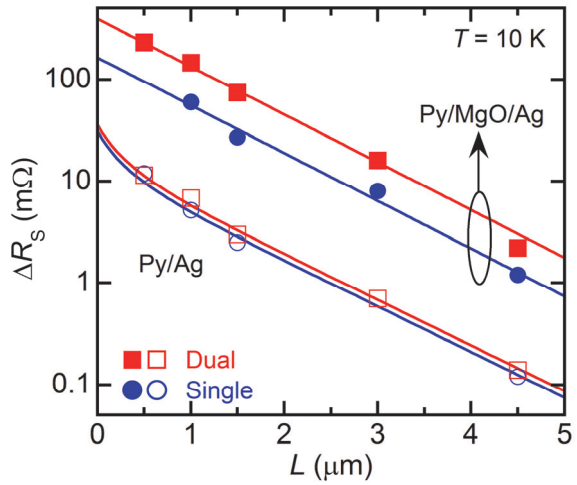

Figure 4.13: Spin valve signal $\Delta R_S \equiv \Delta R_{F1} + \Delta R_{F2}$ as a function of injector-detector separation L at 10 K for DLSVs and SLSVs with Py/MgO/Ag junctions and Py/Ag junctions. Closed squares, closed circles, open squares and open circles show DLSVs with Py/MgO/Ag junctions, SLSVs with Py/MgO/Ag junctions, DLSVs with Py/Ag junctions and SLSVs with Py/Ag junctions, respectively. Blue solid lines are the fitting curves using eqn.(4.5) for SLSVs with Py/MgO/Ag junctions and Py/Ag junctions. Red solid lines show the curves for DLSVs with Py/MgO/Ag junctions and Py/Ag junctions.

dimensional spin-diffusion equation [32, 33]. One obtains equations of ΔR_S for DLSVs and SLSVs, respectively, as below

$$\Delta R_{S\_DLSV} = R_N (P_{F3} r_{F3} + P_{I3} r_{I3}) e^{-L/\lambda_N} \times$$

$$\frac{(2 + r_{I1} + r_{F1})(P_{I2} r_{I2} + P_{F2} r_{F2}) + 2e^{-d_{I2}/\lambda_N}(r_{I2} + r_{F2})(P_{I1} r_{I1} + P_{F1} r_{F1}) + e^{-2d_{I2}/\lambda_N}(-2 + r_{I1} + r_{F1})(P_{I2} r_{I2} + P_{F2} r_{F2})}{(2 + r_{I1} + r_{F1})\left[(1 + r_{I2} + r_{F2})(1 + r_{I3} + r_{F3}) - e^{-2L/\lambda_N}\right] + e^{-2d_{I2}/\lambda_N}(-2 + r_{I1} + r_{F1})\left[e^{-2L/\lambda_N}(-1 + r_{I2} + r_{F2}) + (1 + r_{I3} + r_{F3})\right]},$$

(4.4)

$$\Delta R_{S\_SLSV} = R_N e^{-L/\lambda_N} \times \frac{(P_{F2} r_{F2} + P_{I2} r_{I2})(P_{F3} r_{F3} + P_{I3} r_{I3})}{(1 + r_{I2} + r_{F2})(1 + r_{I3} + r_{F3}) - e^{-2L/\lambda_N}}, \quad (4.5)$$

where $r_{Fj} = [2/(1 - P_{Fj}^2)]R_{Fj}/R_N$ and $r_{Ij} = [2/(1 - P_{Ij}^2)]R_{Ij}/R_N$ are the normalized spin-resistance of FM and the normalized interface resistance, respectively, P_{Fj} and P_{Ij} are the spin polarization of j_{th} FM and interface, respectively, $R_N = \rho_N \lambda_N / A_N$ and $R_F = \rho_F \lambda_F / A_J$ are the spin-resistance of NM and FM, respectively, R_{Ij} is the j_{th} junction resistance, ρ is the resistivity, and A_J is the junction resistance.

For the Py/MgO/Ag junctions, the interfacial resistance-area product $R_{Ij}A_J = 0.1$ $\Omega(\mu m)^2$ is much larger than $R_{Ag}A_N \approx 8.0 \times 10^{-3}$ $\Omega(\mu m)^2$ where A_N is the cross-sectional area of non-magnet, implying that the spin absorption from Ag to Py is mostly suppressed. The experimental data are well fitted by the one dimensional model with the fitting parameters of $P_I = 0.37$ and $\lambda_{Ag} = 930$ nm, as can be seen in Fig. 4.13. The widths of the Py1, Py2, Py3 and Ag wires were 140 nm, 100 nm, 100 nm and 100 nm, respectively. The separation d_{12} between Py1 and Py2 was 350 nm. The resistivity of Ag was 0.86×10^{-6} Ωcm. The enhancement factor of the spin accumulation in DLSVs compared to that in SLSVs is estimated to be $\alpha \equiv \Delta R_{S\_DLSV} / \Delta R_{S\_SLSV} = 2.4$. The analytical expression of α in the interfacial spin polarization dominate regime, i.e., $R_I >> R_N$ is obtained as

$$\alpha = 1 + 2\exp(-d_{12}/\lambda_N) + \exp(-2d_{12}/\lambda_N) = (1 + \Delta R_{F1}/\Delta R_{F2})\{1+\exp(-2d_{12}/\lambda_N)\}, \quad (4.6)$$

from eqns.(4.4) and (4.5), where d_{12} is the separation between FM1 and FM2. For the Py/Ag junctions, the interface parameters of P_{Ij} and R_{Ij} are neglected. The experimental data are well fitted by adjusting parameters P_{Py} and λ_{Ag} with setting the value of $\lambda_{Py} = 5$ nm reported by Dubois *et al.* [24]. We obtain $P_{Py} = 0.37$ and $\lambda_{Ag} = 970$ nm, leading to $\alpha = 1.2$. The analytical model supports the little enhancement of ΔR_S in Ohmic-DLSV.

In order to discuss the origin of the different α in DLSVs, the spin absorption process could be examined in more details following the model that led to eqns.(4.4)-(4.5). First, we consider the spin current injected from Py1/Ag junction. The contribution to ΔR_S, namely, ΔR_{F1} is characterized as a function of an interface parameter $x_2 \equiv r_{F2}+r_{I2}$ which determines the magnitude of spin absorption into Py2. From eqn.(4.4) one can obtain $\Delta R_{F1} \propto x_2/(\beta x_2 + \gamma)$, where β and γ are x_2-independent coefficients derived from eqn.(4.4). As a result, ΔR_{F1} increases with x_2 because of the suppression of the spin absorption effect. ΔR_{F1} of Ohmic-DLSV is quantitatively

evaluated to be 2.1 mΩ from eqn.(4.4) with the fitting parameters mentioned above, which is in good agreement with the experimental value shown in Fig. 4.12(d). Second, we analyze the spin current injected from a Py2/Ag junction in the same manner. From eqn.(4.4) one can obtain $\Delta R_{F2} \propto (x_1 + \delta)/(\varepsilon x_1 + \phi)$ where δ, ε and ϕ are x_1-independent coefficients derived from eqn.(4.4) and $x_1 \equiv r_{F1}+r_{I1}$ determines the spin absorption into Py1. ΔR_{F2} of Ohmic-DLSV is 8.6 mΩ which is much larger than that of ΔR_{F1}, implying that the spin accumulation is less influenced by the spin absorption effect of Py1 compared to that of Py2. This is due to the difference of the travelling path of the injected spin current: spins injected from Py2 diffuse toward Py1 and Py3 and some spins can pass through the Ag wire on the Py1/Ag interface to reach the detector whereas all the spins injected from Py1 must pass through the Ag wire on the Py2/Ag interface to reach the detector.

4.5.3 Enhancement of spin accumulation in dual injector LSV with $Co_{50}Fe_{50}$/MgO/Ag junctions

The interface MgO layer is critical to enhance the spin accumulation in DLSV as well as SLSV. The FM layer of Py is so far used in our studies [29, 33-35], however, higher spin polarization is expected for CoFe and CoFeB [22, 36-38]. Therefore, we fabricated LSVs with $Co_{50}Fe_{50}$/MgO/Ag(50nm) and measured Hale effect signal for the SLSV, as shown in Fig. 4.14(a). The analytical expression of ΔR_S is expressed as [29]

$$\Delta R_S = P_I^2 R_N \,\mathrm{Re}\left[\frac{\lambda_\omega}{\lambda_{sf}}\exp\left(-\frac{L}{\lambda_\omega}\right)\right] \tag{4.7}$$

with $\lambda_\omega = \dfrac{\lambda_{sf}}{\sqrt{1+i\omega_L\tau_{sf}}}$

where $\omega_L = g\mu_B B_Z/\hbar$ is Larmor frequency with g the g-factor, μ_B Bohr magneton and τ_{sf} is spin relaxation time, respectively. P_I = 0.52 and λ_{Ag} =780 nm are obtained by

fitting eqn.(4.7) to the experimental data of L = 4.5 μm as shown in Fig. 4.14 (a). Diffusion constant of Ag were 0.056 m^2/s. The obtained P_I of CoFe is higher than that of Py. Figure 4.14 (b) shows the spin valve signal for DLSV with CoFe/MgO/Ag. Large ΔR_S of 220 mΩ and 480 mΩ is observed at 300 K and 10 K, respectively, whereas for SLSV, ΔR_S was 135 mΩ and 230 mΩ. We shall note that a relation is not trivial between the enhancement of detected spin accumulation and that of efficiency for the generation of the pure spin current I_S/I_C. However, the one-dimensional spin diffusion model reveals the same enhancement factor α between them for LSVs with FM/MgO/Ag. The α is enhanced up to 4 in the small d_{12}/λ_N limit, suggesting that the obtained $I_S/I_C = \alpha P_I/2$ = 0.58 (P_I = 0.36 and α =3.2 for Py/MgO/Ag(100nm)), $I_S/I_C = \alpha P_I/2$ = 0.44 (P_I = 0.37 and α =2.4 for Py/MgO/Ag(50nm)) and 0.55 (P_I = 0.52 and α =2.1 for

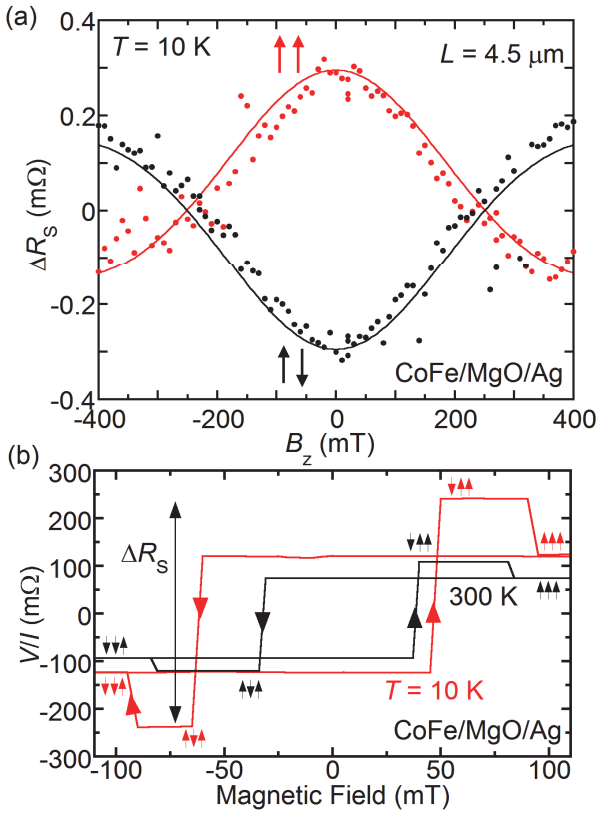

Figure 4.14: (a) Hanle effect of SLSV with CoFe(14nm)/MgO(7.0nm)/Ag(50nm) junctions. Black and red show Hanle signal when the measurements start from parallel and antiparallel magnetic configurations of injector and detector, respectively. (b) Non-local spin signal as a function of magnetic field for DLSV with CoFe/MgO/Ag junctions with L = 300 nm.

CoFe/MgO/Ag(50nm)) can be further improved by optimizing λ_N and d_{12}. This could be useful for developing variety of spintronic devices using pure spin current and spin accumulation.

4.6 Conclusion for chapter 4

Sections 4.2-4.4 describes the enhancement of the spin accumulation in LSVs with Py/Ag junctions and Py/MgO/Ag junctions. The effect of the junction is systematically studied with different MgO thickness for Py/MgO/Ag junctions. The spin signal increases with an increase of the MgO thickness, in which behavior is understood by a spin-resistance mismatch. The result of the annealed sample is analyzed in detail with the spin diffusion model, which gives the spin diffusion length of Ag, the spin polarization of the interface, and the spin polarization of Py. It reveals that the origin of the enhancement of the spin accumulation as follows. (1) The injector Py/MgO/Ag junction prevents back-flow of spin current, which enables efficient spin injection. (2) The detector Py/MgO/Ag junction prevents the decrease of the spin accumulation due to the spin absorption, which enables "efficient" detection of the spin accumulation. Since the desired interface resistance is around the spin-resistance of Ag, the Py/MgO/Ag junctions enables to apply higher current than one for the conventional high resistance magnetic tunnel junctions. It results in the hundred-fold spin accumulation signal $\Delta V = 225$ μV for LSVs.

In sec 4.5, we have investigated the enhancement of spin accumulation in dual-injection lateral spin valves (DLSVs). The spin accumulation is enhanced by a factor α for the dual spin injection scheme compared with the conventional single spin injection scheme. α reaches 3.2 for the Py/MgO/Ag(100nm) junctions. Spin accumulation shows a maximum when the injectors takes antiparallel magnetic configurations. Although the number of injection electrodes is increased in a lateral

geometry, the spin absorption effect for Ohmic Py/Ag junctions prevents the enhancement of the spin accumulation in the Ag nanowire. α is 2.4 and 1.2 for the Py/MgO/Ag(50nm) junctions and Py/Ag(50nm) junctions, respectively. Analysis based on one-dimensional spin diffusion model revealed that the spin absorption effect in the middle Py/Ag junction strongly suppress the enhancement of the spin accumulation in Ohmic-DLSVs. We found α reaches up to 4 in the present device structure with small d_{12}/λ_N and without spin absorption. Large spin vale signals of 233 mΩ and 480 mΩ are observed for DLSVs with Py/MgO/Ag and $Co_{50}Fe_{50}$/MgO/Ag, respectively. The junction polarization of $Co_{50}Fe_{50}$/MgO/Ag is as high as 0.52. The efficient generation of the pure spin current $I_S/I_C = 0.58$ is realized.

References for chapter 4

[1] M. Johnson and R. H. Silsbee, *Physical Review B* **35**, 4959 (1987).

[2] P. C. van Son, H. van Kempen, and P. Wyder, *Physical Review Letters* **58**, 2271 (1987).

[3] T. Kimura, Y. Otani, and J. Hamrle, *Physical Review Letters* **96**, 037201 (2006).

[4] T. Yang, T. Kimura, and Y. Otani, *Nature Physics* **4**, 851 (2008).

[5] J. Z. Sun *et al.*, *Applied Physics Letters* **95**, 083506 (2009).

[6] D. Ilgaz *et al.*, *Physical Review Letters* **105**, 076601 (2010).

[7] F. Jedema, A. T. Filip, and B. J. van Wees, *Nature* **410**, 345 (2001).

[8] F. Jedema, H. Heersche, A. T. Filip, J. Baselmans, and B. J. van Wees, *Nature* **416**, 713 (2002).

[9] S. Garzon, I. Žutić, and R. Webb, *Physical Review Letters* **94**, 176601 (2005).

[10] S. Valenzuela, D. Monsma, C. Marcus, V. Narayanamurti, and M. Tinkham, *Physical Review Letters* **94**, 196601 (2005).

[11] R. Godfrey and M. Johnson, *Physical Review Letters* **96**, 136601 (2006).

[12] T. Kimura and Y. Otani, *Physical Review Letters* **99**, 196604 (2007).

[13] A. Vogel, J. Wulfhorst, and G. Meier, *Applied Physics Letters* **94**, 122510 (2009).

[14] X. J. Wang, H. Zou, L. E. Ocola, and Y. Ji, *Applied Physics Letters* **95**, 022519 (2009).

[15] M. Johnson and R. H. Silsbee, *Physical Review Letters* **55**, 1790 (1985).

[16] F. Jedema, M. Nijboer, A. T. Filip, and B. J. van Wees, *Physical Review B* **67**, 085319 (2003).

[17] M. Johnson and R. H. Silsbee, *Physical Review B* **37**, 5312 (1988).

[18] A. Fert and S.-F. Lee, *Physical Review B* **53**, 6554 (1996).

[19] M. Zaffalon and B. J. van Wees, *Physical Review Letters* **91**, 186601 (2003).

[20] H. Jaffrès, J. M. George, and A. Fert, *Physical Review B* **82**, 140408(R) (2010).

[21] J. Bass and W. P. Pratt, *Journal of Physics: Condensed Matter* **19**, 183201 (2007).

[22] S. S. P. Parkin, C. Kaiser, A. Panchula, P. M. Rice, B. Hughes, M. Samant, and S. H. Yang, *Nature Materials* **3**, 862 (2004).

[23] S. Yuasa, T. Nagahama, A. Fukushima, Y. Suzuki, and K. Ando, *Nat Mater* **3**, 868 (2004).

[24] S. Dubois, L. Piraux, J. M. George, K. Ounadjela, J. L. Duvail, and A. Fert, *Physical Review B* **60**, 477 (1999).

[25] W. Wulfhekel, M. Klaua, D. Ullmann, F. Zavaliche, J. Kirschner, R. Urban, T. Monchesky, and B. Heinrich, *Applied Physics Letters* **78**, 509 (2001).

[26] Y. Fukuma, L. Wang, H. Idzuchi, and Y. Otani, *Applied Physics Letters* **97**, 012507 (2010).

[27] H. Idzuchi, Y. Fukuma, L. Wang, and Y. Otani, *Applied Physics Express* **3**, 063002 (2010).
[28] S. O. Valenzuela and M. Tinkham, *Nature* **442**, 176 (2006).
[29] Y. Fukuma, L. Wang, H. Idzuchi, S. Takahashi, S. Maekawa, and Y. Otani, *Nat Mater* **10**, 527 (2011).
[30] R. J. Elliott, *Physical Review* **96**, 266 (1954).
[31] Y. Yafet, *Solid State Physics* **14**, 1 (1963).
[32] S. Takahashi and S. Maekawa, *Physical Review B* **67**, 052409 (2003).
[33] H. Idzuchi, Y. Fukuma, and Y. Otani, *Scientific reports* **2**, 628 (2012).
[34] L. Wang, Y. Fukuma, H. Idzuchi, G. Yu, Y. Jiang, and Y. Otani, *Applied Physics Express* **4**, 093004 (2011).
[35] H. Idzuchi, Y. Fukuma, L. Wang, and Y. Otani, *Applied Physics Letters* **101**, 022415 (2012).
[36] S. Yuasa, T. Katayama, T. Nagahama, A. Fukushima, H. Kubota, Y. Suzuki, and K. Ando, *Applied Physics Letters* **87**, 222508 (2005).
[37] D. D. Djayaprawira, K. Tsunekawa, M. Nagai, H. Maehara, S. Yamagata, N. Watanabe, S. Yuasa, Y. Suzuki, and K. Ando, *Applied Physics Letters* **86**, 092502 (2005).
[38] C. Ahn, K.-H. Shin, R. Loloee, J. Bass, and W. Pratt, *Journal of Applied Physics* **108**, 023908 (2010).

Chapter 5

Spin relaxation mechanism in non-magnetic nanowires

5.1 Introduction

The spin relaxation mechanism in non-magnetic (NM) metals has originally been discussed by Elliott and Yafet [1, 2]. According to their theory, the spin-orbit interaction (SOI) in NM lifts the spin degeneracy of Bloch electrons, and results in two different energy states for up or down spin. The spin relaxation, i.e., the transition between the opposite spin states, can therefore be caused by the spin independent momentum scatterings due to impurities, grain boundaries, surfaces and phonons [1-3]. The earlier experimental works on the spin relaxation mechanism were mainly performed by conduction electron spin resonance (CESR) measurements and the results were *e.g.*, analyzed by Monod and Benue in the material independent manner [4, 5]. Fabian and Das Sarma revisited the CESR analyses and showed a quantitative relationship between the spin-flip scattering and the phonon mediated change in resistivity including the effect of Fermi surface topology [6, 7]. Since the emergent development in the spintronic devices requires understanding the spin relaxation mechanism in nanowires, the mechanism has been intensively studied by means of non-local spin injection techniques using LSVs as a unique probe [8-12]. However, since the spin transport properties of LSV depends on the qualities of the sample, it is desired to separate the intrinsic and extrinsic properties. In this section we studied it by analyzing temperature dependence of the spin relaxation properties. Sec. 5.3 provides detail analysis of spin relaxation mechanism in Ag nanowire. Surface spin relaxation is recently reported in the NM nanowires, which hampered a quantitative analysis of the

spin relaxation mechanism [10-12]. The surface spin scattering is now suppressed by MgO protection layer and then the spin-flip probability ε for phonon or impurity scattering is determined accurately on the basis of Elliott-Yafet (E-Y) mechanism. The temperature dependence of the spin-lattice relaxation for the phonon scattering is well fitted to the Bloch-Grüneisen formula [13, 14], showing good consistency with that obtained from CESR measurements in the bulk.

In the latter section, we study the effect of the topology on the spin relaxation properties with the spin injection into light metal Mg, having a weak SOI, and thus being a promising candidate for materials with longer spin diffusion length. To our knowledge, there is no report on the spin injection into Mg from the ferromagnetic metal whereas the spin diffusion length of Al is reported in the order of micrometer at low temperatures [9].

5.2 Spin injection into Mg

5.2.1 Fabrication of Mg-based LSV

LSV devices were fabricated by means of shadow evaporation combined with *e*-beam lithography using a suspended resist mask, consisting of a bilayer resist 500-nm-thick Methyl methacrylate (MMA) and 50-nm-thick Poly methyl methacrylate (PMMA) formed on Si/SiO_2 substrates. Firstly a Py layer was *e*-beam deposited at an angle of 45 degrees from substrate normal. Then, the substrate was transferred under vacuum to the different chamber with a base pressure 6×10^{-8} Pa, and a Mg layer was *e*-beam deposited normal to the substrate cooled by liquid nitrogen. Finally, a 5-nm-thick MgO capping layer was deposited to protect the surface. After a lift-off procedure, the structure was examined by means of scanning electron microscopy (SEM), as shown in Fig. 5.1. Three classes of devices, LSV1, 2, and 3, with different Py and Mg wire widths w_{Py} and w_{Mg} were prepared. For LSV1, a Py wire with w_{Py} of 80 nm was bridged by a Mg wire with w_{Mg} of 110 nm. For LSV2 and 3, w_{py} were different, 80 nm for LSV2 and

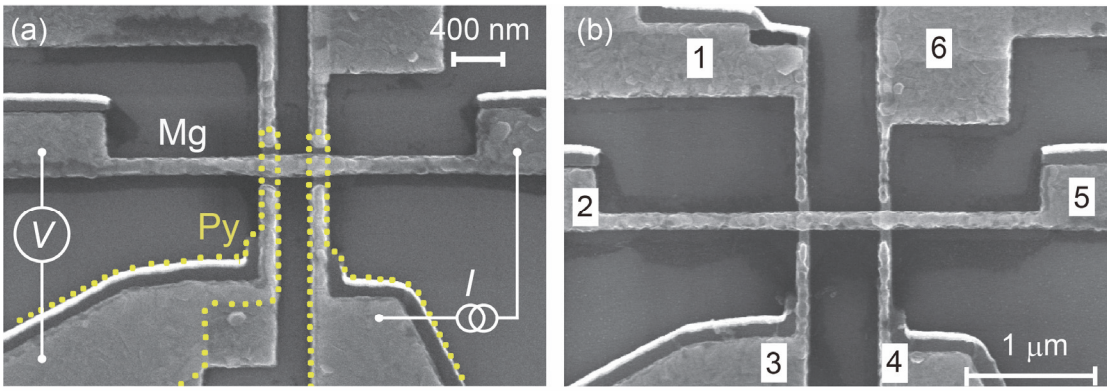

Figure 5.1: Scanning electron microscope (SEM) images of fabricated lateral spin valve devices with measurement circuit of non-local resistance.

130 nm for LSV3 while w_{Mg} was set at 170 nm. The thicknesses of all the Py and Mg layers were 20 nm and 100 nm, respectively. The center-to-center separation L between the Py injector and detector was varied from 250 nm to 1000 nm to determine the spin diffusion length λ_{Mg} of Mg. After examination of SEM, all the devices were covered with a 10-nm-thick sputter deposited SiO_2 layer to prevent oxidation of the side edges of Mg wires.

5.2.2 Non-local and local spin valve measurement

The spin injection from Py into Mg is carried out by non-local technique, where the current is applied between terminals 4 and 5 and the voltage is detected by using terminals 2 and 3, as shown in Fig. 5.1(b). The non-local spin valve measurements are performed by using conventional current-bias lock-in technique with amplitude of 0.20 mA with a frequency of 79 Hz. The magnetic field is applied parallel to the Py wires. The field dependence of the non-local resistance for the LSV with L = 300 nm is shown in Fig. 5.2(a), representing a clear spin valve behavior. The switching field of each Py wire is controlled by the domain-wall nucleation, i.e., the injector has a large domain wall reservoir at the edge, producing lower switching field than the detector. Spin valve signal $\Delta R_S = (V_P - V_{AP})/I$, is defined as the overall signal change between parallel and

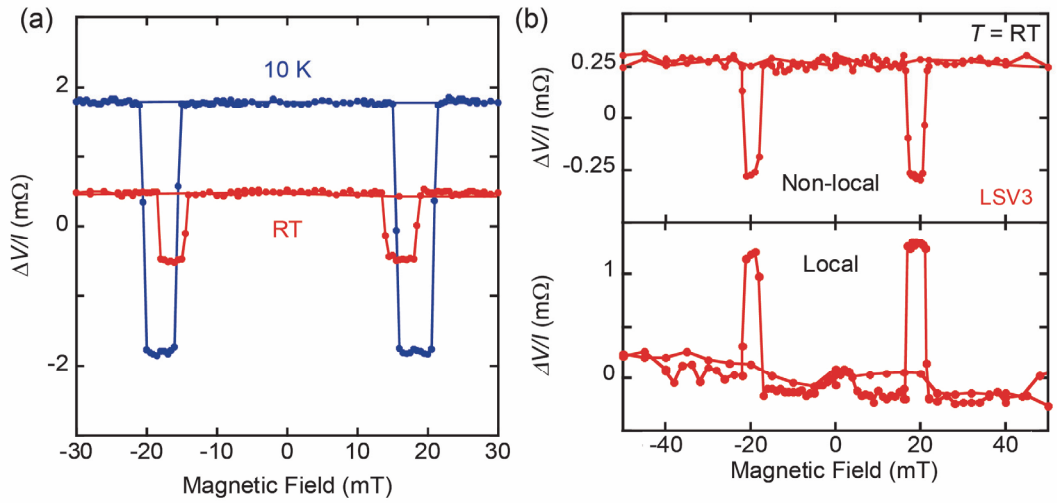

Figure 5.2: (a) Field dependence of non-local spin valve signal at 10 K and at RT for LSV3 with L = 300 nm. (b) Field dependence of non-local and local spin valve signals at RT for LSV with L = 400 nm.

antiparallel configurations of the two Py wires. ΔR_S is 1.1 and 3.6 mΩ at room temperature (RT) and 10 K, respectively. The interface resistance of the Py/Mg junction was measured where the current is applied between terminals 4 and 5 and the voltage is detected by using terminals 6 and 2, as shown in Fig. 5.1(b). The interface resistance is below the resolution ability of 1 fΩm^2 in our measurement system, and thus we assume that the Py/Mg junctions are transparent, i.e., zero interface resistance. The amplitude of ΔR_S is relatively high in the metallic LSVs with the transparent Ohmic contact such as Py/Cu, Co/Cu and Co/Al junctions [10, 15-17] implying the high spin injection efficiency of the Py/Mg junction. Figure 5.2(b) shows the field dependence of the non-local and local spin valve signals for LSV3 with L = 400 nm. For the local measurements, the current is applied between terminals 3 and 4 and then the voltage is detected by using terminals 1 and 6. As can be seen in Fig. 5.2(b), ΔR_S = 1.2 mΩ for the local spin valve measurement is 2.4 times larger than that of 0.5 mΩ for the non-local spin valve measurement, which is in reasonable agreement with the factor of 2 expected in [8].

5.2.3 Spin diffusion characteristic in Mg nanowire

Figure 5.3 shows non-local spin valve signal at 10 K for the Py/Mg devices with a variable L = 400, 600, and 800 nm. The ΔR_S decreases with increasing L due to a spin-flip scattering in the Mg nanowire. A clear spin signal ΔR_S of 1.2 mΩ is observed for the device even with the long L = 800 nm. For the LSVs with Ohmic junctions, ΔR_S can be given as a solution of one-dimensional spin dependent diffusion equation considering additional spin relaxation in the Py detector whose spin-resistance is much lower than that of NM Mg [18].

$$\Delta R_S = 4R_N \frac{\left(\frac{P_F}{1-P_F^2}\frac{R_F}{R_N}\right)^2 e^{-\frac{L}{\lambda_N}}}{\left(1+\frac{2}{1-P_F^2}\frac{R_F}{R_N}\right)^2 - e^{-\frac{2L}{\lambda_N}}}, \tag{5.1}$$

where P_F is the spin polarization for Py. $R_N = \rho_N\lambda_N/t_N w_N$ and $R_F = \rho_F\lambda_F/w_F w_N$ are the spin-resistances for Mg and Py, respectively, with resistivity ρ, spin diffusion length λ, thickness t, and width w. The subscripts F and N represent Py and Mg, respectively.

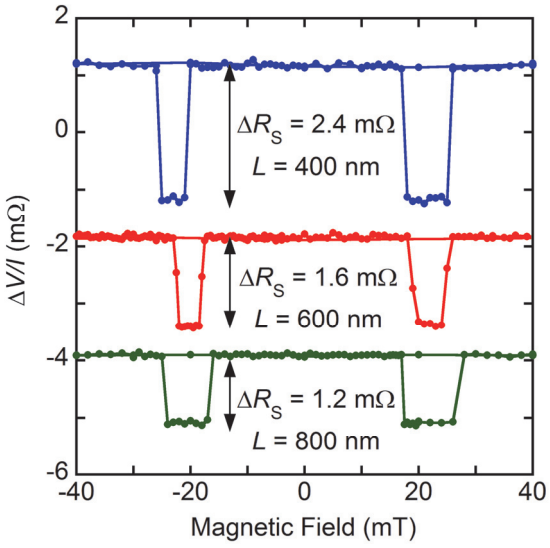

Figure 5.3: Field dependence of non-local spin valve signal at 10 K for LSV with L = 400, 600, and 800 nm.

Figure 5.4 shows the ΔR_S as a function of L at RT and 10 K and for various LSVs. ΔR_S decreases with increasing L due to a spin-flip scattering during the diffusive spin transport in the Mg nanowire. The experimental results are fitted to eqn.(5.1) by adjusting parameters P_F and λ_N. The spin diffusion length λ_F of Py is fixed to the value of 5 nm from the literature [19]. The resistivitiy of Py is 4.7×10^{-5} Ωcm at RT and 3.5×10^{-5} Ωcm at 10 K, respectively. The resistivities of Mg are 1.0×10^{-5} Ωcm for w_{Mg} = 170 nm at RT, 1.5×10^{-5} Ωcm for w_{Mg} = 110 nm at RT, and 4.0×10^{-6} Ωcm for w_{Mg} = 170 nm at 10 K, respectively.

From the fitting, the values of λ_N and P_F are found to be 720 nm and 0.43 at 10 K, and 230 nm and 0.33 at RT for LSV3, respectively. The value of P_F is relatively high in the LSV, indicating a good quality of the Py/Mg interface. The spin diffusion length of Mg shows a similar value reported for Ag, Cu and Al [9]. Among these NM materials so far used in the LSVs, Mg is a lightest element, implying a smallest SOI. However, the obtained spin diffusion length of Mg is below micron. The width dependent of the deduced fit parameters are $P_F = 0.30 \pm 0.07$ and $\lambda_N = 175 \pm 45$ nm for LSV1, $P_F = 0.27 \pm 0.03$ and $\lambda_N = 210 \pm 30$ nm for LSV2, and $P_F = 0.33 \pm 0.03$ and $\lambda_N = 230 \pm 30$ nm for

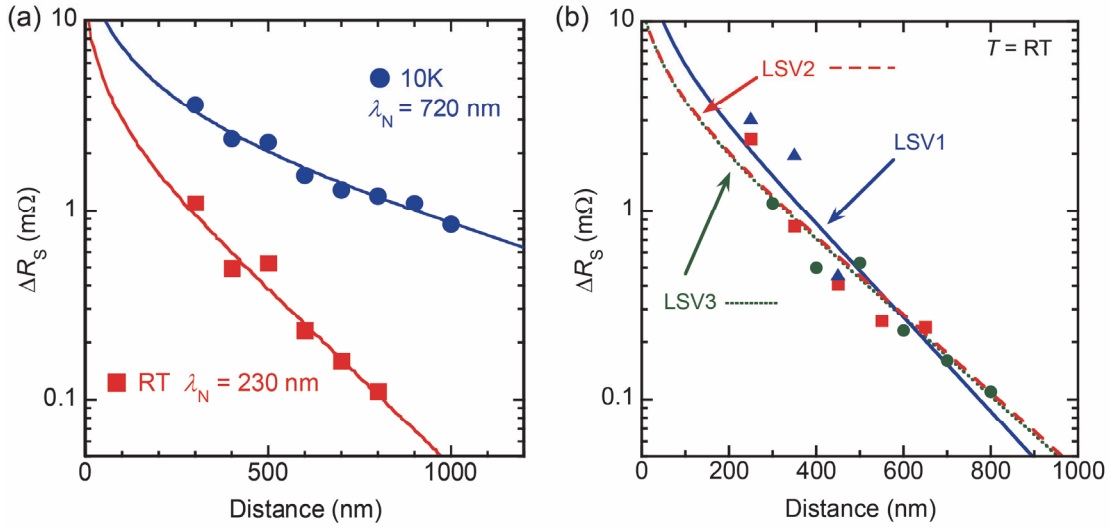

Figure 5.4: (a) L dependence of ΔR_S at RT and 10 K. The lines are fitting curves to the data set for LSV3 using eqn.(5.1). (b) L dependence of ΔR_S at RT for LSV1, LSV2 and LSV3.

LSV3. The shorter λ_N for the narrower Mg wire could be due to impurity and defect scatterings.

5.2.4 Spin relaxation mechanism in Mg

To discuss the origin of the comparable spin diffusion length in spite of small SOI for Mg, we focus on the spin-flip mechanism in the NM metal. Monod reported that the spin relaxation in metals is divided into two groups: one is the monovalent alkali and noble metals, and the other is the polyvalent metals such as Al and Mg [5]. The former group shows a universal curve in the $1/\{\tau_{sf}^{ph}(\lambda_{SOI}/\Delta E)^2\}$ vs T/T_D plot, where τ_{sf}^{ph} the spin relaxation time from phonon, λ_{SOI} the spin-orbit splitting, ΔE the energy distance between the band state in question and the state in the nearest band, and T_D the Debye temperature. The latter group has much shorter τ_{sf}^{ph} than for the monovalent metals because a complicated Fermi surface enhances a spin-flip scattering [6]. The total spin relaxation time $\tau_{sf} = \lambda_N^2 / D_N$, is deduced from λ_N determined by the injector-detector separation dependence of ΔR_S. D_N is the diffusion constant, which is determined by Einstein relation $\rho_N^{-1} = e^2 D_N N(\varepsilon_F)$, where $N(\varepsilon_F) = 1.88 \times 10^{22}$ states/eV/cm^3 is the density of state on the Fermi energy in Mg [20]. τ_{sf} of 14 ps, 13 ps and 16 ps are obtained for the Mg nanowire in LSV1, LSV2 and LSV3, respectively.

For a quantitative discussion of the spin relaxation in Mg, we revisit the expression for the total τ_{sf}

$$\frac{1}{\tau_{sf}} = \frac{1}{\tau_{sf}^{ph}} + \frac{1}{\tau_{sf}^{imp}}, \tag{5.2}$$

where τ_{sf}^{imp} is the spin relaxation time from impurities. According to the E-Y mechanism, each spin-flip process is proportional to each momentum relaxation time for the phonon and impurity scatterings [12],

$$\frac{1}{\tau_{sf}} = \frac{\varepsilon_{ph}}{\tau_e^{ph}} + \frac{\varepsilon_{imp}}{\tau_e^{imp}} \propto \varepsilon_{ph}\rho_{ph} + \varepsilon_{imp}\rho_{imp}, \tag{5.3}$$

where τ_e^{ph} and τ_e^{imp} are momentum relaxation times, and $\varepsilon_{\mathrm{ph}}$ and $\varepsilon_{\mathrm{imp}}$ are the spin-flip probabilities for phonon and impurity scatterings, respectively. ρ_{ph} and ρ_{imp} are the phonon and impurity contributions, respectively. $\tau_{\mathrm{sf}}(\mathrm{RT}) = (1/\tau_{\mathrm{sf}}^{\mathrm{ph}} + 1/\tau_{\mathrm{sf}}^{\mathrm{imp}})^{-1} = 16$ ps and $\tau_{\mathrm{sf}}(T = 10\ \mathrm{K}) = (1/\tau_{\mathrm{sf}}^{\mathrm{imp}})^{-1} = 62$ ps in LSV3, results in $\tau_{\mathrm{sf}}^{\mathrm{ph}} = 22$ ps. Therefore, one obtains $\varepsilon_{\mathrm{ph}} = \tau_{\mathrm{e}}^{\mathrm{ph}} / \tau_{\mathrm{sf}}^{\mathrm{ph}} = 0.0068$ ps / 22 ps = 3.1×10^{-4}, $\varepsilon_{\mathrm{imp}} = \tau_{\mathrm{e}}^{\mathrm{imp}} / \tau_{\mathrm{sf}}^{\mathrm{imp}} = 0.0103$ ps / 62 ps = 1.7×10^{-4}. These values are smaller than noble metals Ag and Cu and comparable to those of Al [8, 21]. However, since the diffusion constant of Mg as well as Al is an order of the magnitude smaller than those of Ag and Cu, all the resulting spin diffusion lengths are comparable. We note here that this unexpected short spin diffusion length for the light element Mg is not attributed to the quality of Mg nanowire because the residual resistivity ratio (RRR) of our Mg nanowire is 2.5, which is in the same order of magnitude reported for Cu and Al nanowires (RRR = 2.1 - 3.4) [8, 10, 15].

For the comparison of the materials with the almost same strength of the SOI, we compare the obtained τ_{sf} with that of Na e.g., the normalizing factor $(\lambda_{\mathrm{SOI}}/\Delta E)^2$ is 1.32×10^{-5} and 2.73×10^{-5} for Mg and Na, respectively [5]. τ_{sf} of the Mg nanowire is 14 ps at RT which is close to $T_{\mathrm{D}} = 290$ K, and τ_{sf} of Na is 22 ns at $T_{\mathrm{D}} = 150$ K [22]. Moreover, the spin-flip probability for Mg is two order of the magnitude larger than those of Na ($\varepsilon^{\mathrm{ph}} \sim 0.067$ ps / 22 ns = 3.0×10^{-6}, where the momentum relaxation time is obtained with Drude model [23]). Such a significant reduction of $\tau_{\mathrm{sf}}^{\mathrm{ph}}$ and $\varepsilon^{\mathrm{ph}}$ for Mg could not explain by the simple E-Y mechanism. This may be due to the existence of spin-hot-spots pointed out by Fabian and Sarma [6]. Polyvalent metals such as Al and Mg have a complex Fermi surfaces and the area with enhanced spin relaxation property near the Brillouin zone boundaries, accidental degeneracy points.

5.3 Spin relaxation mechanism in Ag

5.3.1 Experimental methods

LSVs with $Ni_{80}Fe_{20}$ (Permalloy, Py) / Ag junctions were fabricated *in-situ by multi-angle deposition technique*. First, suspended resist mask patterns consisting of a bilayer resist, 500 nm-thick methyl methacrylate and 50 nm-thick Poly methyl methacrylate, were formed on a Si/SiO_2 substrate by means of *e*-beam lithography. Then shadow evaporation was performed by using the suspended resist mask to get a clean interface: a Py layer was first *e*-beam deposited at an angle of 45 degrees from substrate normal, followed by deposition of an Ag layer normal to the substrate cooled by liquid nitrogen. Finally, a MgO capping layer was deposited to avoid surface contamination of the devices. The scanning electron microscopy image of the LSV with a non-local measurement configuration is shown in Figs. 5.5(a) and (c), and the cross-sectional transmission electron micrograph of the Ag nanowire and the corresponding energy dispersive X-ray mapping of Ag, Mg and O are shown in Fig. 5.5(b). The coverage factor of the entire surface of the wire for the MgO protection layer is estimated to be about 85%. The LSV consists of the Ag nanowire and two Py wires which are electrodes for spin injection and detection. The center to center separation L between the injector and the detector was varied from 300 nm to 1500 nm to determine λ_{sf}. To study the influence of capping layer on the spin-flip mechanism for Ag nanowires, three classes of LSVs are fabricated: without MgO capping layer with annealing (LSV1), with MgO capping layer with annealing (LSV2), and, with MgO capping layer in pristine (LSV3). LSV1 and LSV2 are annealed at 400 °C for 40 min in an N_2 (97%) and H_2 (3%) atmosphere to improve crystallographic quality of the Ag nanowire (Chapter 4). The thickness of MgO capping layer is 3 nm. The thickness of Py wires are 20 nm for all LSVs. The width of Py is 120 nm, 120 nm, and 150 nm for

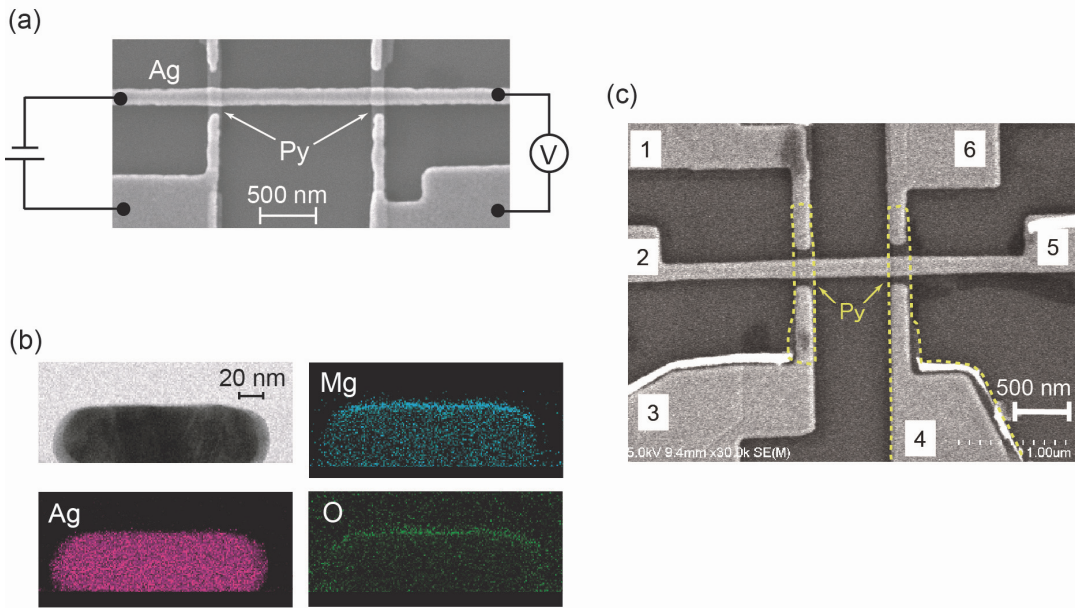

Figure 5.5: (a) Schematic diagram of the measurement circuit and a scanning electron microscope (SEM) image of LSV fabricated in this study. (b) Cross-sectional transmission electron micrograph of Ag nanowire and corresponding energy dispersive X-ray mapping for Ag, Mg and O. (c) SEM image of fabricated LSV with Py/Ag junctions. Region of Py electrode is marked by the dotted line.

LSV1, LSV2 and LSV3 respectively. The width of Ag are 150 nm, 150 nm, 200 nm, and the thickness is 50 nm, 50nm and 100 nm for LSV1, LSV2 and LSV3 respectively.[6]

5.3.2 Spin diffusion characteristics in Ag nanowire

The non-local spin injection measurements were performed on the LSVs with clean Py/Ag junctions. As shown in Fig. 5.5(c), the current is applied between terminals 5 and 4 and the voltage is detected by using terminals 2 and 3. Conventional current-bias lock-in technique with applied current of 0.30 mA and frequency of 79 Hz was used. The magnetic field was applied parallel to the Py wires. The field dependence of the spin signal for LSV with MgO capping is shown in Fig. 5.6(a). Clear spin valve signals ΔR_S were observed to be 2.45 mΩ at 300 K and 8.92 mΩ at 5 K for LSV1. Figures 5.6(b) and (d) display a reasonable decrease in ΔR_S with an increase of L,

[6] For the pristine LSV with 50-nm-thick Ag, the spin signal ΔR_S was not enough high to observe the whole range of temperature and separation L.

attributable to the spin relaxation in the Ag nanowire. Here we assume a transparent interface for the Py/Ag junction of our devices, i.e. clean interfaces confirmed by TEM analyses and very low interface resistance of the Py/Ag junction below the resolution ability of 1×10^{-3} Ωμm^2 of our measurement system. Therefore, we assume the Py/Ag junction is transparent, i.e., zero interface resistance. In this case, the analytical expression of ΔR_S can be obtained as below by solving the one-dimensional spin diffusion equation for the LSV geometry [24].

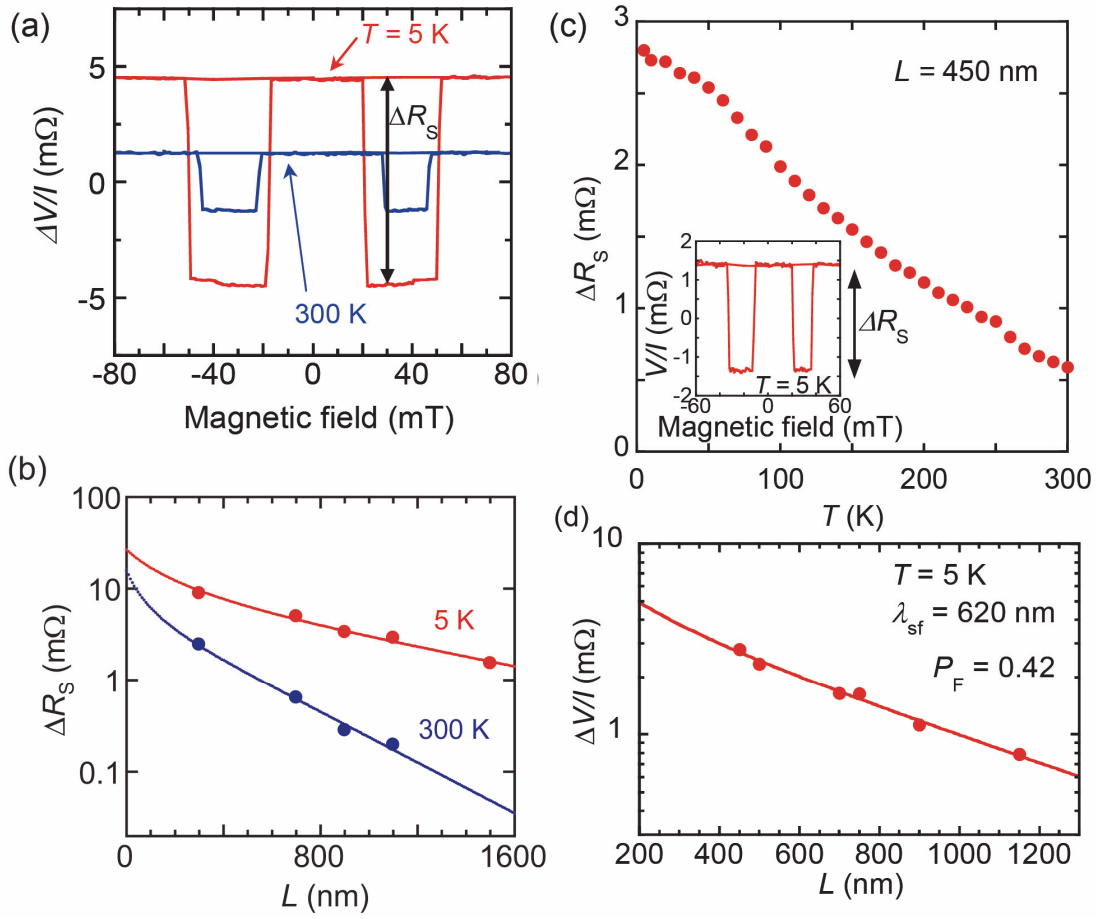

Figure 5.6: (a) Non-local spin valve signal as a function of magnetic field for LSV1 with MgO capping with L = 300 nm at T = 300 K and 5 K. (b) Spin signal as a function of L at T = 300 K and 5 K. The solid lines are the fitting curves using eqn.(5.1). (c) Temperature variation of spin valve signal for LSV3 with L = 450 nm. Inset shows field dependence of spin valve signal at T = 5 K. (d) Injector-detector separation dependence of ΔR_S at T = 5 K. Line is fitted curve using eqn.(5.1).

$$\Delta R_S = 4R_N \frac{\left(\frac{P_F}{1-P_F^2}\frac{R_F}{R_N}\right)^2 e^{-\frac{L}{\lambda_N}}}{\left(1+\frac{2}{1-P_F^2}\frac{R_F}{R_N}\right)^2 - e^{-\frac{2L}{\lambda_N}}}, \quad (5.1)$$

where P is the spin polarization of FM, $R_{Ag} = \rho_{Ag}\lambda_{Ag}/t_{Ag}w_{Ag}$ and $R_{Py} = \rho_{Py}\lambda_{Py}/w_{Py}w_{Py}$ are the spin-resistances for Ag and Py, respectively, where ρ is the resistivity, t is the thickness, and w is the width. The experimental data were fitted by adjusting parameters P_F and λ_{Ag} with setting the value of λ_{Py} = 5 nm reported by Dubois *et al.* [19]. The resistivity of Py was 4.70×10^{-5} Ωcm and 3.46×10^{-5} Ωcm at 300 K and 5 K, respectively. We then obtained $P_F = 0.343\pm0.025$ and 0.485 ± 0.015 and $\lambda_{Ag} = 316\pm28$ nm and 851 ± 98 nm, at 300 K and 5 K, respectively, for LSV1 as shown in Fig. 5.6(a). $P_F = 0.421\pm0.010$ and $\lambda_{Ag} = 618\pm41$ nm at 5 K for LSV3 as shown in Fig. 5.6(c).

5.3.3 Temperature variation of spin transport properties

Figure 5.7(a) shows the temperature dependence of λ_{Ag} for LSV1 and LSV2. For LSV without capping, λ_{Ag} shows maximum at low temperature, which is previously reported for both Cu and Ag nanowires in LSVs due to the surface spin scattering [10-12]. However, monotonic decrease in λ_{Ag} with temperature is observed for LSV with capping. The MgO capping layer could effectively suppress the surface spin-flip event. The spin relaxation time $\tau_{sf} = \lambda_{Ag}^2 / D_{Ag}$ was calculated by using the diffusion constant D_{Ag} deduced from the Einstein's relation $D_{Ag} = \left(e^2 N(\varepsilon_F)\rho_{Ag}\right)^{-1}$, with the density of states $N(\varepsilon_F) = 1.55 \times 10^{22}$ states/eV/cm^3 [20]. The temperature dependence of τ_{sf} in Fig. 5.7(b) shows that τ_{sf} stays almost constant at 16.2 ps below 30 K for LSV with capping, indicating that the phonon contribution is frozen out. The temperature increase above 30 K promotes phonon mediated scattering, resulting in a gradual decrease in τ_{sf}. According to the E-Y mechanism, the total spin relaxation time is given by

$$\frac{1}{\tau_{sf}} = \frac{1}{\tau_{sf}^{ph}} + \frac{1}{\tau_{sf}^{imp}} = \frac{\varepsilon_{ph}}{\tau_e^{ph}} + \frac{\varepsilon_{imp}}{\tau_e^{imp}}, \quad (5.4)$$

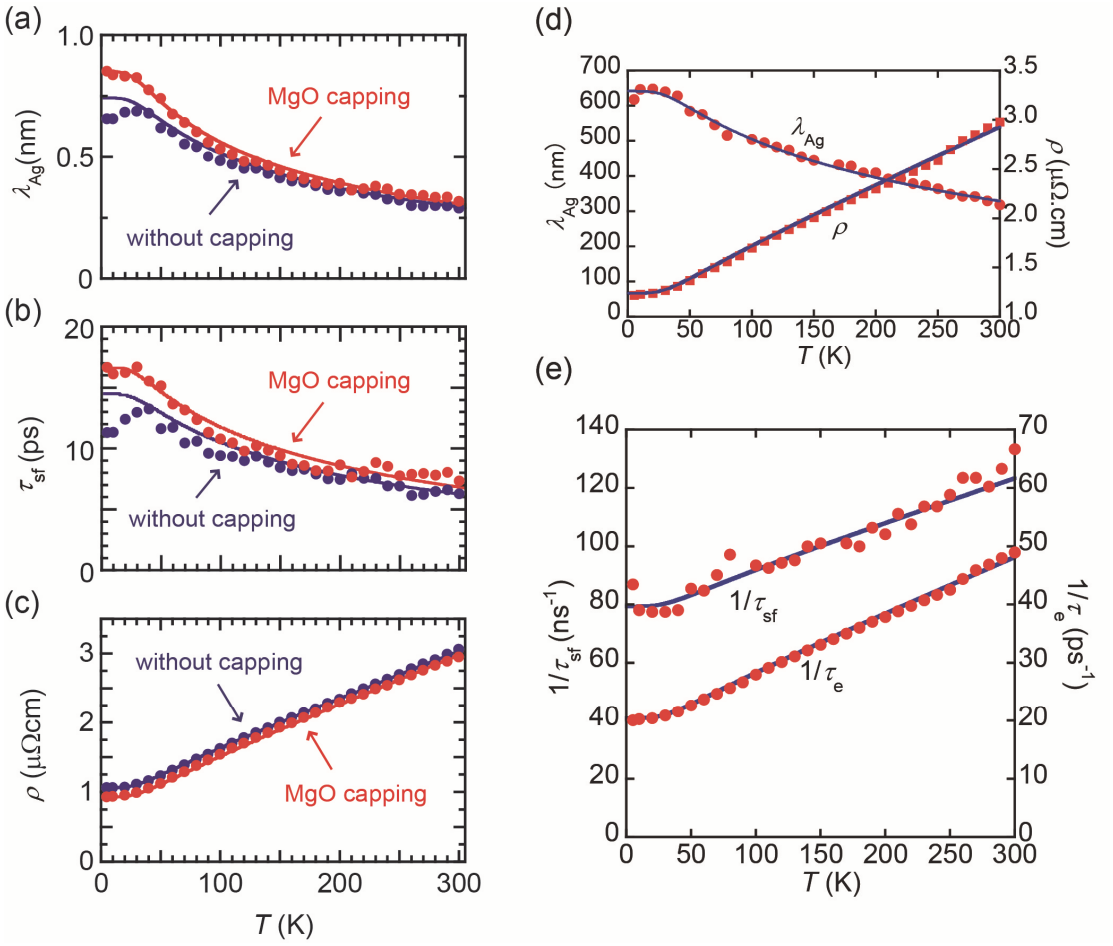

Figure 5.7: (a) Temperature dependence of spin diffusion length of Ag nanowires for LSV1 (with capping MgO, annealed) and LSV2 (without capping MgO, annealed). Solid lines show fitted curves based on the Elliott-Yafet mechanism with ε_{imp} and ε_{ph} determined from LSV with MgO capping. (b) Temperature dependence of spin relaxation time of Ag nanowire for LSV1 and LSV2. Solid lines show fitted curves obtained by the same manner as (a). Fitted curves do not contain the contribution of T-dependent surface scattering. (c) Temperature dependence of resistivity of Ag nanowire for LSV1 and LSV2. Solid lines show fitted curves for the Bloch-Grüneisen theory. (d) Temperature variation of spin diffusion length and resistivity of Ag for LSV3. Line for resistivity is fitted curve using eqn.(5.5). Line for spin diffusion length is deduced from spin-flip probabilities and resistivities due to phonon and impurity scatterings. ρ_N^{imp} is determined by the residual resistivity i.e., $\rho_N = 1.22\times10^{-6}$ Ωcm at $T = 5$ K. (e) Temperature variation of spin-flip probability and momentum relaxation probability of Ag for LSV3 (with capping MgO, pristine). Lines are fitted curves using eqn.(5.5). Impurity contribution is determined by averaging τ_{sf} for the data at the temperature below 40 K, and $\tau_{sf}^{imp} = 12.6$ ps is obtained. Fitting of $\tau_{sf}^{ph\,-1}$ results in $\Theta_D = 184$ K, and $A = 110$ ns^{-1}.

where τ_{sf}^{ph} and τ_{sf}^{imp} are spin relaxation times, τ_e^{ph} and τ_e^{imp} are momentum relaxation times, and ε_{ph} and ε_{imp} are probabilities of spin-flip scatterings. The notations "ph" and "imp" mean phonon, and impurity (including grain boundaries and T-

independent surface) mediated scatterings or probabilities, respectively. For LSV with capping, we derive the ε_{ph} and ε_{imp} by assuming the T-dependent surface spin-relaxation is suppressed to be enough small. This assumption will be examined as follows by comparing ε_{ph} and ε_{imp} from this analysis with those from bulk sample of which surface spin relaxation is negligible.

5.3.4 Universal behavior of spin relaxation in non-magnet

To compare τ_{sf}^{ph} with τ_{e}^{ph} the temperature dependence of $1/\tau_{sf}^{ph}$ and ρ_{ph} is analyzed on the basis of E-Y mechanism combined with Bloch-Grüneisen (B-G) theory describing the phonon mediated change in resistivity ρ_{ph} in the entire temperature range. With using Drude model, one obtains

$$\begin{cases} 1/\tau_{sf}^{ph} = \varepsilon_{ph} n e^2 \rho_{ph} / m_e & \text{(5.5a)} \\ \rho_{ph} = Kf\left(T/\Theta_D\right) = K\left(\dfrac{T}{\Theta_D}\right)^5 \displaystyle\int_0^{\Theta_D/T} \frac{z^5 dz}{\left(e^z-1\right)\left(1-e^{-z}\right)}, & \text{(5.5b)} \end{cases}$$

where m_e is the electron mass, n is the free electron density (= 5.86×10^{22} cm^{-3} for Ag) [25], K is a constant for a given metal and Θ_D is Debye temperature. Experimentally obtained phonon contribution to the resistivity ρ_{ph} is fitted to eqn.(5.5b) with K and Θ_D as fitting parameters. Then we obtain K and Θ_D as 5.15 × 10^{-6} Ωcm and 184 K, 4.70 × 10^{-6} Ωcm and 175 K, and 4.23 × 10^{-6} Ωcm and 184 K for LSV1 (with capping), LSV2 (without capping), and LSV3 (pristine), respectively. These are in good agreement with reported values [26]. Also, K is expressed by the analytical expression and $K = \alpha_B \rho_{\Theta_D}^{ph}$, with α_B = 4.255 [27]. Our data results in $\alpha_B \sim 4.2$, which is in reasonable agreement. As discussed previously, since the T-dependent surface scattering is assumed to be neglected on the analysis of LSV with the MgO capping layer, the constant value of τ_{sf} at the low temperatures is considered as τ_{sf}^{imp}. Hence, the temperature variation of τ_{sf}^{ph} can be deduced from eqn.(5.4). Then, by comparing ρ with τ_{sf}, we obtain ε_{ph} and ε_{imp} for the Ag nanowires in substantial agreement with reported values for the bulk: ε_{ph} and

ε_{imp} are, 2.61 × 10^{-3} and 4.03 × 10^{-3} for LSV1 and 1.6 × 10^{-3} and 3.9 × 10^{-3} for LSV3; ε_{ph} = 2.86 × 10^{-3} and ε_{imp} = 2.50 × 10^{-3} for the bulk from CESR study [28, 29]. The temperature dependence of $1/\tau_{sf}^{ph}$ is in good agreement with B-G curve based on CESR study [28], as shown in Fig. 5.8(a), which reflects intrinsic feature of Ag. Material dependence of $\tau_{sf}^{ph\text{-}1}$ is discussed by Monod and Benue [5], and more recently Fabian and Das Sarma pointed out the relation between τ_{sf}^{ph} and $\rho_{\Theta_D}^{ph}$ [7]. For monovalent metals, the material dependence of $\tau_{sf}^{ph\text{-}1}$ is ruled by $\tau_{sf}^{ph\text{-}1} \propto \rho_{\Theta_D}^{ph}(\lambda_{SOI}/\Delta E)^2$, where λ_{SOI} is the spin-orbit splitting and ΔE is the separation to the nearest band with the same transformation properties [2]. Therefore, by using Drude model, ε is expressed as $\varepsilon \equiv \tau_e^{ph}/\tau_{sf}^{ph} \propto (\lambda_{SOI}/\Delta E)^2/n$, and it follows that $\varepsilon_{Ag}/\varepsilon_{Cu} \sim 0.7$ [2, 5, 25]. In this way both LSV and CESR results are found consistent with the B-G theory in the entire temperature range and now the assumption is validated that *T*-dependent surface spin-relaxation is negligible on LSV with MgO capping.

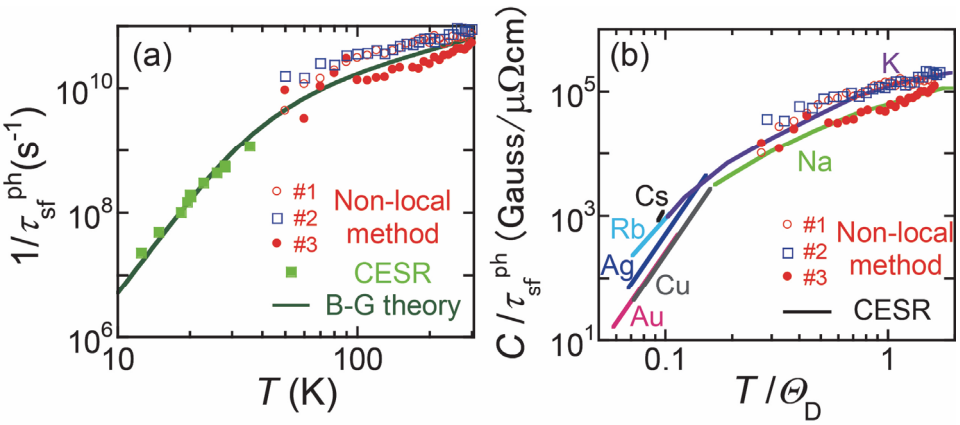

Figure 5.8: (a) Temperature dependence of spin relaxation rate *via* phonon scattering. Open circles, open rectangle, closed circles, and closed rectangles show experimental data for the Ag nanowires in the non-local spin injection measurement of LSV1 (with capping MgO, annealed), LSV2 (without capping MgO, annealed), LSV3 (with capping MgO, pristine), and Ag foil in the conduction electron spin resonance (CESR) experiment (from [28]), respectively. The solid line shows the theoretical curve of the B-G model. (b) Revised Monod-Beuneu plot, C/τ_{sf}^{ph} vs T/Θ_D, with experimental data for spin injection and CESR measurements (from [5, 7]) for noble and monovalent metals, where Θ_D is the Debye Temperature and *C* is the material constant $(\Delta E/\lambda_{SOI})^2/\gamma_e/\rho_{\Theta_D}$ (see the text for the definition).

To clarify the suppression of surface spin-relaxation, LSV with the capping layer is compared to LSV without capping. For LSV without capping, we observe peak structure at low temperature. Hence, we formulate the spin relaxation as $1/\tau_{sf} = 1/\tau_{sf}^{ph} + 1/\tau_{sf}^{imp} + 1/\tau_{sf}^{surf}$ where τ_{sf}^{surf} denotes T-dependent surface spin-relaxation time. Then, the temperature dependence of $\bar{\lambda} = \sqrt{D_N \bar{\tau}_{sf}}$ and $\bar{\tau}_{sf}^{-1} \equiv \left(\tau_{sf}^{ph}\right)^{-1} + \left(\tau_{sf}^{imp}\right)^{-1}$ is calculated by using ρ in combination with obtained value of ε_{ph} and ε_{imp} based on LSV with capping layer. As shown in Figs. 5.7 (a) and (b), the calculated values on LSV with capping layer well reproduce the temperature dependence whereas those without capping layer shows the clear deviation from experimental data especially below T = 40 K. It means that the surface scattering is pronounced on LSV without capping layer. We shall note here that quantitative model of T-dependent surface scattering is proposed in [12]. However, it cannot be directly applied on the highly conducting sample including the sample in the present study[7]. Thus, to clarify the surface spin-relaxation quantitatively, further study is required. The possible origin of the reduction of surface spin relaxation is as follows. Surface spin-flip is dominated by SOI [30, 31]. Thus, the surface spin-flip probability, ε_{surf}, is of the order of the magnitude, $(\alpha Z)^4$, where $\alpha = e^2/\hbar c$ and Z is an atomic number [30, 31]. In the present study, the MgO capping layer decreases effective Z at the surface, may resulting in suppression of the spin-flip scattering.

As in eqn.(5.5b), reduced resistivity $\rho/K = f(T/\Theta_D)$ is material independent. Eqn.(5.5a) shows that the spin-lattice relaxation is also material independent after proper scaling by considering the SOI. Based on E-Y mechanism, Monod and Benue estimated a magnitude of the effect of the SOI interaction as $\lambda_{SOI}/\Delta E$ where λ_{SOI} is the spin-orbit splitting and ΔE is the separation to the nearest band with the same transformation properties [2]. Then they found the reduced temperature dependence of

[7] Eqn. 5 in [12] cannot be used for highly conductive samples with $\tau_e > (4a)^{-1/2}$, where $a = (v_F/d)2/3\gamma$, v_F, d and γ are Fermi velocity, thickness and geometrical factor, respectively.

$1/\tau_{sf}^{ph}$ /(λ_{SOI} /ΔE)^2 in CESR data shows material independent B-G curve for noble and monovalent alkali metals. In eqn.(5.5), by substituting representative value of (λ_{SOI} /ΔE)^2 into ε, spin flip rate is expressed as, $C/\tau_{sf}^{ph} \sim Bf\left(T/\Theta_D\right)$ where C is the material constant $\left(\Delta E/\lambda_{SOI}\right)^2/\gamma_e/\rho_{\Theta_D}$, $\gamma_e = g\mu_B/\hbar$ is the gyromagnetic ratio, g is the g-factor and μ_B is the Bohr magneton and B is constant $\alpha_B n e^2 m_e/\gamma_e$. Revised Monod-Beuneu scaling [7] of C/τ_{sf}^{ph} vs T/Θ_D is shown in Fig .5.8(b) for CESR data of noble and monovalent alkali metals together with the non-local spin injection data for the Ag nanowire. The experimental data in the present study fall well on to the universal curve which reflects intrinsic feature of the Ag nanowire.

5.4 Conclusion for chapter 5

In the first part, we have examined the spin diffusion characteristics in LSVs consisting of Py spin injector and detector electrodes bridged by Mg nanowire. Clear spin signals are observed for all the devices in the present study. Non-local and local spin valve signals show the same switching characteristics and the amplitude of the local spin valve signal is 2.4 times larger than that of the non-local spin valve signal, which assure that one-dimensional spin diffusion model is applicable to explain the observed spin valve behaviors in the Py/Mg devices. The amplitude of the spin signal is relatively large among LSVs with transparent Ohmic junctions. The spin diffusion length of Mg is found to be 720 nm at T = 10 K and 230 nm at RT from the measurement of the spin valve signal as a function of the separation L. The obtained spin diffusion lengths for Mg are not much longer than those for Al, Cu and Ag, although the obtained spin-flip probabilities for Mg is $\varepsilon_{ph} = 3.1 \times 10^{-4}$, $\varepsilon_{imp} = 1.7 \times 10^{-4}$, are little smaller than those of Ag and Cu but comparable with those of Al. These are considered due to the small diffusion constant for Al and Mg. The spin-flip probabilities for Mg *via* phonon scatterings are two order of the magnitude larger than one for Na where the strengths of the SOI for these materials are comparable, which is consistent with the theoretical

prediction by Fabian and Das Sarma: possibly because of the enhanced spin relaxation near the special points for polyvalent metals in momentum space called as spin–hot-spots.

In the second part, we have investigated the spin relaxation mechanism in NM nanowire by characterizing spin transport properties of Mg in LSVs. The spin-flip probability caused by phonon and impurity scatterings is precisely determined because a surface spin scattering of the Ag wire is well suppressed by an MgO capping layer. This may be due to a decrease of effective Z at the surface. The spin relaxation mechanism can be explained in the framework of the conventional Elliott-Yafet model. The temperature dependence of the spin relaxation times due to phonon scattering for the Ag nanowire is well fitted to the B-G formula. The fitting curve is in good agreement with the reported spin relaxation times of Ag foils used in the CESR measurement, which reflects intrinsic feature of Ag. From ε^{ph}, ε^{imp}, ρ_N^{ph} and ρ_N^{imp}, we can deduce the temperature variation of τ_{sf} and D_N, and thus, λ_N can be also deduced from $\lambda_N = \sqrt{D_N \tau_{sf}}$ in the entire temperature range as in Figs. 5.7 (a) and (d). The experiment data in the present study fall on to the universal curve for monovalent metals in the revised Monod-Beuneu scaling. These allow us to determine the spin relaxation time for phonon scattering in the monovalent metals at any temperatures and to understand the spin-flip mechanism in the NM nanowires.

References for chapter 5

[1] R. J. Elliott, *Physical Review* **96**, 266 (1954).

[2] Y. Yafet, *Solid State Physics* **14**, 1 (1963).

[3] A. W. Overhauser, *Physical Review* **89**, 689 (1953).

[4] F. Beuneu and P. Monod, *Physical Review B* **18**, 2422 (1978).

[5] P. Monod and F. Beuneu, *Physical Review B* **19**, 911 (1979).

[6] J. Fabian and S. Das Sarma, *Physical Review Letters* **81**, 5624 (1998).

[7] J. Fabian and S. Das Sarma, *Journal of Vacuum Science & Technology B: Microelectronics and Nanometer Structures* **17**, 1708 (1999).

[8] F. Jedema, M. Nijboer, A. T. Filip, and B. J. van Wees, *Physical Review B* **67**, 085319 (2003).

[9] J. Bass and W. P. Pratt, *Journal of Physics: Condensed Matter* **19**, 183201 (2007).

[10] T. Kimura, T. Sato, and Y. Otani, *Physical Review Letters* **100**, 0666021 (2008).

[11] M. Erekhinsky, A. Sharoni, F. l. Casanova, and I. K. Schuller, *Applied Physics Letters* **96**, 022513 (2010).

[12] G. Mihajlović, J. E. Pearson, S. D. Bader, and A. Hoffmann, *Physical Review Letters* **104**, 237202 (2010).

[13] F. Bloch, *Z. Physik* **59**, 208 (1930).

[14] E. Grüneisen, *Annalen der Physik* **408**, 530 (1933).

[15] F. Jedema, A. T. Filip, and B. J. van Wees, *Nature* **410**, 345 (2001).

[16] Y. Ji, A. Hoffmann, J. E. Pearson, and S. D. Bader, *Applied Physics Letters* **88**, 052509 (2006).

[17] F. Casanova, A. Sharoni, M. Erekhinsky, and I. Schuller, *Physical Review B* **79**, 184415 (2009).

[18] S. Takahashi and S. Maekawa, *Physical Review B* **67**, 052409 (2003).

[19] S. Dubois, L. Piraux, J. M. George, K. Ounadjela, J. L. Duvail, and A. Fert, *Physical Review B* **60**, 477 (1999).

[20] D. Papaconstantopoulos, *Handbook of the band structure of elemental solids* (Plenum Press New York, 1986).

[21] H. Idzuchi, Y. Fukuma, L. Wang, and Y. Otani, *Applied Physics Letters* **101**, 022415 (2012).

[22] F. Vescial, N. S. VanderVen, and R. T. Schumacher, *Physical Review* **134**, A1286 (1964).

[23] J. S. Dugdale and D. Gugan, *Proceedings of the Royal Society of London. Series A. Mathematical and Physical Sciences* **270**, 186 (1962).

[24] S. Takahashi and S. Maekawa, *Physica C: Superconductivity* **437-438**, 309 (2006).

[25] N. W. Ashcroft and N. D. Mermin, *Solid state physics.* (Brooks Cole, United States, 1976), p.^pp. 5.

[26] A. Bid, A. Bora, and A. Raychaudhuri, *Physical Review B* **74**, 035426 (2006).
[27] P. L. Rossiter and J. Bass, in *Electronic and Magnetic Properties of Metals and Ceramics PartI*, edited by K. H. J. Buschow (Weinheim, New York, 1993), pp. 257.
[28] M. R. Shanabarger, Ph. D. dissertation, University of Calfornia, San Diego, 1970.
[29] F. Beuneu and P. Monod, *Physical Review B* **13**, 3424 (1976).
[30] R. Meservey and P. Tedrow, *Physical Review Letters* **41**, 805 (1978).
[31] A. A. Abrikosov and L. P. Gor'kov, *Sov. Phys. JETP* **15**, 752 (1962).

Chapter 6

Dynamic spin transport properties of spin current

6.1 Introduction

The velocity of spin current has been analyzed by a response of spin precession and dephasing since the pioneering work of Johnson and Silsbee in 1985 [1] and this so-called Hanle effect analysis has been used for extracting the spin relaxation time, the velocity and the transit-time distribution between the injector and the detector [2-7]. However, recent experimental progress in creating spin currents revealed new experimental results which could not be explained by the previous theoretical framework. For example, the Hanle analyses of dynamic spin transport properties of graphene, recently performed by assuming an empirical transit-time distribution, yielded strikingly different spin relaxation times depending on the type of contacts although intrinsic spin transport properties of non-magnet (NM) should be an independent parameter of the contact type [6]. In the case of silicon, the experimental Hanle signals could not be fully described by the empirical model based on a drift-dominated transit-time distribution in spin-transport of semiconductor [8, 9]. For GaAs, solid analysis of spin relaxation in a two-dimensional electron gas is hampered by complexities of charge and spin transports [10, 11]. Therefore, it is essential to provide a framework for understanding the dynamic spin transport properties in non-magnetic (NM) materials.

In the first part of the chapter 6, we establish the formalism of the Hanle effect to characterize intrinsic spin transport properties in NM materials. The experimental studies are based on metallic lateral spin valves (LSVs), which have comparative advantage in designing the measurement scheme owing to clear physics of charge and spin transport and spin relaxation mechanism [12, 13], good controllability of

dimensions where one-dimensional transport model is applicable, and comparability of junction property from low resistive transparent junctions to high resistive tunnel junctions [2, 5, 7, 12-19]. As a consequence, we have succeeded in identifying the impact of spin absorption effect on the deduced spin relaxation time and obtaining intrinsic spin relaxation time which is comparable with other experimental probes such as conduction electron resonance.

In the second part of the Chapter 6, we study the coherence of spin precession in the Hanle effect. With the aid of the techniques to generate large spin accumulation discussed in the Chapter 4, we observe long-distance spin precession and characterize the transport and relaxation mechanisms. In ballistic spin transport, spins can coherently rotate at a frequency proportional to the applied magnetic field. This allows us to control the direction of the spins in the channel and to manipulate the output signal of LSVs by adjusting an effective external parameter such as the Rashba field tunable via a gate voltage [20]. This scheme realizes an active spin device such as the spin-transistor [21]. However, in a diffusive pure spin current in NMs, the precession causes dephasing, and decreases drastically the spin accumulation [3, 4, 22-27]. In this section we show the LSVs with dual injectors enable us to detect a genuine in-plane precession signal from the Hanle effect with no spurious signals, demonstrating the phase coherency in precession is improved with an increase of the channel length. The coherency in the spin precession shows a universal behavior as a function of the normalized separation between the injector and the detector in material-independent fashion for metals and semiconductors including graphene.

6.2 The effect of spin absorption on Hanle effect

6.2.1 The effect of spin absorption on Hanle signal

In order to establish a model of dynamic spin-transport, the response of spin precession in magnetic fields, namely, the Hanle effect was measured in various LSVs with $Ni_{80}Fe_{20}$(Permalloy, Py)/Ag Ohmic and with Py/MgO/Ag junctions. Samples (Fig. 6.1) were prepared on a Si/SiO_2 substrate with a suspended resist-mask by using shadow evaporation technique [19] and fabricated LSVs consist of two ferromagnetic (FM) Py wires (140-nm-wide and 20-nm-thick) bridged by a NM Ag wire (100-140 nm-wide and 100-nm-thick). When the current is applied to the Py/(MgO/)Ag injector junction, the diffusive spin current is generated in the NM wire. With the perpendicular magnetic field B_z applied, the spins begin to precess, which changes the output signals of the devices [1, 2], and the transit time for the spin t is deduced from a change of the angle in the orientation at the detector. Figure 6.1 shows Hanle signal for LSVs with both the Py/Ag and Py/MgO/Ag junctions, with the injector-detector separation L varied from 3.00 μm to 6.00 μm. The ΔR_S corresponds to the difference in non-local resistances

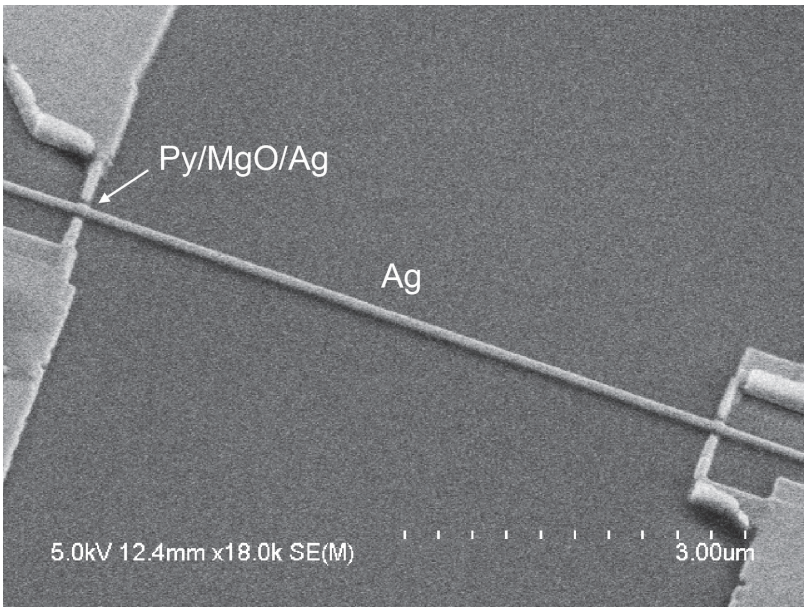

Figure 6.1: Scanning electron microscope (SEM) images of fabricated lateral spin valve devices.

between the parallel and antiparallel magnetic configurations of the injector and the detector at $B_Z = 0$. The value of ΔR_S decreases with increasing L because the spin accumulation decreases due to the spin relaxation in Ag [13]. Also, the values of ΔR_S for the Py/Ag junctions are reasonably smaller than those for Py/MgO/Ag junctions due to the spin-resistance mismatch [14, 19]: in the case of the Ohmic Py/Ag junction, the spin current in the Ag wire is absorbed into Py, which is expected from very low

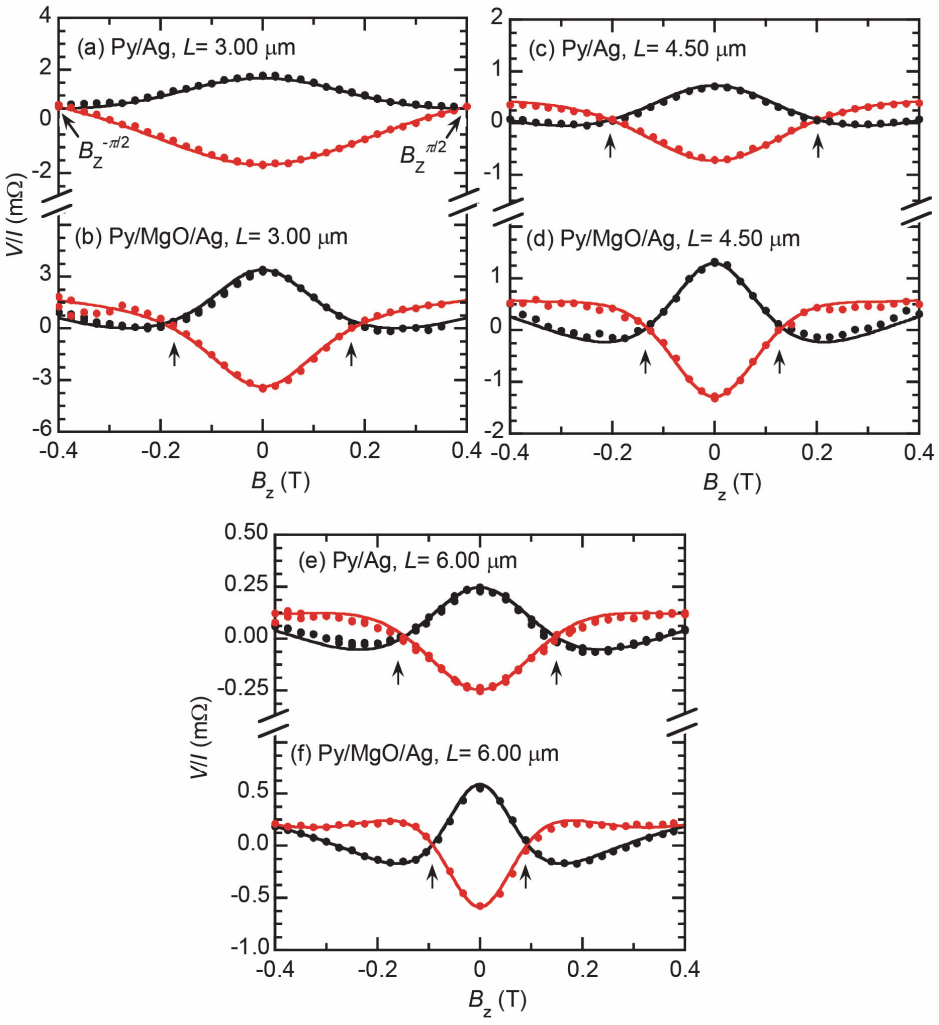

Figure 6.2: Hanle signal in LSVs with Py/Ag junctions and Py/MgO/Ag junctions with various separations L. Black and red circles show non-local resistance V/I of parallel and antiparallel magnetic configurations of the injector and detector electrodes, respectively at $T = 10$ K. Curves are obtained by the formula of Hanle effect (eqns.(2.43) and (2.54)) with adjusting parameters shown in Table I. Arrows ($B_z^{\pi/2}$ and $B_z^{-\pi/2}$) show the first cross-points of the Hanle signal for the parallel and antiparallel configurations corresponding to the collective $\pm\pi/2$ rotation of diffusive spins.

interface resistance R_I for Py/Ag. In Fig. 6.2, the first cross-point $B_z^{\pi/2}$ of the Hanle signal for the parallel and antiparallel magnetic configuration of the injector and detector Py wires corresponds to the transit time when the collective $\pi/2$ rotation of diffusive spins is completed. The $B_z^{\pi/2}$ decreases with increasing L because of the increased transit time in the Ag wire. Figure 6.2 also shows that the magnitude of $B_z^{\pi/2}$ alters depending on the type of junctions: for LSV with L = 6.00 μm, the Py/Ag junctions give $B_z^{\pi/2}$ ~ ± 148 mT whereas the Py/MgO/Ag junctions give ± 92 mT. These values correspond to $\omega_L^{\pi/2} \sim 2.60 \times 10^{10}$ s^{-1} and 1.62×10^{10} s^{-1}, respectively, indicating that faster spin diffusion for the Py/Ag junctions compared with the Py/MgO/Ag junctions. This tendency was consistently observed in the LSVs both with L = 4.50 μm and 3.00 μm, the latter of which has the most pronounced difference in $B_z^{\pi/2}$ between the LSVs with Py/Ag and Py/MgO/Ag junctions.

6.2.2 The analysis of transit-time distribution

In order to understand more explicitly the effect of the spin absorption on the dynamic property of spin transport, the transit-time distribution was examined. Hanle signal is described by integrating the transit-time distribution with Larmor precession as

$$V \propto \int_0^\infty dt\, S_y(x = L, t) \equiv \int_0^\infty dt P(t) \cos(\omega_L t) \tag{6.1}$$

where $S_y(x=L,t)$ is the net spin density along the y direction parallel to the easy axis of the ferromagnet (FM) at the detector, t is the transit time and $P(t)$ is the transit-time distribution of the net spin density given by its modulus $S(L,t) = [S_x^2(L,t) + S_y^2(L,t)]^{1/2}$ [2, 7]. This means that spins injected at x=0 arrive at the detector position with a probability of $P(t)$ and the detection voltage is proportional to the integrated y-component spin density $S(x=L,t)\cos(\omega_L t)$ with respect to all the possible transit time. Since the spin current is diffusive, there is a finite time to travel across NM Ag wire. After the spin begins to reach the detector, the $P(t)$ increases until the spin-flip nature

appears, i.e., the transit time becomes comparable to the spin relaxation time. As a result, the transit-time distribution exhibits a typical peak structure as shown in Fig. 6.3(a), and is usually described by an empirical distribution

$$P_{em}(t) = \frac{1}{\sqrt{4\pi D_N t}} \exp\left[-\left(L^2/4D_N t\right) - \left(t/\tau_{sf}\right)\right], \tag{6.2}$$

where D_N is the diffusion constant for spin and τ_{sf} is the spin relaxation time [2]. Considering the fact that the Hanle signal is given by eqn.(6.1), $P(t)$ can be directly derived by applying Fourier transform to the experimental Hanle signal [8]. Figures 6.2(a) and 6.2(b) show the derived $P(t)$ by performing Fourier transform for the 6 μm spin transport in LSVs. In the case of LSVs with the Py/MgO/Ag junctions, experimental data agree excellently with the curve obtained from an empirical model (eqn.(6.2)) with the spin relaxation time in table I and the diffusion constant derived with Einstein relation, which validates this scheme. On the other hand, in the case of LSVs with the Py/Ag junctions, $P(t)$ from Fourier transform is shifted to the left-hand

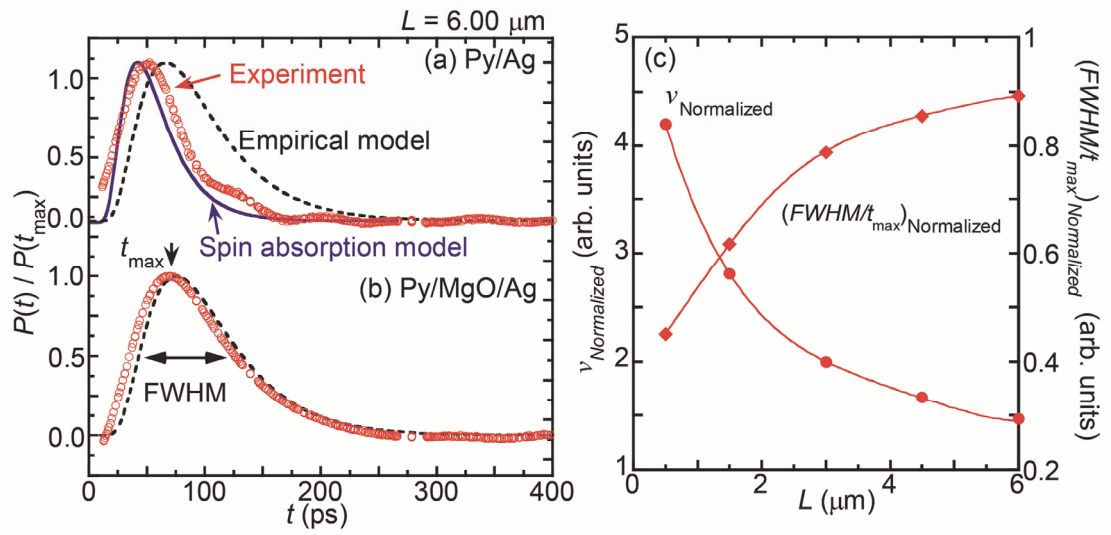

Figure 6.3: (a),(b) Derived transit time distribution of pure spin current $P(t)$ (red circle) by performing Fourier transform on Hanle signal shown in Fig. 6.2(e) and (f). Dashed curves are derived by the empirical model, i.e., diffusion distribution with spin-flip expressed by eqn. (6.2), with the values of D_N and τ_{sf} listed in Table I. Solid curve shows the distribution including the effect of spin absorption. All $P(t)$ is normalized by $P(t_{max})$ where t_{max} gives the maximum of $P(t)$. (c) Velocity and full width at half maximum (FWHM) for spin absorption model normalized by those for empirical model. Lines are guides to the eyes.

side with respect to the one expected from the empirical equation (6.2), suggesting the faster spin diffusion. The experimental $P(t)$ is remarkably different from the empirical equation (6.2); this makes us desire to construct the model of transit-time distribution to go beyond the empirical one which does not consider the spin absorption.

In order to gain the insight of the effect of spin absorption on the dynamic properties of spin currents in NM, we formulate the Hanle effect for LSVs with low resistive Ohmic junctions to tunnel junctions. For this, following two issues have to be fully taken into account: firstly, the spin absorption by both injector and detector FMs, affects a spatial distribution of electro chemical potential [28]. In addition to it, a recent experiment of Ghosh *et al.* showed that spin relaxation processes in FMs were different between longitudinal and transverse spin currents [29]. Their results suggest that the spin relaxation is expected to be more pronounced when the diffusive spins are oriented perpendicular to the magnetization of the detector via precession. The longitudinal component of spin current $I_{Si}^{\parallel}$ through i-th junction ($i = 1, 2$) is described as $I_{Si}^{\parallel} = P_{\mathrm{I}i} G_{\mathrm{I}i} \bar{\mu}_{\mathrm{F}i} / e + (G_{\mathrm{I}i}/2e)[\delta\mu_{\mathrm{F}i} - \delta\mu_{\parallel}(x_i)]$, where $P_{\mathrm{I}i}$ is the interfacial-current spin-polarization, $G_{\mathrm{I}i}$ is the interface conductance, $\bar{\mu}_{\mathrm{F}i} = (\mu_{\mathrm{F}i}^{\uparrow} + \mu_{\mathrm{F}i}^{\downarrow})/2$, $\mu_{\mathrm{F}i}^{\uparrow(\downarrow)}$ is the spin-dependent electro chemical potential of F_i, $\delta\mu_{\mathrm{F}i}$ is the spin accumulation of FM_i at the interface, $\delta\mu_{\parallel}(x) = S_y(x)/N(\varepsilon_{\mathrm{F}})$ is the longitudinal component of spin accumulation in the Ag wire, $N(\varepsilon_{\mathrm{F}})$ is the density of state at Fermi energy, and x_i is the contact position ($x_1 = 0$, $x_2 = L$). $I_{Si}^{\parallel}$ is inversely proportional to the spin-resistance of i-th FM $R_{\mathrm{F}i}$, as schematically shown in Fig. 6.4(a). In the presence of transverse spin accumulation $\delta\mu_{\perp}(x) = S_x(x)/N(0)$, the transverse spin current $I_{Si}^{\perp}$ is given by $I_{Si}^{\perp} = (G_{\uparrow\downarrow,i}/e)\delta\mu_{\perp}(x_i)$, where $G_{\uparrow\downarrow,i}$ is the real part of spin mixing conductance at the i-th interface [30] as schematically shown in Fig. 6.4(b). The spatial distribution of $\delta\mu_{\perp}$ and $\delta\mu_{\parallel}$ are illustrated in Figs. 6.4(c) and 6.4(d) with considering different

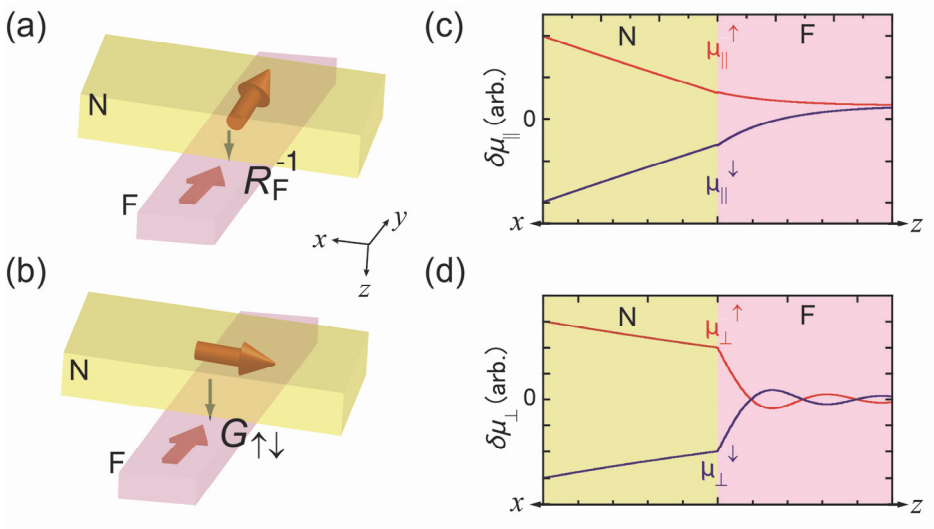

Figure 6.4: (a) Absorbed longitudinal spin current $I_{S\parallel}$ is proportional to longitudinal spin accumulation $\delta\mu_{\parallel}$ and inversely proportional to the spin-resistance of FM R_F. (b) Absorbed transverse spin current $I_{S\perp}$ is proportional to transverse spin accumulation $\delta\mu_{\perp}$ and the real part of spin mixing conductance $G\uparrow\downarrow$. (c), (d) Schematic of $\delta\mu_{\parallel}$ and $\delta\mu_{\perp}$ in the vicinity of the detector junction. In FM, $\delta\mu_{\perp}$ is decaying with precessing along the magnetization direction, which results in damping with oscillation [31]. The red and blue curves are calculated by the spin diffusion equation with using the eqn.(48) in [31].

mechanism of spin absorption for longitudinal and transverse spin accumulation, based on the model of Stiles and Zangwill [31]. The spin accumulations, $\delta\mu_{\parallel}(x)$ and $\delta\mu_{\perp}(x)$ in the Ag nanowire are given by the complex representation $\delta\tilde{\mu}(x,t)=\delta\mu_{\parallel}(x)+i\delta\mu_{\perp}(x)$

$$\delta\tilde{\mu}(x)=\frac{I_{S1}^{\parallel}+iI_{S1}^{\perp}}{2eN(\varepsilon_F)A_N}\int_0^{\infty}dtP_{em}(x,t)e^{i\omega_L t}+\frac{I_{S2}^{\parallel}+iI_{S2}^{\perp}}{2eN(\varepsilon_F)A_N}\int_0^{\infty}dtP_{em}(x-L,t)e^{i\omega_L t} \qquad (6.3)$$

and the spin current density in the complex representation is $\tilde{j}_S(x)=-(\sigma_N/2e)\nabla\delta\tilde{\mu}(x)$, where σ_N is the electrical conductivity of the Ag wire. Using the boundary conditions that the spin and charge currents are continuous at the interfaces of junctions 1 and 2, we obtain the spin accumulation voltage $V_2\equiv V$ detected by Py and the non-local resistance V/I of Hanle signal in LSV (eqn.(2.43)). When the junctions are the tunnel type, the Hanle signal reduces to the conventional expression in LSVs eqn.(2.30) in the limit of small spin absorption.

6.2.3 Evaluation of the spin relaxation time

The experimental results are well reproduced by the present theoretical calculations using reasonable parameters listed in Table I, as can be seen in Fig. 6.3. The obtained spin polarizations P_F and P_I agree well with our previous results [19] and values reported in ref. [32]. The resistivity of Py was 1.75×10^{-5} Ωcm. The junction resistance of Py/MgO/Ag was 20 Ω, which is enough higher compared with spin-resistance $R_{Ag} = \rho_N\lambda_N/A_N = 1$ Ω. The interfacial resistance of Ohmic Py/Ag junctions and the spin diffusion length of Py are taken as $R_IA_J = 5 \times 10^{-4}$ Ω(μm)^2 [32] and λ_{Py} = 5 nm [33], respectively from the literature. $D_N = 612 \pm 19$ cm^2/s is derived from Einstein relation $\sigma_N = e^2D_NN(\varepsilon_F)$ where $N(\varepsilon_F)$ = 1.55 states/eV/cm^3 [34]. While the shape of Hanle signal is drastically modified by the junctions as in Fig. 6.2, the spin relaxation times for Py/Ag and Py/MgO/Ag junctions are well agreed as 40.8 ± 6.2 ps and 40.3 ± 7.3 ps. The spin relaxation mechanism is characterized by the spin-flip probability $\varepsilon \equiv \tau_e/\tau_{sf}$ with respect to the momentum relaxation time τ_e. For Ag, ε = 0.10 ps / 40 ps = 2.5×10^{-3} in this study is consistent with that (2.50×10^{-3}) deduced form conduction electron spin resonance [35], in which spin relaxation mechanism was established as Elliott-Yafet mechanism. The agreement of a between the measurements is also

Table I: Adjusting parameters for Hanle signals which are shown in Fig. 6.2.

Junction	L (μm)	P_F	$P_{I(Py/MgO/Ag)}$	$P_{I(Py/Ag)}$	τ_{sf} (ps)	$G\uparrow\downarrow$ (m$^{-2}\Omega^{-1}$)
Py/Ag	3.00	0.57 ± 0.04	N/A	0.80 ± 0.03	40.3 ± 5.3	$(3.5 \pm 0.9) \times 10^{14}$
Py/MgO/Ag	3.00	N/A	0.28 ± 0.02	N/A	38.0 ± 3.9	N/A
Py/Ag	4.50	0.51 ± 0.14	N/A	0.80 ± 0.10	39.3 ± 5.1	$(2.0 \pm 0.9) \times 10^{14}$
Py/MgO/Ag	4.50	N/A	0.33 ± 0.05	N/A	38.0 ± 6.4	N/A
Py/Ag	6.00	0.55 ± 0.12	N/A	0.76 ± 0.06	42.9 ± 7.9	$(3.6 \pm 8.4) \times 10^{14}$
Py/MgO/Ag	6.00	N/A	0.26 ± 0.07	N/A	45.0 ± 10.2	N/A

reported for Al and Cu [1, 12]. Therefore, the spin relaxation time obtained in this study reflects intrinsic properties of Ag, in which characterization was enabled by the well-designed device structure, e.g., the spin transport channel is much longer than the junction size and surface spin scattering is suppressed by capping layer [13]. In addition to it, the Fourier transform of the theoretical Hanle signal agrees with the experimental $P(t)$ not only for LSVs with Py/MgO/Ag junctions but also for Py/Ag junctions, which complimentary supports the validity of our model. These results show that eqn.(6.1) cannot be used with the most widely used $P(t) = P_{em}(t)$ to analyze Hanle signal in LSVs of which R_I is lower than R_N due to the spin absorption effect. They may provide spurious spin relaxation times with mimicking signals or in some cases with different shapes of Hanle signals. In other words, the same spin relaxation time results in the different Hanle signal with and without spin absorption, the former of which exhibits a broader signal as shown in Fig. 6.2. This tendency is consistent with the reported Hanle signals in graphene based LSVs with various type of junctions, where the spin relaxation time is deduced as 448-495 ps and 84 ps for tunnel junction and transparent junction, respectively [6]. The reanalysis of data using our model provides 448-495 ps and 440 ps for tunnel junctions and transparent junctions, respectively as shown in

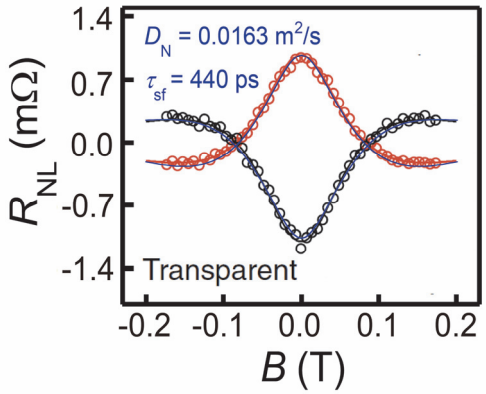

Figure 6.5: Simulated Hanle curve of a graphene based lateral spin valves with transparent junctions. Dots (experimental data) are from ref. [6] and blue lines are calculated from eqn.(2.43).

Table II: Adjusting parameters for Hanle signals for graphene based LSV with Co/Graphene junction in ref [6].

L (μm)	P_F	$P_{I(Co/Graphene)}$	τ_{sf} (ps)	D_N (cm^2/s)	$G\uparrow\downarrow$ (m$^{-2}\Omega^{-1}$)
3.00	0.40	0.0088	440	163	1.6×10^{10}

Fig.6.5 and Table II, which allows us to separate the intrinsic and extrinsic spin flip mechanisms in graphene.

6.2.4 Full width at half maximum

Spin absorption effect drastically alters the transit-time distribution. The velocity v is estimated as $v \approx L/t_{trans}$ where $t_{trans} \equiv \int_0^\infty dt\{tP(t)\} / \int_0^\infty dt\ P(t)$. Figures 6.3(a) and 6.3(b) show its speed as fast as 9.2×10^4 m/s for the Py/Ag junctions and 6.6×10^4 m/s for the Py/MgO/Ag junctions, which means the diffusion velocity depends on not only diffusion constant but also a spatial gradient in the accumulated spins. The velocity for the Py/Ag junctions is accelerated toward the detector because the spatial distribution of the electro chemical potential is strongly modified by the spin absorption while the diffusion coefficient remains constant in consistent with theoretical report [36]. Figure 6.3(c) shows v and the full width at half maximum (FWHM) of P(t) for the Py/Ag junctions normalized by those for the Py/MgO/Ag junctions. For the Py/Ag junction not only v is higher but also the FWHM is smaller than those for Py/MgO/Ag junctions, which has the more pronounced difference for short L. FWHM is the essential parameter to characterize the coherent spin precession with respect to the applied field because broad distribution of the dwell time gives rise to phase decoherence of the precessing spins [7]. The narrower FWHM for the Ohmic junction may pave the way for efficient control of spins in NM material for active spintronic devices.

6.2.5 Spin mixing conductance

Our model also enables to derive spin mixing conductance $G_{\uparrow\downarrow}$ which is one of the principal physical quantities characterizing recent novel spintronic effects such as spin pumping and insulating spin Seebeck effect [37, 38]. In the present study experimental $G_{\uparrow\downarrow}$ is shown in Table I, whereas theoretical $G_{\uparrow\downarrow}$ is roughly given by Sharvin mixing conductance $G_{\uparrow\downarrow}^{\mathrm{Sh}} = e^2k_F^2/4\pi h$, where k_F is the Fermi wave number of NM [39, 40]. It provides the value of $G_{\uparrow\downarrow}^{\mathrm{Py/Ag}} \approx G_{\uparrow\downarrow}^{\mathrm{Sh}} = 3.7 \times 10^{14}\ (\Omega\mathrm{m}^2)^{-1}$ ($k_F = 1.20 \times 10^{10}\ \mathrm{m}^{-1}$ is from [41]), which is consistent with our experimental values. The larger theoretical value may be due to a reflection of the spin current at the interface [39]. Similar behavior is reported for $G_{\uparrow\downarrow}^{\mathrm{Py/Cu}}$ of Py/Cu junctions: the experimental value of $G_{\uparrow\downarrow}^{\mathrm{Py/Cu}}$ was obtained as $3.9\times10^{14}\ (\Omega\mathrm{m}^2)^{-1}$ from Giant Mageneto Resistance (GMR) study analyzed by circuit theory on FM/NM metal hybrid device developed by Brataas *et al.* [37, 42], which is also smaller than the theoretical value $G_{\uparrow\downarrow}^{\mathrm{Sh}} = 4.8 \times 10^{14}\ (\Omega\mathrm{m}^2)^{-1}$ ($k_F = 1.36 \times 10^{10}\ \mathrm{m}^{-1}$ is from [41]). The quantitative evaluation of τ_{sf} on the change of $G_{\uparrow\downarrow}$ is as follows. For that, we estimate alternative parameter to $G_{\uparrow\downarrow}$ as $1/A_J\times\{1/(2R_I)+1/(2R_F)\}$ in the case of isotropic spin absorption (see eqn.(2.41)). In the case of LSV with Py/Ag junctions with $L = 3\ \mu\mathrm{m}$, isotropic spin absorption causes 20 % reduction of spin relaxation time. In contrast, for the graphene with transparent junction ($R_I = 285\ \Omega$) [6], since obtained $G_{\uparrow\downarrow}$ is only 4% different from the equivalent parameter $1/(2A_JR_I)$ for isotropic spin absorption, it does not give strong impact on spin absorption. This is attributed to higher junction resistance compared with Ohmic contact in metallic system. We shall note here that $G_{\uparrow\downarrow}$ obtained in this study is different from the value obtained from spin pumping by a factor of 3-6 [29, 43]. For the spin pumping measurement, the magnetization dynamics in FM resonance is used for injecting spins in the NM, and therefore the spin transport properties at the interface may be different from the Hanle effect and GMR measurements using static spin

current[8]. The transport parameters generally depend on the frequency i.e. $G=G(\omega)$. Therefore, the Hanle measurements provide us an alternative scheme to determine $G_{\uparrow\downarrow}$.

6.3. Towards coherent spin precession

6.3.1 Sample preparation and measurement condition

LSVs with Py/MgO/Ag junctions are prepared on a Si/SiO_2 substrate by means of shadow evaporation using a suspended resist mask which is patterned by *e*-beam lithography. To make the analysis simple, Py/MgO/Ag junctions are used, which prevents spin absorption. All the layers are *e*-beam deposited in an ultra-high vacuum condition of about 10^{-6} Pa. First, 20-nm-thick Py layer is obliquely deposited at a tilting angle of 45° from substrate normal. Second, the interface MgO layer is deposited at the same tilting angle of 45°. Third, 100-nm-thick Ag layer is obliquely deposited normal to the Si substrate. Finally, 3-nm-thick capping MgO layer is deposited to prevent surface contamination of the devices. After the liftoff process, the devices are annealed at 400 °C for 40 min in an N_2 (97%) + H_2 (3%) atmosphere.

The non-local measurements are carried out by a dc current source and nano-voltmeter. The bias current in the range between 200 and 400 μA is applied to the injector. The magnetic field is applied parallel to the Py wires for the spin valve measurements. For the Hanle effect measurements, the magnetic field is applied perpendicular to the Si substrate. The field direction is carefully controlled to rule out the misalignment that causes the in-plane field component that switches the magnetization of Py in the plane during the measurements.

[8] In the case of spin pumping, injected spin is in resonant state.

6.3.2 Experimental observation of genuine spin precession signal

The Hanle effect measurements were performed on LSVs by applying perpendicular magnetic fields. Figure 6.6(a) shows the modulated non-local spin signal for SLSV and DLSV. A parabolic background signal is observed for the SLSV, the origin of which is the magnetization process of FMs. When the applied magnetic field is increased above the demagnetizing field of the FM wires, the magnetizations for the injector and the detector are tilted up along the field direction, pushing the background signal up towards the value of parallel configuration for FMs. To describe the both contributions of spin precession and magnetization process, we decompose them into that of spin precession in *x*-*y* plane and that of the *z* component reflecting the magnetization process. The non-local spin signal V/I in the presence of B_Z is thus given by the sum of the above two contributions;

$$\frac{V}{I} = R_{\mathrm{S}}^{\mathrm{Hanle}}\left(\omega_{\mathrm{L}}, \mathbf{e}^{\mathrm{FM1}}\bullet\mathbf{e}_y, \mathbf{e}^{\mathrm{FM2}}\bullet\mathbf{e}_y, \mathbf{e}^{\mathrm{FM3}}\bullet\mathbf{e}_y\right) + R_{\mathrm{S}}^{\mathrm{Hanle}}\left(0, \mathbf{e}^{\mathrm{FM1}}\bullet\mathbf{e}_z, \mathbf{e}^{\mathrm{FM2}}\bullet\mathbf{e}_z, \mathbf{e}^{\mathrm{FM3}}\bullet\mathbf{e}_z\right), \quad (6.4)$$

$$\text{with} \quad R_{\mathrm{S}}^{\mathrm{Hanle}}(\omega_{\mathrm{L}}, a^{\mathrm{FM1}}, a^{\mathrm{FM2}}, a^{\mathrm{FM3}}) = \frac{1}{2}P_{\mathrm{I}}^2 R_{\mathrm{N}}\,\mathrm{Re}\left[\alpha_\omega\left(\lambda_\omega/\lambda_{\mathrm{N}}\right)\exp(-L/\lambda_\omega)\right], \quad (6.5)$$

where $\alpha_\omega = a^{\mathrm{FM2}}a^{\mathrm{FM3}}\left\{1+\exp(-2d_{12}/\lambda_\omega)\right\} - 2a^{\mathrm{FM1}}a^{\mathrm{FM3}}\exp(-d_{12}/\lambda_\omega)$, $\lambda_\omega = \lambda_{\mathrm{N}}/\sqrt{1+i\omega_{\mathrm{L}}\tau_{\mathrm{sf}}}$, $\tau_{\mathrm{sf}} = \lambda_{\mathrm{N}}^2/D_{\mathrm{N}}$ the spin relaxation time, D_{N} the diffusion constant, $\omega_{\mathrm{L}} = \gamma_e B_z$ the Larmor frequency, $\gamma_e = g\mu_{\mathrm{B}}/\hbar$ the gyromagnetic ratio, g the g-factor, μ_{B} the Bohr magneton and $a^{\mathrm{FM}i}$ is the projection of the unit vector of the magnetization of FMi $\mathbf{e}^{\mathrm{FM}i}$ on y or z-axis (see the eqns.(2.54) and (2.56), and chapter 2 for the detail). Note here that $R_{\mathrm{S}}^{\mathrm{Hanle}}\left(\omega_{\mathrm{L}}, \mathbf{e}^{\mathrm{FM1}}\bullet\mathbf{e}_y, \mathbf{e}^{\mathrm{FM2}}\bullet\mathbf{e}_y, \mathbf{e}^{\mathrm{FM3}}\bullet\mathbf{e}_y\right)$ represents the non-local resistance at the precessional frequency ω_{L}, and $R_{\mathrm{S}}^{\mathrm{Hanle}}\left(0, \mathbf{e}^{\mathrm{FM1}}\bullet\mathbf{e}_z, \mathbf{e}^{\mathrm{FM2}}\bullet\mathbf{e}_z, \mathbf{e}^{\mathrm{FM3}}\bullet\mathbf{e}_z\right)$ does that without spin precession (see chapter 2 for details). Note also that to avoid the spin absorption by FM wires, we use the Py/MgO/Ag junction in the present study [14, 19]. For SLSV, we obtain $P_{\mathrm{I}} = 0.37$ and $\lambda_{\mathrm{N}} = 1420$ nm by fitting eqn.(6.4) to the experimental data as shown in Fig. 6.6(a), which are consistent with those obtained alternatively from the L

dependence of ΔR_S in the previous section. For DLSV, the z component of the injectors is canceled out because of the opposite direction of the applied current to the junctions

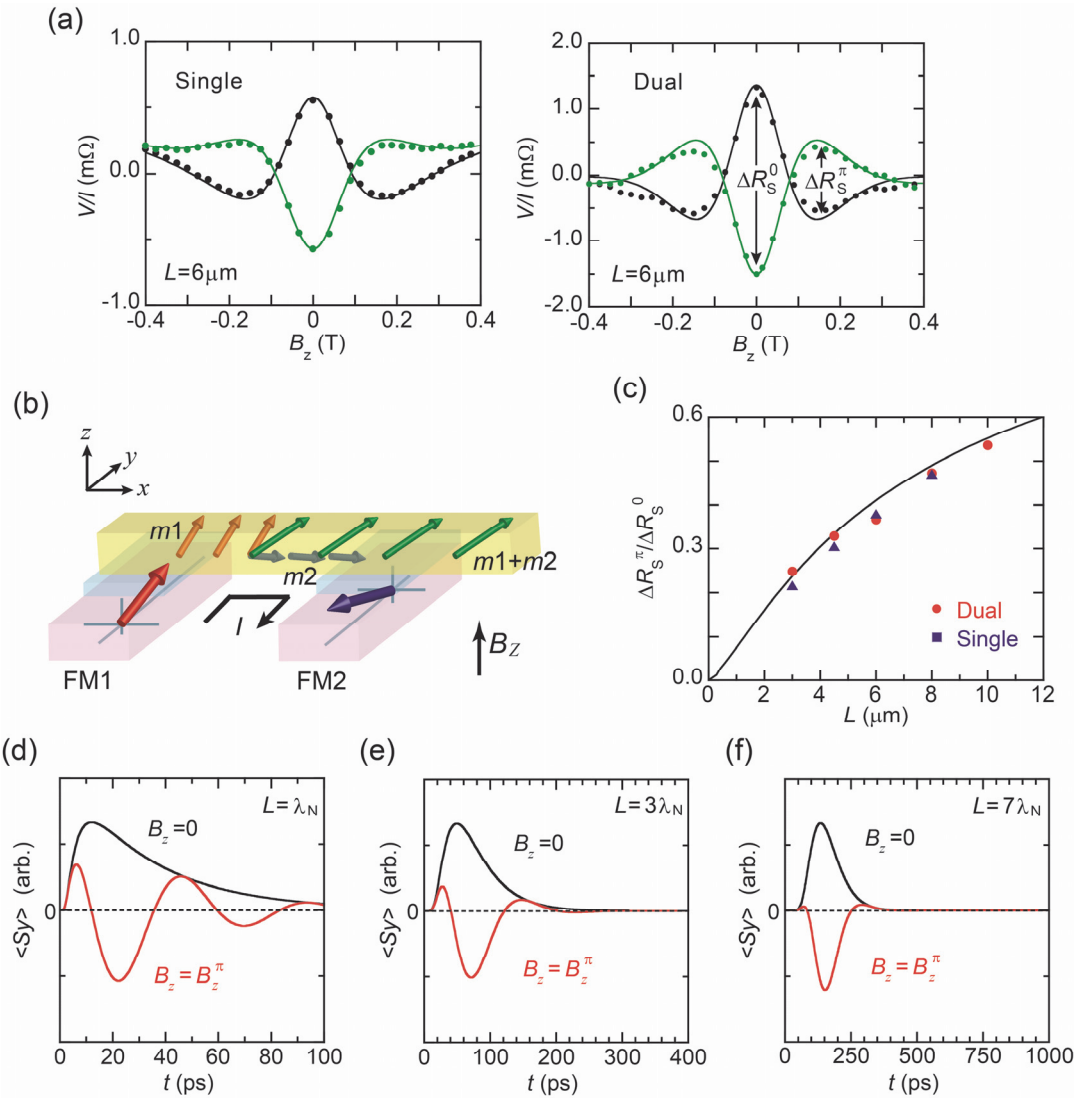

Figure 6.6: (a) Non-local spin signal modulated by spin precession as a function of perpendicular field for single and dual injector LSVs with L = 6 μm at 10 K. The solid lines are the fitting curves using eqn.(6.4). (b) Schematic diagram of magnetizations of injectors and non-equilibrium magnetization m in the Ag wire in the presence of high B_Z. In Ag, y-components of $m1$ and $m2$ are constructive but z-component of them are canceled each other out both for antiparallel and parallel magnetization configurations of the injectors. (c) Coherent parameter of the spin precession $\Delta R_S^{\pi}/\Delta R_S^{0}$ as a function of L. The solid lines are the fitting curves using eqn.(6.4) with the same parameters as used in (a). Data are corrected by taking account of the influence of magnetization process. (d)-(f) Density of y-directional spin arrived at the detector as a function of dwell time for LSVs with different L. The black and red lines represent the distribution of the dwell time in the channel without and with B_Z that causes π rotation after spins are injected, respectively.

as depicted in Fig. 6.6(b). This allows us to detect the genuine precession signal in Fig. 6.6(a).

6.3.3 Towards coherent spin precession

In the diffusive pure-spin transport, the collective spin precession decoheres due to broadening of the dwell time distribution in the channel between the injector and the detector [2]. For example, the amplitude of the spin valve signal at $B_Z = 0$ decreases after the π rotation at $B_z^{\pi} = 0.16$ T, as can be seen in Fig. 6.6(a). In order to better quantify the coherency in the collective spin precession, we define the figure of merit as the ratio $\Delta R_S^{\pi} / \Delta R_S^0$, where ΔR_S^{π} and ΔR_S^0 are the amplitude of the spin signal right after the π rotation and that in zero field right before the rotation begins, respectively. The $\Delta R_S^{\pi} / \Delta R_S^0$ increases with increasing L, and the experimental trend is well reproduced by eqn.(6.4) as shown in Fig. 6.6(c). To understand the observed trend in more detail, we employ the one-dimensional diffusion model which gives the y-component of net spin density at the detector $\langle S_y \rangle \propto 1/\sqrt{4\pi D_N t}\exp\left(-\left(L^2/4D_N t\right) - t/\tau_{sf}\right)\cos(\omega_L t)$, as a function of the dwell time t in the presence of B_z [2]. The $\langle S_y \rangle$ versus t curves for $L = \lambda_N$ with $B_z = 0$ and $B_z = B_z^{\pi}$ are shown in Fig. 6.6(d). When $B_z = 0$, $\langle S_y \rangle$ takes a broad peak structure followed by a long exponential tail. The detected spin signal in LSVs is proportional to the $\langle S_y \rangle$ integrated over time. The distribution of $< S_y >|_{B_z=0}$ gets narrower as the channel length becomes longer, of which evolution is depicted in three distribution curves under $B_z = 0$ of Figs. 6.6(d)-(f). The long exponential tail observed in Fig. 6.6(d) diminishes in proportion to $1/\sqrt{t}\exp\left(-t/\tau_{sf}\right)$. When $B_Z = B_Z^{\pi}$ is applied, the integrated value of $\langle S_y \rangle$ over time cancel for short $L \sim \lambda_N$ (Fig. 6.6(d)) whereas it does not cancel for long $L >> \lambda_N$ (Figs. 6.6(e) and (f)), indicating that the coherence of collective spin precession is well preserved for long spin transport. This trend is experimentally observed as an increase of $\Delta R_S^{\pi} / \Delta R_S^0$ from 0.21 to 0.53 with L as shown in Fig. 6.6(c).

6.3.4 Universal curve for the coherency

To better understand the coherence in collective spin precession, $t = \tau_{sf}\tilde{t}$ is substituted into the distribution function at B_Z = 0. We then obtain $< S_y > \propto 1/\sqrt{\tilde{t}}\exp\left(-(L/2\lambda_N)^2/\tilde{t} - \tilde{t}\right)$, where $\tilde{t}$ is dimensionless time. This implies that the distribution of the dwell time, i.e., coherency, is characterized only by L/λ_N and more importantly it does not depend on the kind of materials as long as their transport is diffusive. To check this idea the L/λ_N dependence of $\Delta R_S^{\pi}/\Delta R_S^{0}$ are summarized by using the data so far reported for metals, semiconductors and graphene in Fig. 6.7. Interestingly the relation between the coherence and the normalized separation shows a universal behavior and the experimental data are well reproduced by eqn.(6.4). We shall note here that the effective length L/λ_N, not the spin relaxation time, is an important parameter to manipulate the spin precession coherently in the diffusive pure-spin transport while the spin accumulation is relaxed during the diffusive transport in the channel. Therefore, the high spin injection efficiency of the Py/MgO/Ag junction and the confinement effect in the DLSV structure could offer advantages for realizing giant spin accumulation as well as the coherent spin precession along a 10 μm-long Ag wire which is much longer than the spin diffusion length. In the Hanle effect measurement of spin-polarized electron transport in a 350 μm-thick undoped single-crystal Si wafer, coherent spin precession up to 13π is reported [44]. However, the diffusion constant of the spin current is lower than that in Ag and the collector current, which is the proportional to the amount of spins in the channel, is two orders of the magnitude smaller than the detected spin current in DLSV with L = 10 μm, even though the spin-polarized current in Si is accelerated by means of electric fields.

For spintronic devices using such a long-diffusion spin current, fast spin transport may be critical. The high coherence of the spin precession over $\Delta R_S^{\pi}/\Delta R_S^{0}$ = 0.4 is reported for Al and graphene as can be seen in Fig. 6.7, however, the diffusion constant of the pure spin current is 0.003 m^2/s and 0.01 m^2/s [22, 27], respectively,

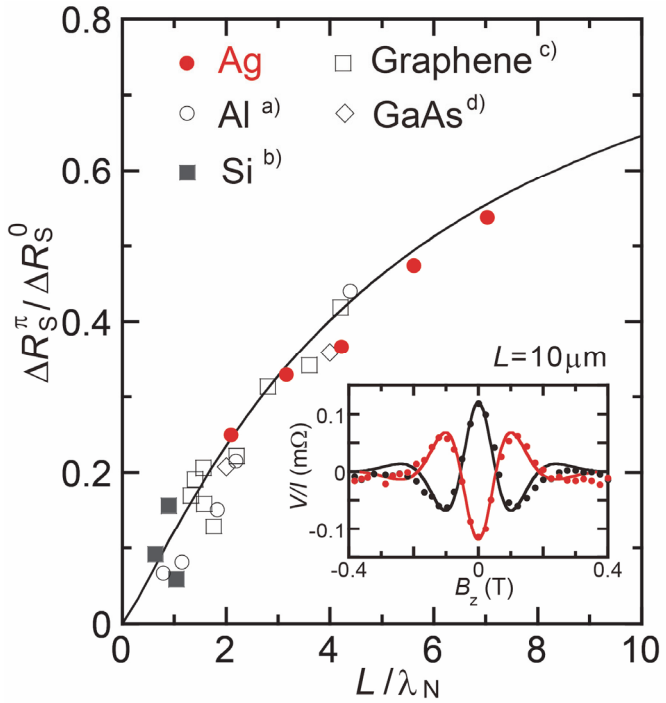

Figure 6.7: Coherency of spin precession in diffusive pure-spin current. Coherent parameter of the spin precession $\Delta R_S^{\pi}/\Delta R_S^0$ as a function of L/λ_N. The solid line is a universal curve obtained from eqn.(6.4). a) [2, 22, 23] b) [4] c) [6, 25-27] d) [3]

which is much slower than that of Ag (0.047 m^2/s). Also, the velocity of spin current in Ag is estimated to be $\sqrt{D/\tau_{sf}}$, which is as high as the drift-velocity of Si [44]. Therefore, the experimental results in this study could be useful in developing a new class of spintronic devices and the material-independent perspective for the spin precession will be beneficial for us to design pure-spin-current-based memory and transistor by using a variety of metallic and semi-conductive materials including graphenes.

6.4 Conclusion for chapter 6

In summary, we have studied the dynamic transport properties of spin current in metallic LSVs with various junctions. The effect of spin absorption on the Hanle signal was clearly observed in all the devices. The velocity of diffusive spin currents

and the transit-time distribution was successfully evaluated by applying Fourier transform to the experimental Hanle signals, resulting in excellent agreement with the empirical model in the case of the Py/MgO/Ag junctions. In contrast, we found that the transit-time distribution in LSVs with the Py/Ag junctions was strongly deviated from that expected in the empirical model and that the spins diffuse much faster than in LSVs with the Py/MgO/Ag junctions, reflecting the spatial distribution of electro chemical potential affected by the type of junctions. We have successfully formulated the Hanle effect for the LSVs with anisotropic spin absorption for the transverse and longitudinal components of the spin polarization in spin currents relative to the detector magnetization-direction, which enables to elucidate intrinsic spin transport and relaxation mechanisms in the NM. The model also provides alternative way to determine the spin mixing conductance.

In the last part, we have demonstrated that the LSVs with dual injector Py/MgO/Ag junctions enable to detect highly coherent spin precession over a distance of 10 μm with keeping spin accumulation vector in plane against out of plane magnetization process, which results in genuine signal of the in-plane precession. We also experimentally found that the better the phase coherency becomes the longer the spins travel. This tendency appears to fall on a material independent universal curve when the coherence is plotted against the reduced parameter of the injector-detector distance over spin diffusion length. This is useful for the material design of spintronics devices based on pure spin current.

References for chapter 6

[1] M. Johnson and R. H. Silsbee, *Physical Review Letters* **55**, 1790 (1985).

[2] F. Jedema, H. Heersche, A. Filip, J. Baselmans, and B. J. van Wees, *Nature* **416**, 713 (2002).

[3] X. Lou, C. Adelmann, S. A. Crooker, E. S. Garlid, J. Zhang, K. S. M. Reddy, S. D. Flexner, C. J. Palmstrøm, and P. A. Crowell, *Nature Physics* **3**, 197 (2007).

[4] T. Sasaki, T. Oikawa, T. Suzuki, M. Shiraishi, Y. Suzuki, and K. Noguchi, *Applied Physics Letters* **96**, 122101 (2010).

[5] G. Mihajlović, J. E. Pearson, S. D. Bader, and A. Hoffmann, *Physical Review Letters* **104**, 237202 (2010).

[6] W. Han, K. Pi, K. M. McCreary, Y. Li, J. J. I. Wong, A. G. Swartz, and R. K. Kawakami, *Physical Review Letters* **105**, 167202 (2010).

[7] H. Idzuchi, Y. Fukuma, and Y. Otani, *Scientific reports* **2**, 628 (2012).

[8] H.-J. Jang and I. Appelbaum, *Physical Review Letters* **103**, 117202 (2009).

[9] B. Huang and I. Appelbaum, *Physical Review B* **82**, 241202 (2010).

[10] C. P. Weber, N. Gedik, J. E. Moore, J. Orenstein, J. Stephens, and D. D. Awschalom, *Nature* **437**, 1330 (2005).

[11] L. Yang, J. D. Koralek, J. Orenstein, D. R. Tibbetts, J. L. Reno, and M. P. Lilly, *Nature Physics* **8**, 153 (2011).

[12] A. T. Filip, B. H. Hoving, F. J. Jedema, B. J. van Wees, B. Dutta, and S. Borghs, *Physical Review B* **62**, 9996 (2000).

[13] H. Idzuchi, Y. Fukuma, L. Wang, and Y. Otani, *Applied Physics Letters* **101**, 022415 (2012).

[14] Y. Fukuma, L. Wang, H. Idzuchi, and Y. Otani, *Applied Physics Letters* **97**, 012507 (2010).

[15] S. O. Valenzuela and M. Tinkham, *Applied Physics Letters* **85**, 5914 (2004).

[16] S. Garzon, I. Žutić, and R. Webb, *Physical Review Letters* **94**, 176601 (2005).

[17] A. Vogel, J. Wulfhorst, and G. Meier, *Applied Physics Letters* **94**, 122510 (2009).

[18] X. J. Wang, H. Zou, L. E. Ocola, R. Divan, and Y. Ji, *Journal of Applied Physics* **105**, 093907 (2009).

[19] Y. Fukuma, L. Wang, H. Idzuchi, S. Takahashi, S. Maekawa, and Y. Otani, *Nat Mater* **10**, 527 (2011).

[20] A. B. a. E. Yu, *Journal of Physics C: Solid State Physics* **17**, 6039 (1984).

[21] S. Datta and B. Das, *Applied Physics Letters* **56**, 665 (1990).

[22] S. O. Valenzuela and M. Tinkham, *Nature* **442**, 176 (2006).

[23] A. van Staa, J. Wulfhorst, A. Vogel, U. Merkt, and G. Meier, *Physical Review B* **77**, 214416 (2008).

[24] O. van't Erve, C. Awo-Affouda, A. T. Hanbicki, C. H. Li, P. E. Thompson, and B. T. Jonker, *Electron Devices, IEEE Transactions on* **56**, 2343 (2009).

[25] N. Tombros, C. Jozsa, M. Popinciuc, H. T. Jonkman, and B. J. van Wees, *Nature* **448**, 571 (2007).
[26] M. Popinciuc, C. Józsa, P. J. Zomer, N. Tombros, A. Veligura, H. T. Jonkman, and B. J. van Wees, *Physical Review B* **80**, 214427 (2009).
[27] T. Maassen, F. K. Dejene, M. H. D. Guimarães, C. Józsa, and B. J. van Wees, *Physical Review B* **83**, 115410 (2011).
[28] S. Takahashi and S. Maekawa, *Physical Review B* **67**, 052409 (2003).
[29] A. Ghosh, S. Auffret, U. Ebels, and W. E. Bailey, *Physical Review Letters* **109**, 127202 (2012).
[30] A. Brataas, Y. V. Nazarov, and G. E. Bauer, *The European Physical Journal B-Condensed Matter and Complex Systems* **22**, 99 (2001).
[31] M. Stiles and A. Zangwill, *Physical Review B* **66**, 014407 (2002).
[32] J. Bass and W. P. Pratt, *Journal of Physics: Condensed Matter* **19**, 183201 (2007).
[33] S. Dubois, L. Piraux, J. M. George, K. Ounadjela, J. L. Duvail, and A. Fert, *Physical Review B* **60**, 477 (1999).
[34] D. Papaconstantopoulos, *Handbook of the band structure of elemental solids* (Plenum Press New York, 1986).
[35] P. Monod and S. Schultz, *Journal de Physique* **43**, 393 (1982).
[36] S. Hershfield and H. L. Zhao, *Physical Review B* **56**, 3296 (1997).
[37] Y. Tserkovnyak, A. Brataas, and G. Bauer, *Physical Review B* **66**, 224403 (2002).
[38] J. Xiao, G. E. W. Bauer, K.-c. Uchida, E. Saitoh, and S. Maekawa, *Physical Review B* **81**, 214418 (2010).
[39] J. Barnaś, A. Fert, M. Gmitra, I. Weymann, and V. Dugaev, *Physical Review B* **72**, 024426 (2005).
[40] A. Kovalev, A. Brataas, and G. Bauer, *Physical Review B* **66**, 224424 (2002).
[41] N. W. Ashcroft and N. D. Mermin, *Solid state physics.* (Brooks Cole, United States, 1976), p.^pp. 5.
[42] G. Bauer, Y. Tserkovnyak, D. Huertas-Hernando, and A. Brataas, *Physical Review B* **67**, 094421 (2003).
[43] F. D. Czeschka *et al.*, *Physical Review Letters* **107**, 046601 (2011).
[44] B. Huang, D. Monsma, and I. Appelbaum, *Physical Review Letters* **99**, 177209 (2007).

Summary

This thesis describes a series of experiment aimed at the understanding of the static and dynamic properties of pure spin current by using lateral spin transport with non-local spin injection techniques.

The major results of the thesis are as follows:

1. The hundred-fold enhancement of the spin accumulation was realized by non-local spin injection in lateral spin valves (LSVs) with $Ni_{80}Fe_{20}$(Permalloy, Py) /MgO/Ag and $Co_{50}Fe_{50}$/MgO/Ag junctions. Underlying physics is understood as a (spin) resistance (conductance) mismatch (Chapter 2 and 4).
2. Spin relaxation mechanism in non-magnetic Ag and Mg nanowires were quantitatively examined by evaluating its spin diffusion properties. Intrinsic properties was deduced by temperature variation of spin relaxation time and momentum relaxation time. The strength of spin relaxation were explained by the effects of the spin-orbit interaction and the electronic structure (Chapter 5).
3. The model to characterize dynamic spin transport properties were established, which quantitatively explains the impact of spin absorption on the collective spin precession (Hanle effect) and enables to derive intrinsic spin relaxation time of non-magnetic nanowires (Chapter 2 and Chapter 6).
4. Long-distance 10 μm collective spin precession was observed in dual injector lateral spin valve (DLSV). The coherence of the spin precession, defined as the ratio of the spin signal after the π rotation and without rotation, was as high as

0.5 for 10 μm spin precession. The coherence of the spin precession was summarized in various non-magnetic material including metals and semiconductors such as silicon and graphene by using the separation normalized by spin diffusion length (Chapter 6).

The enhancement of the spin accumulation in LSVs with Py/Ag junctions and Py/MgO/Ag junctions. The effect of the junction for the generation of spin current was systematically studied. The spin signal increases with an increase of the MgO thickness and the interface resistance, in which behavior is understood as a spin-resistance mismatch. The experimental results are analyzed in detail with the spin diffusion model. The origin of the enhancement of the spin accumulation is found as follows. (1) The injector Py/MgO/Ag junction prevents back-flow of spin current, which enables efficient spin injection. (2) The detector Py/MgO/Ag junction prevents the decrease of the spin accumulation caused by spin absorption, which enables "efficient" detection of the spin accumulation. The experimental result shows that the junction resistance of around the spin-resistance of Ag is enough for efficient spin injection, which is compatible with higher current application than one for the conventional high resistance magnetic tunnel junctions. It results in the hundred-fold spin accumulation signal $\Delta V = 225$ μV.

The enhancement of spin accumulation in dual-injection DLSVs. The device structure for efficient generation of spin current was optimized. Dual spin injection scheme enhanced spin accumulation by a factor of 3.2 with Py/MgO/Ag(100-nm-thick) junctions. We found that the enhancement reaches up to 4 in the present device structure with small

injectors' separation and without spin absorption. Spin accumulation shows a maximum among the several magnetic configurations when the injectors' magnetization-configuration is antiparallel. Large spin signals of 233 mΩ and 480 mΩ are observed for DLSVs with Py/MgO/Ag and CoFe/MgO/Ag, respectively. The spin polarization of the CoFe/MgO/Ag junctions is found as high as 0.52. The efficient generation of the pure spin current $I_S/I_C = 0.58$ is realized. Although the number of injection electrodes is increased in a lateral geometry, the spin absorption effect for Ohmic Py/Ag junctions prevents the enhancement of the spin accumulation in the Ag nanowire. Analysis based on one-dimensional spin diffusion model revealed that the spin absorption effect in the middle Py/Ag junction strongly suppress the enhancement of the spin accumulation in DLSVs with Ohmic junctions.

The spin diffusion characteristics in LSVs with Mg nanowire. Clear non-local and local spin valve signals are observed for a LSV with Py/Mg junctions. The amplitude of the local spin valve signal is 2.4 times larger than that of the non-local spin valve signal, which assure that one-dimensional spin diffusion model is applicable to explain the observed spin valve behaviors in the Py/Mg devices. The amplitude of the spin signal is relatively large among LSVs with transparent Ohmic junctions. The spin diffusion length of Mg is found to be 720 nm at $T = 10$ K and 230 nm at RT from the measurement of the spin valve signal as a function of the separation L. The obtained spin diffusion lengths for Mg are not much longer than those for Al, Cu and Ag whereas the obtained spin-flip probability, ratio of spin relaxation time and momentum relaxation time, is a little smaller than those of Cu and Ag. The spin-flip probability is larger compared to one in the material

with similar spin-orbit strength, which is consistent with the theoretical prediction by Fabian and Das Sarma: possibly because of the enhanced spin relaxation near the special points for polyvalent metals in momentum space called as spin–hot-spots.

The spin relaxation mechanism in Ag nanowires. The spin-flip probability caused by phonon and impurity scatterings is precisely determined. The surface spin scattering, which hampered quantitative analysis in previous reports, is well suppressed in Ag nanowire by an MgO capping layer. The temperature dependence of the spin relaxation times due to phonon scattering for the Ag nanowire is well fitted to the Bloch-Grüneisen formula. The fitting curve is in good agreement with the reported spin relaxation times of Ag foils used in the conduction electron spin resonance measurement, which reflects intrinsic feature of Ag. Thus the spin relaxation mechanism of Ag nanowire is well explained in the framework of the conventional Elliott-Yafet model. The experiment data in the present study fall on to the universal curve for monovalent metals in the revised Monod-Beuneu scaling. These allow us to determine the spin relaxation time for phonon scattering in the monovalent metals at any temperatures and to understand the spin-flip mechanism in the non-magnetic nanowires.

The dynamic transport properties of spin current in metallic LSVs with various junctions. The effect of spin absorption on the Hanle signal was clearly observed. The velocity of diffusive spin currents and the transit-time distribution was successfully characterized by applying Fourier transform to the experimental Hanle signals, resulting in excellent agreement with the empirical model in the case of Py/MgO/Ag junctions. In

contrast, we found that the transit-time distribution in LSVs with Py/Ag junctions was strongly deviated from that expected in the empirical model and that the spins diffuse much faster than in LSVs with Py/MgO/Ag junctions, reflecting the spatial distribution of electro chemical potential affected by the type of junctions. We have successfully formulated the Hanle effect for the LSVs with anisotropic spin absorption for the transverse and longitudinal components of the spin polarization in spin currents relative to the detector magnetization-direction, which enables to separate intrinsic spin transport parameters from spin absorption effect.

Long-distance and highly coherent spin precession. Highly coherent spin precession over a distance of 10 μm was demonstrated. DLSV scheme cancels out the out-of-plane component of the spin accumulation from each injector, which suppresses the background of Hanle signal. We also experimentally found that the better the phase coherency becomes the longer the spins travel. This tendency appears to fall on a material independent universal curve when the coherence is plotted against the reduced parameter of the injector-detector distance over spin diffusion length.

This thesis presents a systematic study on the spin dependent transport in the mesoscopic metallic devices. The thesis consists of three complimentary studies, the enhancement of the spin accumulation (the effect of the junction and device structure), the spin relaxation mechanism (intrinsic properties: phonon contribution and the effect of the electronic structure), and the collective spin precession (the characterization of the spin transport properties and the modulation of spin current), which are deeply related each

other. The in-depth understandings of lateral spin transport could be useful for developing new spintronics devices based on the pure spin current.

Publications

- H. Idzuchi, Y. Fukuma, S. Takahashi, S. Maekawa and Y. Otani,
  Effect of anisotropic spin absorption on the Hanle effect in lateral spin valves.
  Phys. Rev. B (Rapid), accepted
- K. Fujiwara, Y. Fukuma, J. Matsuno, H. Idzuchi, Y. Niimi, Y. Otani , and H. Takagi.
  5d iridium oxide as a material for spin-current detection.
  Nat. Commun. **4**, 2893-1~6 (2013).
- H. Idzuchi, S. Karube, Y. Fukuma, T. Aoki, and Y. Otani.
  Impact of interface properties on spin accumulation in dual-injection lateral spin valves.
  Appl. Phys. Lett. **103**, 162403-1~4 (2013).
- Y. P. Liu, H. Idzuchi, Y. Fukuma, O. Rousseau, Y. Otani, and W. S. Lew.
  Spin injection properties in trilayer graphene lateral spin valves.
  Appl. Phys. Lett. **102**, 033105-1~4 (2013).
- Y. Niimi, D. H. Wei, H. Idzuchi, T. Wakamura, T. Kato, and Y. Otani.
  Experimental Verification of Comparability between Spin-Orbit and Spin-Diffusion Lengths.
  Phys. Rev. Lett. **110**, 016805-1~5 (2013).
- H. Idzuchi, Y. Fukuma and Y. Otani.
  Towards coherent spin precession in pure-spin current.
  Sci. Rep. **2**, 628-1~5 (2012).
- H. Idzuchi, Y. Fukuma, L. Wang, and Y. Otani.
  Spin relaxation mechanism in silver nanowires covered with MgO protection layer.
  Appl. Phys. Lett. **101**, 022415-1~4 (2012).

- J. Tarun, S. Huang, Y. Fukuma, H. Idzuchi Y. Otani, N. Fukata, K. Ishibashi, and S. Oda.
  Temperature Evolution of Spin-Polarized Electron Tunneling in Silicon Nanowire–Permalloy Lateral Spin Valve System.
  Appl. Phys. Exp. **5**, 045001-1~3(2012).
- L. Wang, Y. Fukuma, H. Idzuchi and Y. Otani.
  Effect of Annealing on Interfacial Spin Polarization and Resistance in Permalloy/MgO/Ag Lateral Spin Valves.
  Appl. Phys. Exp. **4**, 093004-1~3(2011).
- H. Idzuchi, Y. Fukuma, L. Wang and Y. Otani.
  Spin Injection Into Magnesium Nanowire.
  IEEE. Trans. on Magnetics **47**, 1545~1548(2011).
- Y. Fukuma, L. Wang, H. Idzuchi, S. Takahashi, S. Maekawa and Y. Otani,
  Giant enhancement of spin accumulation and long-distance spin precession in metallic lateral spin valves.
  Nature Materials **10**, 527~531(2011).
- J. Tarun, S. Huang, Y. Fukuma, H. Idzuchi, Y. Otani, N. Fukata, K. Ishibashi, and S. Oda.
  Demonstration of spin valve effects in silicon nanowires.
  J. Appl. Phys. **109**, 07C508-1~3(2011).
- L. Wang, Y. Fukuma, H. Idzuchi and Y. Otani.
  Efficient spin injection into nonmagnetic metals through low-resistance MgO.
  J. Appl. Phys. **109**, 07C506-1~3(2011).
- H. Idzuchi, Y. Fukuma, L. Wang and Y. Otani.
  Spin Diffusion Characteristics in Magnesium Nanowires.
  Appl. Phys. Exp. **3**, 063002-1~3(2010).
- Y. Fukuma, L. Wang, H. Idzuchi and Y. Otani.
  Enhanced spin accumulation obtained by inserting low-resistance MgO interface in

metallic lateral spin valves
Appl. Phys. Lett. **97**, 012507-1~3(2010).

- Y. Fukuma, L. Wang, H. Idzuchi and Y. Otani.
  Enhanced spin accumulation obtained by inserting low-resistance MgO interface in metallic lateral spin valves
  Appl. Phys. Lett. **97**, 012507-1~3(2010).
- T. Hirahara, T. Komorida, Y. Gu, F. Nakamura, H. Idzuchi, H. Morikawa, and S. Hasegawa.
  Insulating conduction in Sn/Si (111): Possibility of a Mott insulating ground state and metallization/localization induced by carrier doping.
  Phys. Rev. B **80**, 235419 (2009).

Acknowledgements

I would like to acknowledge all the people who gave me the insightful, critical and helpful comments and discussions, collaborate with me, helped the experiment, and encouraged me. This theis could not be made possible without the help of many people.

I would like to express my gratitude to Yoshichika Otani in Institute for Solid State Physics in the University of Tokyo, my supervisor in PhD, for giving me chance to study the state of the art in his group, discussing frankly and guiding me to find exciting research and scientific interest. I also greatly appreciate Albert Fert in Unité Mixte de Physique CNRS/Thales and Sadamichi Maekawa in Japan Atomic Energy Agency for their insightful suggestions and discussions based on their immense knowledge. I greatly appreciate Yuji C. Sasaki in Graduate School of Frontier Sciences, the University of Tokyo and Satoru Nakatsuji in Institute for Solid State Physics in the University of Tokyo for their suggestions which are not biased from the specific view in the community in spintronics.

I also greatly appreciate Yasuhiro Fukuma in Frontier Research Academy for Young Researchers, Kyushu Institute of Technology for guiding our research by his enthusiasm and for practical-minded suggestions on my everyday research life. Special thanks must go to Akira Tonomura in Hitachi Ltd., for giving me *his passion*. His encouragement greatly supported my research. I also want to thank Saburo Takahashi in Institute for Materials Research in Tohoku University for the helpful discussions about the analysis of Hanle effect.

I also would like to thank Yasuhiro Niimi for discussions about the various spin transport phenomena and comments on e.g. my presentation and the way to proceed my

research. I am so much indebted to Kohei Fujiwara for his kind guidance of my research in the initial stage. It was a very pleasure to work with you. Many thanks to Keiichi Yanagisawa (柳沢　佳一　様) for his consultations of micro fabrication and his fast response. I would like to thank Hajime Kohinata for his careful consultations on e-beam lithography and SEM techniques. I also thank to Ryoji Itoh, Kazuhiko Shihoyama and Chiari Itonaga for the help to use a clean room.

I am grateful to Tsuyoshi Matsuda, Keiichi Yanagisawa (柳沢　圭一　様) for their patient collaborations on TEM observation. I also thank Daisuke Shindo, Hyun Soon Park, Toshiaki Tanigaki, Kimi Matsuyama, Manabu Shirai, and Yoshimasa A. Ono for their patient collaborations. I also want to thank Kouta Kondou, Motoi Kimata, and Satoshi Sugimoto for the helpful discussions and the measurements on the magnetization dynamics. I would like to thank Hikota Akimoto for his kind consultations of my research life in the latter of my PhD study. I also would like to thank Susumu Shimoda and Kei Sunouchi for their consultations on the engineering. I thank Keiji Ohno for the help of the equipment in the clean room. I would like to thank Le Wang for the kind teaching of various experimental techniques related to LSVs. I would like to thank Shinya Kasai for the helpful discussions of the detection techniques. I thank Jobu Matsuno for the frank discussions from his wide perspective view. I also would like to thank Xiaofeng Jin and Axel Hofmann for their helpful comments on the analysis and interpretations of Hanle effect. I thank Hiroki Nanaumi for the discussions on the experimental techniques of the Hanle effect. I also thank Tatsuya Aoki for giving the *trigger* of the experiment on $Co_{50}Fe_{50}$ alloys. I also thank Kohei Ohnishi for his careful guidance of research life and *quick* response. I also would like to thank Machie Kaito and Noriko Iizuka for the assistance of the sample

fabrication and characterization. I thank Liu Yanping for the experience of graphene related spintronics. I thank Jean Tarun for the collaboration of Si nanowires. I thank Daishi Inoue and Tomoka Kikitsu for the characterization by the electron micrography. I thank Shutaro Karube for the help of sample fabrications. I thank Ryo Anami for magnetization measurements. I would like to thank Prof. Marrows for the helpful comments on the presentation. Special thanks go to Milan Agrawal for the exciting collaborations. It was a very pleasure to work with you, and I wish good luck with the research.

For all the paper work I thank our group secretaries Junko Kawamura, Michiko Ishinabe, and Hiromi Oshimori. I also thank secretaries in University of Tokyo Yukiko Tan, Sachie Iimura, Makiko Matsuzaki, Masako Kotake and Chieko Kobayashi for the paper work.

It is a pleasure to thank to all other (former) group members. I thank Dahai Wei, Long You, Gaier Oksana, Olivier Rousseau, Misako Morota and Hiromi Sakata for the suggestions on the research life. I also thank Taro Wakamura, Yohei Kawanishi, Hiroaki Fujimori, Hiroshi Suzuki, Norinobu Hasegawa for stimulating my research. For the pleasant atmosphere in the office I would like to thank Daisuke Nozaki, Yasutomo Omori, and Daichi Kodama.

Finally, I thank my family and my brother Akira for all their understanding and support.

Thank you.

Hiroshi Idzuchi

Wako, Japan

February 2014.

謝辞 (Acknowledgements)

本研究を進めるに当り多くの方々のご指導、ご協力、ご支援をい頂きました。この場を借りて厚く御礼申し上げます。

東京大学物性研究所 大谷義近教授には、最先端の環境において研究をする機会を与えて下さったこと、常に気さくに議論をして頂き、筆者にない科学的視点からの様々な気づきをくださったことに深く感謝致します。日本原子力研究開発機構 前川禎通 教授、パリ南大学 Prof. Albert Fert には短時間の議論においても常に本質を衝く質問を頂き、大変勉強になりました。深謝いたします。東京大学新領域創成科学研究科物質系専攻 佐々木 裕次 教授、東京大学物性研究所 中辻知 准教授には、研究をまとめるにあたり分野の枠にとらわれない指摘を頂きました。深謝いたします。

九州工業大学 若手研究者フロンティア研究アカデミー 福間康裕 准教授には、研究テーマをすすめるに当り、日々どのように考えて研究するかは身をもって教えて頂きました。感謝いたします。日立製作所　外村 彰 フェロー には、その実験に対する徹底した考え方を実際の研究に基づいて教えて頂くとともに、サンプル作製の困難な時期にも激励を頂き、大変励みになりました。東北大学金属研究所 高橋三郎 助教 にはHanle効果の解析に関する詳細な議論を頂きました。東京大学物性研究所 新見康洋 助教には、スピン流諸現象の議論、研究の進め方や研究発表の仕方を初めとして様々な助言を頂きました。理化学研究所 藤原宏平 基礎科学特別研究員（現大阪大学産業科学研究所 助教）には、研究の初期の段階において筆者に実験のすすめ方や研究発表の方法などご指導頂くとともに、メンターとして様々な相談にのって頂きました。理化学研究所 研究技術開発支援チーム

柳沢 佳一 様には蒸着装置、加工装置の使用方法に関して丁寧に教えて頂くと共に、迅速に対応していただきました。理化学研究所 創発物性科学研究支援チーム 小日向一 様には電子ビーム露光装置、SEMに関して非常に丁寧に教えていただきました。同 伊藤 良二 様、四方山 和彦 様、糸永 千亜里 様にはクリーンルームの使用に際してお世話になりました。

科学技術振興機構(JST) 松田強 技術コーディネーター、理化学研究所量子現象観測技術研究チーム 柳沢 圭一 様、同創発現象観測技術研究チーム進藤 大輔 チームリーダー、朴賢洵 上級研究員、谷垣俊明 協力研究員、会沢 真二 様、日立製作所 松山 喜美 プロジェクト員、 白井 学 プロジェクト員、科学技術振興機構(JST) 小野 義正 技術コーディネーターには電子線ホログラム観測に関して大変丁寧かつ根気よく対応していただきました。理化学研究所量子ナノ磁性研究チーム 近藤 浩太 研究員、東京大学物性研究所 木俣 基 助教には磁化ダイナミクスを用いた測定に関してご教授、ご協力頂きました。理化学研究所創発物性科学研究支援チーム 秋元彦太 チームリーダーには研究の後期の段階においてメンターとして様々な相談に対応して頂きました。理化学研究所先端工作支援チーム 霜田 進 様、 洲之内 啓 様には研究工作において迅速に対応していただきました。理化学研究所 河野低温研究室 大野圭司 専任研究員にはワイヤーボンダーの使用に関して丁寧にご協力いただきました。理化学研究所量子ナノ磁性研究チーム Le Wang 様 には実験方法について丁寧に教えていただきました。同 Yanpin Liu 様には Grapheneへのスピン注入素子の作製、評価に関して一緒に実験をさせて頂きました。物質材料研究機構 葛西伸哉 主任研究員にはスピントロニクスに関しての幅広い見解と具体的な測定手法をご教授頂きました。理化学研究所 高木磁性研究室 松野 専任研究員 (現強相関界面研究グループ)には幅広い視点からの議

論をいただきました。Fudan University Prof. Xiaofeng Jin、Argonne National Laboratory Dr. Axel Hoffman にはHanle効果の解析に関して有益なコメントを頂きました。東京大学物性研究所 七海裕貴 様にはHanle効果の実験方法に関して議論頂き、同 青木達也博士 にはCoFe合金を用いた実験を進めるきっかけを作って頂きました。理化学研究所量子ナノ磁性研究チーム 皆藤真智恵 様、飯塚紀子 様にはサンプル作製及びサンプル評価に関して、理化学研究所石橋極微デバイス工学研究チームJean Tarun博士にはSi nanowireへのスピン注入実験に関して一緒に実験をさせて頂いたことを感謝します。理化学研究所 物質評価チーム井ノ上大嗣様、喜々津智郁 様には透過電子顕微鏡観察において丁寧に対応していただきました。Technische Universität Kaiserslautern Burkard Hillebrands Lab. Mr. Milan Agrawal にはBLSとスピン流の実験に関して一緒に実験をさせて頂いたことを感謝します。

また、理化学研究所量子ナノ磁性研究チーム アシスタント 石鍋道子 様、押森広美 様、東京大学物性研究所 秘書 川村順子 様には充実した研究生活を送る上で様々なサポートをしていただきました。東京大学新領域創成科学研究科物質系専攻教務の丹由紀子 様、飯村祐枝様、松崎真紀子 様、同研究科教務の小竹真佐子 様、小林智恵子 様には事務でお世話になりました。上で挙げきれなかった研究室のメンバーの、研究員の魏大海 博士、Dr. Long You、Gaier Oksana 博士、Dr. Rousseau、先輩の諸田美砂子 様、大西紘平 様、坂田裕美 様には研究室生活全般について助言いただきました。同期の杉本聡志 君、後輩の川西庸平 君、若村太郎 君、鈴木裕 君、藤森啓晃 君、軽部修太郎 君、長谷川徳信 君は研究を刺激してくださいました。

最後に、研究生活をサポートしてくれた家族に感謝しています。

List of abbreviations

B-G	Bloch-Grüneisen
CESR	Conduction electron spin resonance
DLSV	Dual injector lateral spin valve
E-Y	Elliott-Yafet
FM	Ferromagnetic/ferromagnet
FWHM	Full width at half maximum
GMR	Giant Mageneto Resistance
IPA	Isopropyl alcohol
LSV	Lateral spin valve
MMA	Methyl-methacrylate
NM	Non-magnetic/non-magnet
PMMA	polymethyl methacrylate
Py	Permalloy, $Ni_{80}Fe_{20}$
RT	Room temperature
SEM	Scanning electron microscopy
SOI	Spin-orbit interaction

Index of symbols

Symbol	*Definition*	*Page*
A_F	Cross-sectional area of ferro-magnet	12
A_J	Cross-sectional area of junction	62
A_N	Cross-sectional area of non-magnet	63
a_1	Coefficients of spin accumulation in NM in spin diffusion equation	12
a^{FMi}	Projection of the unit vector of the magnetization of FM*i*	103
α	Enhancement factor of DLSV compared to SLSV	21
α_B	Coefficient for B-G theory	83
$B_Z^{\pm\pi/2}$	Magnetic field for collective $\pm\pi/2$ spin precession	24, 93
B_Z^{π}	Magnetic field for collective π spin precession	24
b_1	Coefficients of spin accumulation in FM in spin diffusion equation	12
C	Material constant for revised Monod-Beuneu scaling	86

$\cos\theta_{yj}$	Projection of magnetization direction of j-th magnet on y-direction	32
D	Diffusion constant	10
D_{N}	Diffusion constant for NM	24
D_{σ}	Diffusion constant for σ channel	9
d_{12}	Separation of FM1 injector and FM2 injector	19
ΔE	Separation to the nearest band with the same transformation properties	33, 84
ΔR_{S}	Spin signal	16
$\Delta R_{\mathrm{F}i}$	Spin signal due to the magnetization reversal of FMi	60
$\Delta R_{\_\mathrm{DLSV}}$	Spin signal for DLSV	62
$\Delta R_{\_\mathrm{SLSV}}$	Spin signal for SLSV	62
ΔV_{S}, ΔV	Spin-valve voltage	ii
δn_{σ}	Non-equilibrium electron density	9
$\delta\mu$	Spin accumulation	9
$\delta\mu_{\mathrm{Ag}}$	Spin accumulation of Ag	56
$\delta\mu_{\mathrm{F}}$	Electro chemical potential for FM	12
$\delta\mu_{\mathrm{N}}$	Electro chemical potential for NM	12
$\delta\mu_{\parallel}$	Longitudinal spin accumulation in NM	96
E	Energy	2
E	Electrical field	9
E_{D}	Demagnetization energy	29
$\mathbf{e}^{\mathrm{FM}i}$	Unit vector of the magnetization of FMi	20
ε	Spin relaxation ratio	ii
ε_{F}	Fermi energy	2
$\varepsilon_{\mathrm{imp}}$	Spin-flip probability for impurity scatterings	77
$\varepsilon_{\mathrm{ph}}$	Spin-flip probability for phonon scatterings	77
$\varepsilon_{\mathrm{surf}}$	Spin-flip probability for surface scatterings	85
ϕ_e	Electrical potential	9
ϕ	Angle between I_0 and positive direction of H	30
g	g-factor	86
$G_{\mathrm{I}i}$	Interface conductance of i-th junction	16
$G_{\mathrm{I}j}{}^{\sigma}$	Interface conductance of j-th junction for spin channel σ	16
$G_{\uparrow\downarrow,\,k}$	Real part of spin mixing conductance of k-th junction	27
$G_{\uparrow\downarrow}^{\mathrm{Sh}}$	Sharvin mixing conductance	101
γ_{e}	Gyromagnetic ratio	24

H	Magnetic field	30
$\hbar$	Planck constant	24
$\mathcal{H}$	Hamiltonian	33
I, I_C	Applied current	9
$I\uparrow$, $I\downarrow$	Current for $\uparrow$ channel, for $\downarrow$ channel	8
$I_{Jk}^{x(y),\sigma}$	Current with the polarization in $x(y)$ direction	27
$I_{S,Jk}^{y}$	Transverse spin current	27
I_m	Injected spin current	26
I_S	Spin current	11
$I_{Si}^{\parallel}$	Longitudinal component of spin current of i-th junction	96
$I_{Si}^{\perp}$	Transverse component of spin current of i-th junction	96
I_0	Intensity of the magnetization	20
$j_{\tilde{S}}$	Spin current density	10
$\dot{j}_s$	Complex representation of spin current density	10
j_σ	Current density for σ channel	9
K	Coefficient for B-G theory	83
k_F	Fermi wave number	101
L	Separation between FM injector to FM detector	16
λ_{SOI}	Spin-orbit splitting	34
λ_{sf}	Spin diffusion length	10
λ_F	Spin diffusion length of FM	12
λ_N	Spin diffusion length of NM	12
λ_ω	Complex spin diffusion length	25
$\bar{\lambda}_\omega$	Normalized complex spin diffusion length	25
$\delta\tilde{\mu}_{F,k}$	Complex spin accumulation of k-th FM	27
$\delta\tilde{\mu}_N$	Complex spin accumulation	26
$\bar{\mu}_N$	Spin independent part of electro chemical potential of NM	19
μ_σ	Electro chemical potential for σ channel	9
μ_B	Bohr magneton	24
m	Non-equilibrium magnetization	104
mi	Non-equilibrium magnetization from the spin injection of i-th junction	104
$\tilde{m}$	Complex representation of non-equilibrium magnetization	26
$\mathbf{m}_N$	Non-equilibrium magnetization	25
m_e	Electron mass	83

m_x	x-component of non-equilibrium magnetization	26
m_y	y-component of non-equilibrium magnetization	26
n	Free electron density	83
Ni	Demagnetization factor of FMi	30
$N\uparrow$, $N\downarrow$	Spin-dependent density of states	3
N_σ	Diffusion constant for σ channel	9
$N(\varepsilon_F)$	Density of states at the Fermi energy	76
P_{eff}	Effective spin polarization	13
$P_{em}(t)$	Empirical transit-time distribution	95
P_F	Spin polarization of FM	8
P_{Fj}	Spin polarization of j-th FM	16
P_I	Spin polarization of the junction	53
P_{Ij}	Spin polarization of j-th junction	16
P_{Py}	Spin polarization of Py	53
$P(t)$	Transit-time distribution	23
θ_{12}	Angle between the magnetization directions of FM1 and FM2	20
θ_{23}	Angle between the magnetization directions of FM2 and FM3	20
R_F	Spin-resistance of FM	11
R_{Fj}	Spin-resistance of of j-th FM	16
R_N	Spin-resistance of NM	11
R_I	Interface resistance	22
R_{IA}	Areal resistance	49
R_{Ij}	Junction resistance of j-th junction	16
R_N	Spin-resistance of NM	53
R_S^{Hanle}	(Hanle signal)	31
R_S^0	Amplitude of spin signal before the rotation begins	105
R_S^π	Amplitude of spin signal after the π rotation	105
r_{Fj}	Normalized spin-resistance of j-th FM	20
r_{Ij}	Normalized resistance of j-th interface	20
r^*	Spin-resistance mismatch factor	22
ρ, ρ_N	Resistivity, rsistivity of NM	11
ρ_{ph}	Resistivity due to phonon scatterings	83
$\rho_{\Theta_D}^{ph}$	Resistivity for phonon scatterings at the Debye temperature	84
S	Spin density	23
$S(L,t)$	Spin density at the position $x = L$, at the time $t = t$	94

S_x	Spin density for x component	94
S_y	Net spin density along the y direction parallel to the easy axis of FM	94
$\sigma\uparrow, \sigma\downarrow$	Electrical conductivities for $\uparrow$ channel, for $\downarrow$ channel	8
σ_σ	Conductivity for σ channel	9
σ_N	Electrical conductivity for NM	10
T	Temperature	51
$\tilde{t}$	Dimensionless time	106
t_F	Thickness of FM	53
t_N	Thickness of NM	53
τ_{sf}	Spin relaxation time	ii
τ_{sf}^{imp}	Spin relaxation time due to impurity scatterings	76
τ_{sf}^{ph}	Spin relaxation time due to phonon scatterings	76
τ_{sf}^{Surf}	Temperature dependent surface spin relaxation time	85
t_{trans}	Transit time	100
τ_e	Momentum relaxation time	ii
τ_e^{imp}	Momentum relaxation time due to impurity scatterings	77
τ_e^{ph}	Momentum relaxation time due to phonon scatterings	77
θ	Angle between polar axis and positive direction of H	30
Θ_D	Debye temperature	83
$\Theta(x)$	Step function	12
v	Spin diffusion velocity	100
V_1	Potential difference between FM and NM	12
V_3	Detection voltage at the detector FM3	20
V_P	Voltage for parallel magnetization states	14
V_{AP}	Voltage for antiparallel magnetization states	14
w_{Ag}	Width of Ag	49
w_F	Width of FM	53
w_N	Width of NM	53
w_{Py}	Width of Ag	49
ω_L	Larmor frequency	24
$\omega_L^{\pi/2}$	Larmor frequency for $\pi/2$ spin precession	94
ψ	Angle between polar axis and I_0	30
Z	Atomic number	85

Hiroshi Idzuchi　　Static and dynamic spin transport in lateral spin valves

（面内スピンバルブにおける静的及び動的スピン輸送　　井土宏）